SAPIENZA
UNIVERSITÀ DI ROMA

**Ph.D. PROGRAMME IN LIFE SCIENCES**

# FERRITIN NANOCAGES FOR THERANOSTIC APPLICATIONS

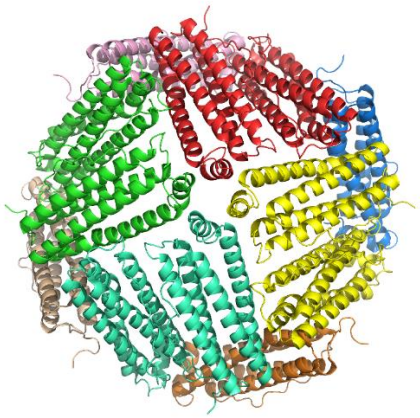


**Ph. D. candidate:**
**Lorenzo Calisti**
Cycle XXX (2014-2017)

**Tutor:**
Prof. Alberto Boffi

**Coordinator:**
Prof. Marco Tripodi

# Aknowledgements

The experimental work presented in this thesis was carried on at the Department of Biochemical Sciences A. Rossi Fanelli of University of Rome "Sapienza" and supported by Istituto Pasteur – Fondazione "Cenci-Bolognetti".

First and foremost, I wish to express all my thankfulness to my supervisor Prof. Alberto Boffi for having accepted me within its group. I am so grateful for the constant supervision and the support he gave me over the entire PhD path.

My deepest and sincere gratitude goes to Prof. Alessandra Bonamore and Dr. Alberto Macone, for all the care they spent in my personal growth and scientific training. Their support and guidance were way beyond of the academic supervision.

I would express all my affection to Dr. Paola Baiocco, Dr. Matilde Cardoso Trabuco, Dr. Irene Benni and to each of my colleagues in the Department for having showed me great friendship and shared funny moments during these years.

I would really thank Dr. Valeria de Turris, Prof. Amédée Des Georges, Dr. Tomasz Rygiel and Prof. Magdalena Krol for the precious collaboration and the invaluable contribution they gave me in my scientific research.

# INDEX:

# 1 Introduction

# 1.1 The Ferritin superfamily

Iron is virtually the most versatile and essential active metal for all forms of life: its unique electrochemical properties make it an ideal redox cofactor for many biologic processes that involve electron transfer, ranging from cellular respiration to nitrogen fixation and photosynthesis. Proteins can contain iron as part of different cofactors, such as iron-sulfur clusters (Fe-S) and heme groups. Moreover, it is used as a sensor of cellular redox status, acting as a switch to control protein activity in response to changes in cellular redox balance [Wayne Outten F et al., (2009)].

However, several problems are related to its employment in cellular biochemistry: iron is poorly available to the majority of life and its extremely low solubility in aqueous solution strongly reduces its bioavailability. Moreover, iron is potentially highly toxic in the presence of $O_2$ due to its redox activity, thus leading to ROS production and oxidative stress damages [Crichton R, (2016)].

To overcome these problems, sophisticated cellular mechanisms have been evolved to achieve iron storage, detoxification and metabolism. The Ferritin superfamily proteins play a vital role in this regard, acting as cellular repository of iron excess. Their biochemical properties allow to store iron in a safe but accessible form and then to release it again in a controlled way, thus avoiding toxicity [Andrews SC et al., (2010)].

The Ferritin superfamily comprehends three subfamilies of highly symmetrical and oligomeric proteins (see Fig. 1.1): bacterioferritins (Bfr), 'DNA-binding protein from starved cells' (Dps) and canonical Ferritins (Ft).

Bfr and Dps are homopolymers composed of 24 and 12 subunits, respectively, that are restricted to the archaeal domains of life [Andrews SC, (1998); Haikarainen T et al., (2010); Le Brun NE et al., (2010)]. Due to their different molecular geometry, these proteins diverge in their biological role: whereas

Bfr are mainly involved in iron storage, Dps handle the detoxification of free ferrous iron and hydrogen peroxide, thus preventing oxidative damages related to the Fenton chemistry [Chiancone E et al., (2010)].

The canonical Ferritin proteins are found in all three domains of life and represent the archetypical members of the Ferritin family. Although the sequence homology within the ferritin family is low, in some cases less than 20%, all ferritins share a common overall three-dimensional structure.

Ferritins are composed of 24 subunits that assemble to form a hollow and spherical nanocage, with internal and external diameters of about 8 and 12 nm respectively. Each subunit consists of a characteristic four-helical bundle (helices A-D), further divided into two homologous pairs of anti-parallel helices (A-B and C-D helices). A fifth short helix E points inside the protein cavity, roughly at 60° to the principal helix bundle. A long extended and unfolded loop traverses the full length of the helical bundle and connects the helix B being to helix C. [Andrews SC, (2010)]. Channels are formed where subunits meet, located at the six fourfold and eight threefold axes. Such pores connect the inner cavity to the outside and allow for the entry and the exit of iron ions and other small molecules [Watt RK et al., (2010)].

The main feature of Ferritins is their capability to catalyse the oxidation of ferrous iron to the ferric state. The catalytic site of this reaction, known as the "ferroxidase centres", is located in the middle of the four-helical bundle of individual subunits [Bou-Abdallah F, (2010); Andrews SC, (1998)].

Ferritins can reversibly store up to 4500 iron atoms inside the cavity in the form of a hydrous ferric oxy-hydroxide mineral. The surrounding protein shell carries out the dual task of maintaining the iron core in a soluble state and preventing the formation of reactive oxygen species. Afterwards, depending on cellular conditions and needs, several signals and pathways may lead to the release of ferric ions from the mineral core to the cellular environment [Melman et al., (2013)]. Ferritins are thus able to perform a fine tuning of cellular iron recycling and availability. Besides iron storage and detoxification,

they play a crucial role in several other processes such as cellular differentiation and proliferation, response to oxygen and programmed cell death named ferroptosis [Arosio P et al., (2017)].

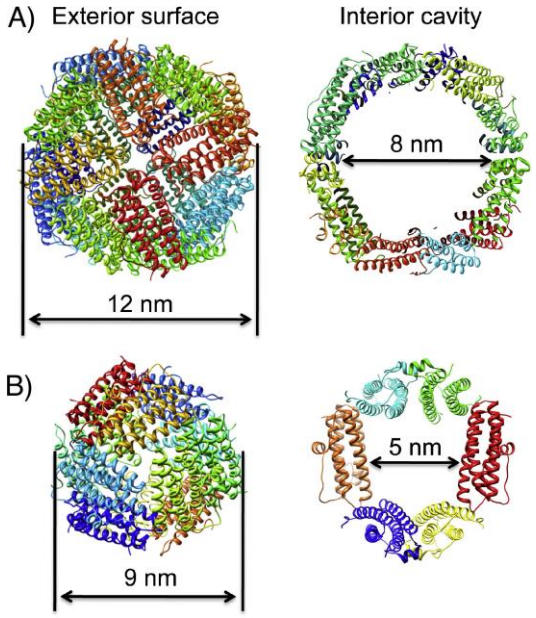


**Fig. 1.1:** three-dimensional structure and interior cavity comparison of (A) human heavy-chain ferritin and (B) *Listeria innocua* Dps. [modified from Uchida M et al., (2010)].

# 1.2 The Mammalian Ferritin

## 1.2.1: Mammalian ferritin structure

In all vertebrates, ferritins are heteropolymers composed of two types of polypeptide chains: the light (L) chain and the heavy (H) chain, respectively of 19 kDa and 21 kDa molecular weight. Amphibians have an additional M-type ferritin that strongly resembles the H-type [Ha Y et al., (1999); Kwak Y et al., (2014)].

Despite a 53% sequence identity, the H-chain and the L-chain display a considerably high degree of structural homology in both subunit fold and inter-subunit interactions. Nearly three quarters of their residues are disposed within five α-helical regions, named A, B, C, D and E helices from the N-terminal end (Fig. 1.2). In both H- and L-chain, the A-D helices are shaped into the characteristic four-helical bundle, while the short helix E lies at about 60° to the bundle. An unfolded loop of nineteen residues connects the opposite ends of B and C helices and short non-helical regions are present at the N- and C-termini. The two ends of the helical bundle are characterized by hydrophobic interactions while hydrophilic residues form a network of hydrogen bonds in the central core. X-ray crystallographic measurements pointed out that structural homology has been highly conserved across the evolutionary line: vertebrate amino acid sequences of either H- or L-chains share about 95% and 85% amino acid identity, respectively [Andrews SC et al., (1992)]. Several residues have been conservatively substituted during the evolutionary path, thus conferring different biological properties to H and L subunit. The residues involved in protein assembly are highly conserved and count for the formation of inter- and intra-species hybrids. These hybrid proteins are fully functional and correctly assembled into their three-dimensional structure [Otsuka S et al., (1981); Rucker P et al., (1996)].

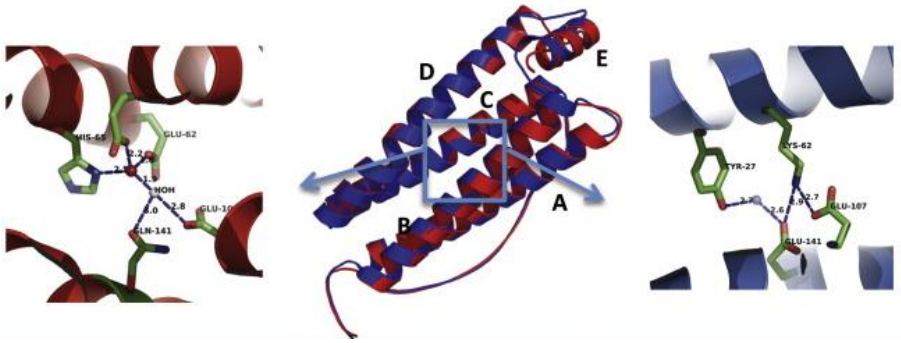


**Fig. 1.2: Three-dimensional structure of ferritin monomer.** Ferritin subunit consists of a four-helix bundle composed by two couples of anti-parallel α-helices (A–B helices and C–D helices respectively) connected by a long loop and a short C-terminal α-helix (E) that lies approximatively at 60° to the bundle. In the central panel, the superimposition of human ferritin L-chain (blue) and H-chain (red) is reported. The two subunits display a different aminoacid arrangement in the central part of four-helix bundle, as highlighted in the blue box. More precisely, the H-chain is characterized by a set of iron coordinating residues that constitute the ferroxidase center (shown in detail on the left side of the image). Those residues are instead replaced by a salt bridge forming amino acids in the L chain (shown on the right). [modified from Levi S et al., (2015)].

H-chain and L-chain are isostructural and assemble in different proportions to make various tissue-specific isoferritins. Tissues that need to minimize iron toxicity or exhibit high ferroxidase activity (i.*e.* heart and brain) contain isoferritins with high proportion of H-chain, while tissues such liver and spleen that are involved in long-term storage of iron have an excess of L-chains [Drysdale J, (2008)]. The H and L subunits, in fact, play a complementary role within the protein functions. The H-chain contains a dinuclear ferroxidase site that catalyses the oxidation of ferrous ion by $O_2$, producing $H_2O_2$. The L-chain,

instead, lacks catalytic activity but holds a microenvironment that facilitates iron nucleation and mineralization.

The ferroxidase site is located in the central hydrophilic region of H-chain and includes seven residues that are essential for maximal activity (shown in Fig. 1.2). More precisely, the amino acids Glu27, Tyr34, Glu61, Glu62, His65, Glu107, Gln141 (according to Human H-ferritin numbering) are involved in iron binding and oxidation. Such residues are highly conserved in vertebrates and are also present in the ferritins of plants and bacteria. In L-chains, these aminoacids are substituted with hydrophilic residues with the exception of Tyr34 and Glu61 that remain highly conserved. At variance, all mammalian L-chains contain two glutamate residues (Glu57 and Glu60 in human L-chain) that are placed inside the iron storage cavity and are reported to bind metal ions. They provide the L-chain with increased efficiency in promoting ferrihydrite nucleation and iron mineralisation [Hempstead PD et al., (1997); Chasteen ND et al., (1999)].

The three-dimensional structure of mammalian ferritin (shown in Fig. 1.3) is composed of 24 subunits assembled into a hollow spherical architecture. The protein shell is characterized by a 432-point symmetry and has the approximate geometry of a rhombic dodecahedron. Each of the twelve faces consists of a pair of subunits oriented with the E helices located at opposite ends of the dimer in an antiparallel topology. Although the oligomerization pathway is still unclear, these dimmers are very likely the first intermediates in the formation of the quaternary structure, in which each subunit interacts with other six subunits of the 24mer.

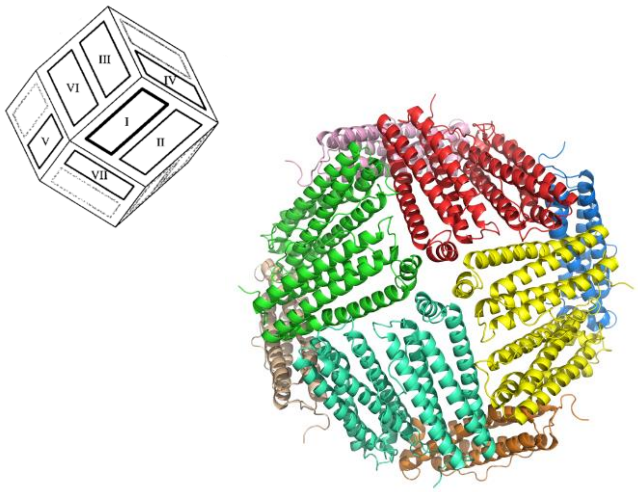


**Fig. 1.3: Three-dimensional structure of mammalian ferritin.** Representation of mouse H-ferritin as model for canonical mammalian ferritin (PDB code: 3WNW). The molecule is shown down the 4-fold symmetry axis and each ferritin dimer is reported with the same color. As highlighted, the protein cage is shaped in a rhombic dodecahedron with each of the twelve faces consisting of a dimeric subunit.

The N-terminus, the BC loop and the A and C helices line the outer surface of the molecule, whereas the B and D helices are located inward. Subunits are tightly packed and a number of intersubunit interactions confer high stability to the protein structure. These interactions mainly occur at helix interfaces and involve hydrogen bonds, salt bridges and hydrophobic contacts between facing residues [Crichton RR et al., (2016); Crichton RR et al., (2010); Harrison P et al., (1998)]. Other stabilizing interactions consist in salt bridges between the highly conserved Asp84 and Lys86 (Human H-ferritin numbering) inside the BC loops of facing subunits. [Bernacchioni C et al., (2014)]. Point mutations, deletions and insertions have been extensively used to identify the residues involved in quaternary assembly. Such genetic engineering also allowed to

modify the structural properties to the ferritin scaffold [Chen H et al., (2016); Huard DJ et al., (2013); Tosha T et al., (2012)]. The protein assembly leads to the formation of channels, which connect the inner cavity to the external environment. These channels lie along the 4-fold and 3-fold axes of symmetry and allows for the entry and the exit of ions and little diffusants through the protein shell (Fig. 1.4). The eight 3-fold channels, located at the convergence of three contiguous subunits, are lined by the C-terminal end of helix C and the N-terminal end of helix D of each subunit. They are hydrophilic and negatively charged pores with a funnel shaped structure. The inner passage is narrow (3.4 Å diameter) and lined by three aspartates and three glutamates (Asp131 and Glu134, in human H-ferritin) from the D helices. These aminoacids are highly conserved in both H and L vertebrate ferritins and confer cations selectivity to the channels, that are functional to the transit of ferrous ions through the protein shell.

The six 4-fold channels, instead, are bordered by the E helices of four neighbouring subunits, whose helical axes point parallel to the inner cavity. Each E helix provides the channel with three leucine residues (Leu158, Leu165, Leu169) aligned along the inner surface of the pore, making a long hydrophobic channel. The fourfold channels are impermeant to all cations with the exception of protons. They are probably involved in protons transfer inside and outside ferritin, that is essential to maintain the electroneutrality of the protein during iron oxidation and mineralization [Crichton RR et al., (2010); Bernacchioni C et al., (2014); Takahashi T et al., (2003)].

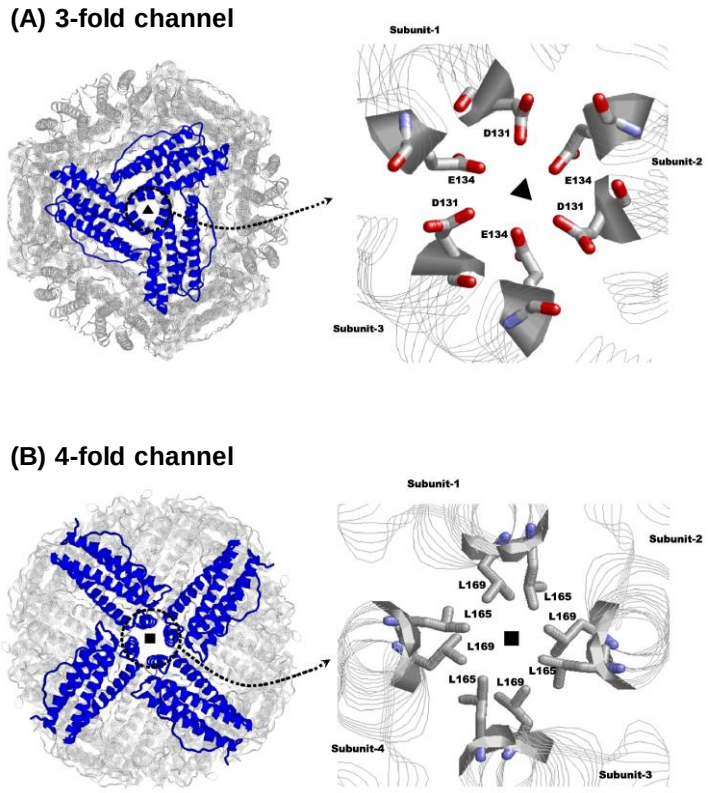


**Fig. 1.4: Schematic representation of ferritin 3-fold channels and 4-fold channels.** The eight 3-fold channels (A) are formed at the juxtaposition of three contiguous subunits. The six 4-fold channels (B), instead, are located at the convergence of four subunits. For both these pores, the lining aminoacids are shown. [modified from Bou-Abdallah F et al., (2010)].

## 1.2.2: Iron oxidation and mineralization in Mammalian ferritins

Despite the differences in the aminoacid sequence and kinetic parameters, all vertebrate ferritins share a common catalytic mechanism. Ferrous ions move through the protein shell along the 3-fold channels and once inside the cavity they migrate to the ferroxidase center. The ferroxidase center represents the catalytic site where iron oxidation occurs, yielding $H_2O_2$ as side product. Ferric ions are then mineralized in the presence of phosphate and shape the mineral core [Theil EC et al., (2013)].

Iron uptake and movements inside the ferritin cavity are driven by electrostatic gradients between the actives sites of the protein, which are correlated with high charge density. The external surface of human H-ferritin is characterized by highly conserved acidic residues (Asp84, Asp89, Asp91, Asp92, and Glu94) and the inner passage of 3-fold channels is lined by conserved glutamates and aspartates from the three facing subunits (Glu131, Asp134 and Glu140). The ferroxidase center too displays a wide region of negative residues (Glu27, Glu61, Glu62, Glu107, Glu140 and Glu147) and six glutamates at the nucleation site (Glu61, Glu64 and Glu67 from two different monomeric subunits) form a ring of negative charges. Several asparagine, glutamine and lysine residues (Gln10, Asn11, Asn109, Gln112 and Asn125), instead, surround the external entrance of the 3-fold channels. Thus, the 3-fold channels, the ferroxidase site and the nucleation site all show negative values of the electrostatic potential, while the outer entrance to the three-fold channels is characterized by regions of positive potential. This arrangement creates an electrostatic field along the 3-fold channels directed towards the interior cavity that guides cation entrance into the protein cavity [Douglas T et al., (1998)].

Several other residues also contribute to the translocation of iron along the 3-fold channels and the accepted mechanism of iron entrance is reported in Fig. 1.5: the His118 and Cys130 residues are responsible for the initial contact of fully hydrated ferrous ions ($[Fe(H_2O)_6]^{2+}$) at the wide entrance of the 3-fold

channels. The hexaaquo ferrous ions then migrate to the deeper triads of Glu134 and Asp131 residues and move along the narrow path of the pore gradually loosing their solvation sphere.
X-ray measurements of human H-ferritin confirmed two $[Fe(H_2O)_6]^{2+}$ ions coordinated by Asp131 and Glu134 and similar results were also obtained the crystal structure of frog M-ferritin treated with $Fe^{+2}$ [Bradley JM et al., (2017); Pozzi C et al., (2015) (a); Pozzi C et al., (2015)(b)].

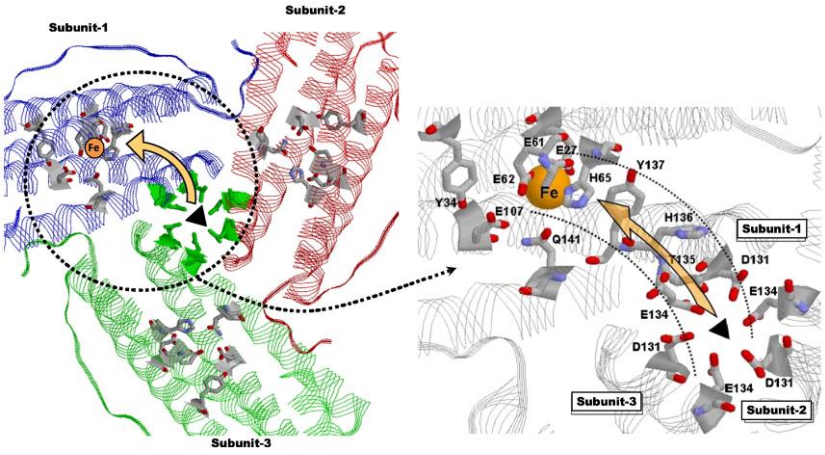


**Fig. 1.5: Putative $Fe^{+2}$ pathway from the 3-fold channel to the ferroxidase center of ferritin.** Residues responsible for iron initial binding and migration are reported. Moreover, the aminoacids of the ferroxidase center are also shown [ modified from Bou-Abdallah F et al., (2010)].

Electrostatic factors appear to play a dominant role also in the migration of ferrous ions to the ferroxidase center. In fact, the ferroxidase site too has very negative values of the potential, which attract ferrous ions from the inner opening of the 3-fold channels. Bou-Abdallah and co-workers proposed that

the residue Thr135, His136, and Tyr137 could be involved in this pathway [Bou-Abdallah F et al., (2008)].

The ferroxidase center of H-chain catalyses the fast oxidation of $Fe^{+2}$ to $Fe^{+3}$. During the reaction, two $Fe^{+2}$ ions are simultaneously oxidized from a single molecule of $O_2$ that is reduced to $H_2O_2$, yielding a $Fe^{+2}/O_2$ ratio of 2:1.

The ferroxidase center comprises a dinuclear iron center, consisting of two metal binding-sites named site A and B. All the seven residues involved in the catalytic mechanism (shown in Fig. 1.6 (a)) are highly conserved along the evolutionary paths and are found also in prokaryotic and plant ferritins. The first $Fe^{+2}$ ion is bound in the site A by a histidine (His65) and a monodentate glutamate (Glu27), while the second $Fe^{+2}$ in site B is ligated by a terminal glutamate (Glu107). Moreover, a bridging glutamate (Glu62) contributes to iron binding in both sites. An additional glutamate (Glu62) is found to adopt two conformations, one bound to the metal at the B site, the other projecting toward the cavity, suggesting its involvement in the transfer of ferric iron into the cavity. Besides these residues involved in metal binding, also Gln141 and Tyr34 residues are strictly conserved amongst eukaryotic and prokaryotic ferritins. The latter residue, in particular, seems to play a major role in the electron transfer between the cavity and the ferroxidase center that occurs within the catalytic mechanism [Bradley JM et al., (2014); Ebrahimi KH et al., (2013)].

The ferroxidase reaction (reported in eq.1) proceeds through several steps and leads to the production of different intermediate species. A general overview of this mechanism is reported in Fig. 1.6 (b) [Bou-Abdallah F, (2010)].

**Eq.1**: $$2Fe^{2+} + O_2 + 4H_2O \rightarrow [Fe_2O_2]^{2+} \rightarrow [Fe_2O(OH)_2]^{2+} \rightarrow 2\ FeOOH_{(core)} + H_2O_2 + 4H^+$$

The resulting ferric ions then leave the catalytic center as oxo(hydroxo)-complexes and move to the inner cavity of ferritin, where become part of the stable nucleus of ferrihydrite mineral core. The nucleation site is correlated with the highest negative potential value in the ferritin structure, indicating that this region is very attractive to positively charged ions. A major role in this sense is played by the L-chains, that support the ferroxidase activity of the H-subunits by accelerating iron translocation from the di-iron center into the cavity. Moreover, the L- subunit assists the formation of polynuclear ferrihydrite crystals at the nucleation site and contributes to its electrostatic stabilization [Crichton RC et al., (2010)].

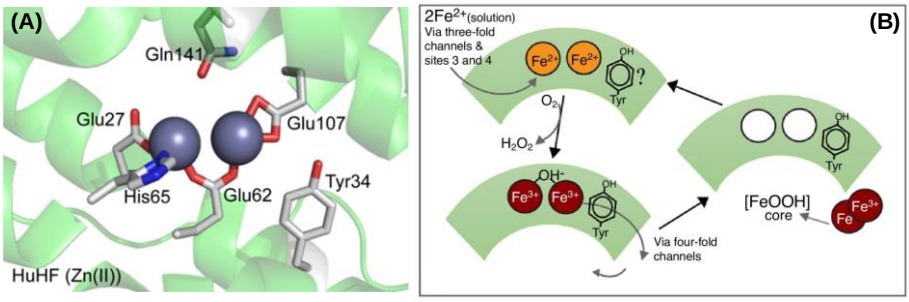


**Fig. 1.6 (a): Structural features of the H-chain-type ferroxidase center.**
(A): Structure of Human H-chain ferroxidase center with $Zn^{+2}$ bound at the center. The A and B binding sites are displayed [from PDB 2CEI; modified from Bradley JM et al., (2014)].
(B): Schematic representation of ferroxidase reaction [modified from Bradley JM et al., (2017)].

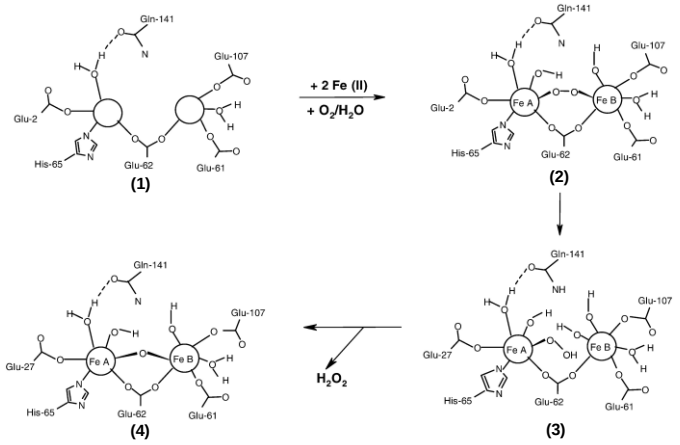


**Fig. 1.6 (b): Accepted catalytic mechanism of the H-chain-type ferroxidase center.** This scheme reports the accepted catalytic mechanism and the overall intermediates produced within the ferroxidase reaction: two $Fe^{+2}$ ions stepwise bind to the sites A and B of Apoprotein **(1)**. Dioxygen subsequently binds to site B, leading to the production of the μ-1,2-peroxo di-iron(III) intermediate **(2)**. This complex undergoes towards hydrolysis, thus producing the μ–hydroperoxo di-iron (III) complex **(3).** This intermediate quickly decays to the μ–oxo di-iron (III) complex **(4),** releasing an $H_2O_2$ molecule. Lastly, the resulting ferric ions leave the catalytic center as oxo(hydroxo) iron (III) complexes to become part of the growing mineral core [modified from Bou-Abdallah F et al., (2010)].

Besides the ferroxidase mechanism, other two iron oxidation reactions occur within the protein shell, whose relevance is a function of the iron flux into the protein. They correspond to the mineral surface and the $Fe^{+2}$ + $H_2O_2$ detoxification reactions. The mineral core building in vertebrate ferritins thus results from the combination of these three pathways [Zhao GH et al., (2003); Yang XK et al., (1998); Xu B et al., (1991)].

At low iron flux (48-800 $Fe^{+2}$/protein), iron oxidation is entirely carried out at the ferroxidase centre (see eq.1). At higher iron loadings (higher than 800

$Fe^{+2}$/protein), instead, the dinuclear site is saturated and the dominant reaction switches to the mineral surface reaction (eq.2). Under such conditions, the oxidation and deposition of further iron directly occurs on the growing surface of the mineral in an autocatalytical way, in agreement with the crystal growth model. The process involves the transfer of four electrons and results in the complete reduction of dioxygen to water [Bradley JM et al., (2014)].

**Eq.2:** $4Fe^{+2} + O_2 + 6H_2O \rightarrow 4FeOOH_{(core)} + 8H^+$

Lastly, at intermediate iron loadings (100-500 $Fe^{+2}$/protein), part of the $H_2O_2$ produced during the ferroxidase mechanism is consumed in the detoxification reaction (eq.3). This reaction allows the ferritin to minimize the hydroxyl radical production during mineralization and to avoid damages related to ROS production [Bou-Abdallah F, (2010)].

**Eq.3:** $2Fe^{+2} + H_2O_2 + 2H_2O \rightarrow 2FeOOH_{(core)} + 4H^+$

Thus, once the core has formed, the mineral core growth is carried out by a complex interplay of multiple iron oxidation pathways.

## 1.2.3: Mammalian Ferritin biophysical properties

The high number of non-covalent interactions and the tight subunit packing provide the ferritin scaffold with an extremely high resistance to chemical denaturation, pH changes and heat stress.
Ferritins are endowed with an uncommon thermostability, that is generally exploited for the purification of both native heteropolymers and recombinant homopolymers. They easily withstand temperature higher than 70°C and the thermal stability improves as a function of the L-chain content within the protein shell [Stefanini S et al., (1996)].

However, the most attractive feature of ferritin nanocage is the ability to undergo towards a pseudoreversible disassembly-reassembly process controlled by pH. Nearly all ferritins disassemble into subunits under extreme acidic conditions (pH ~ 2) without denaturing. They then reconstitute the 24-mer shell when pH is adjusted back to ~7. Both pathways proceed in a stepwise manner, leading to the hierarchical formation of several oligomeric intermediates [Kim M et al., (2011)].

Gerl and co-workers proposed a general mechanism for ferritin assembly that has been further confirmed by several authors. Monomeric subunits are highly unstable in solution and rapidly dimerize, thus forming stable dimers that act as single structural units. The protein self-assembly then proceeds through a sequence of association steps during which dimers combine among themselves and produce a mixture of partially assembled subunits. These subunits include tetramers, examers and, in small amounts, dodecamers. Hence, tetraeicosameric cage would result from the progressive juxtaposition of dimeric units via tetramer and hexamer intermediates [Zhang Y et al., (2011); Gerl M et al., (1987); Gerl M et al., (1988)].

Measurements on mammalian ferritins pointed out that structural recovery upon acidic treatment occurs within one hour, being faster for the H/L-chain heteropolymers than for the H-homopolymers. The formation of heteropolymers is favourited respect to the corresponding homopolymers and

this is mainly due to the preferential formation of H/L heterodimers over homodimers during the self-assembly process [Carmona F et al., (2017)].

The self-assembly property encouraged the employment of recombinant ferritins as biomedical nanocarriers. Bioactive compounds can be encapsulated within the internal cavity but the extremely acidic pH required for the protein shell dissociation might represent a major concern for the stability of several molecules. Hence, several works have been carried out in order to engineer ferritin interfaces and allow for the dissociation under milder conditions. Modifications involving the Lys62-Glu107 salt bridge in human H-chain, for instance, increases its stability to low pH and other denaturants [Santambrogio P et al., (1992)]. Chen and co-workers recently developed a novel construct by cleaving the last 23 amino acids at the C-terminal end of human H-ferritin, which correspond to the DE turn and helix E and are involved in the 4-fold interactions. The deletion yielded a nanocages which disassemble at pH 4.0 and reassemble at pH 7.5 [Chen H et al., (2016)]. The engineering of ferritin surfaces even allowed to make the self-assembly of ferritin controllable by divalent copper binding [Huard DJ et al., (2013)].

A deeper understanding of the assembly mechanism and of the interactions that occur at the ferritin interfaces are therefore mandatory for the development of novel constructs suitable for biomedical applications.

# 1.3 Archaeal and bacterial ferritins

Archaeal and bacterial ferritins, as plant ferritins, are homopolymers composed of 24 identical subunits.

The ferritin from *E. coli* (FtnA) was discovered in the early '90s and is probably the one that has been most extensively characterized among the archetypal bacterial ferritins [Hudson AJ et al., (1993)]. Homologue proteins have been subsequently identified in several other bacteria, such as *Campylobacter jejuni*, *Porphyromonas gingivalis* and *Helicobacter pylori* [Clerte S et al, (1999); Ratnayake DB et al, (2000); Waidner B et al., (2002)]. More recently, two ferritins have been identified form Archaea *Archaeoglobus fulgidus* (Af-Ft) and *Pyrococcus furiosus* (Pf-Ft), which bear an impressive similarity to the bacterial ones [Johnson E et al., (2005); Tatur J et al., (2007)].

Although only distantly related to eukaryotic H-chain polypeptide (∼22% sequence identity), prokaryotic ferritins share most of their structural and functional features with vertebrate ones. Each subunit is shaped into the characteristic four-helical bundle (helices A–D), with the fifth short helix E arranged with a slope of 60°. Short unfolded regions are found at the N- and C- terminal ends, while the long unfolded BC loop traverses all the length of the bundle and connects the helices B and C. The protein shell consists of 24 subunits very similar to vertebrate H-chains, therefore all catalytically active. Subunits are arranged into the typical 4,3,2 octahedral symmetry and channels are formed at the juxtaposition of subunits (Fig. 1.7). The 3-fold channels are significantly less polar than their eukaryotic equivalents, being lined by both hydrophobic and hydrophilic residues. The 4-fold channels, instead, are polar at both inner and outer entrance and hydrophobic in the central part.

Several residues involved in inter-subunit interactions and in the three-dimensional assembly are unchanged with respect to vertebrate ferritins. Similarly to eukaryotic proteins, most of prokaryotic ferritins display the characteristic pH-dependent assembly, although important differences may

arise depending on each sequence. Besides, the tight packing of the helical-bundle and the high number of hydrogen bonds and salt bridges that occur within the subunit confer an overall thermostability to prokaryotic ferritins. Ferritin from hypertermophilic organisms such as *Archaeoglobus fulgidus* are endowed with an extreme thermal resistance and among these, the *Pyrococcus furiosus* one is considered the most thermostable. It has been stated that the preservation of the monomer fold, rather than the 24-mer assembly, protects the ferritin from inactivation by heat [Le Brun NE et al., (2010); Stillman TJ et al., (2001); Tatur J et al., (2007)].

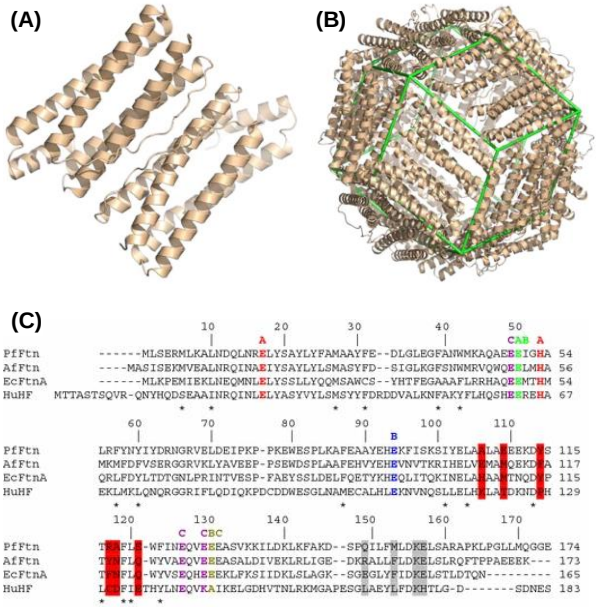


**1.7: Three-dimensional structure of prokaryotic ferritin.** Cartoon representation of *E.coli* FtnA subunit dimer (PDB 1EUM); (B) overall threedimensional structure of *E.coli* FtnA tetraeicosamer [modified from Le Brun NE et al., (2010)]. (C): sequence comparison of *Pyrococcus furiosus* ferritin (PfFtn), *Archaeoglobus fulgidus* ferritin (AfFtn), *E.coli* ferritin (EcFtn) and human H ferritin (HuHF) [modified from Tatur J et al., 2007].

The major differences between prokaryotic and vertebrate ferritins are related to the structure of the catalytic site. The bacterial ferroxidase centre closely resembles that of mammalian H-chain, comprising the typical dinuclear iron centers (site A and B) and all the seven residues that has been reported to be involved in eukaryotic catalytic mechanism. However, prokaryotic ferritins have an additional and closely located third iron-binding site (site C) that is unique to these proteins and is ∼7 Å away from the B-site and ∼11 Å from the A-site.

The structure of the ferroxidase center of *E. coli* FtnA in its iron-bound form is shown in Fig. 1.8. Iron is coordinated in site A by a monodentate glutamate (Glu17), a histidine (His53) residue and a bridging glutamate (Glu50). Besides Glu50, iron is ligated at site B by a terminal glutamate (Glu94) and by another glutamate ligand (Glu130). Glu130 residue is actually a bridging ligand to the third iron-binding site, the site C, which comprises three additional glutamates (Glu49, Glu126 and Glu129) for iron coordination. Lastly, prokaryotic ferroxidase center includes two additional residues (Tyr24 and Gln127) also involved in the catalytic reaction [Bou-Abdallah F et al., (2014); Bradley JM et al., (2014); Treffry A et al., (1998)]. Sequence comparisons showed that site C ligand and ferroxidase center residues and are highly conserved among prokaryotic ferritins. These include even two archaeal proteins from *Archaeoglobus fulgidus* (Af-Ft) and *Pyrococcus furiosus* (Pf-Ft) [Le Brun NE et al., (2010); Tatur J et al., (2007); Johnson E et al., (2005)].

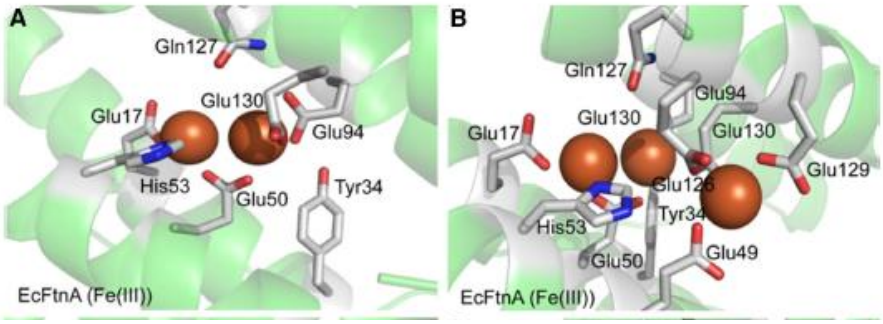


**Fig. 1.8: The prokaryotic-type ferroxidase center.** Three-dimensional structure of *E.coli* FtnA ferroxidase center. (A): representation of bridged A and B sites where residues Gln127, Glu130, Glu94, Tyr34, Glu50, His53 and Glu17 accounts for iron binding. The center is shown without the site C to highlight the similarity with mammalian ferroxidase center. (B): representation of the overall ferroxidase center with site C included. Residues Glu49, Glu129 and Glu126 of site C provide the prokaryotic ferroxidase center with an additional iron binding site [modified from Bradley JM et al., (2014)].

Iron mineralization occurs via a mechanism related to that of eukaryotic H-chains but complicated by the presence of the site C (Fig. 1.9). As for mammalian H-chain, the binding of ferrous ions and dioxygen at the ferroxidase center leads to iron oxidation. All iron oxidation intermediates shown in vertebrate mechanism are formed also in bacterial and archaeal proteins, although the relative rate of formation and decay can represent a limit to their detection [Honarmand Ebrahimi K et al., (2009)]. Moreover, isothermal titration calorimetry measurements demonstrated the existence of essentially two classes of binding sites for each subunit, with a stoichiometry of 2 $Fe^{+2}$ for the site A and B of each dinuclear ferroxidase centers [Bou-Abdallah F et al., (2005)].

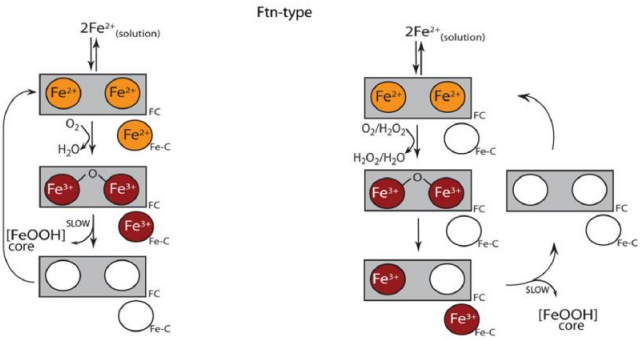


**Fig. 1.9: catalytic mechanism of prokaryotic ferroxidase center and alternative roles proposed for site C.** On the left, the site C acts as an additional catalytic site contributing to $Fe^{+2}$ oxidation. Upon oxidation of $Fe^{+2}$ atoms bound at the site C, the electrons produced are transferred to the nearby dinuclear catalytic center and to the $Fe^{+2}$ atoms bound to the A and B sites. On the right, site C acts as an iron transit/holding site slowing down the iron flux to the nearby dinuclear catalytic center [modified from Bradley JM et al., (2014)].

The role of the site C has not yet been entirely clarified. Compared to site A and B, it exhibits just weak iron binding properties and seems rather involved in modulating the stoichiometric and kinetic properties of the protein. *E.coli* FtnA, for instance, differs from human H-chain in having an $Fe^{2+}/O_2$ stoichiometry for the initial oxidation reaction of ~3 versus ~2 for human one. Similarly, Pf-Ft has a stoichiometry of ~3. The observation that the iron/dioxygen stoichiometry dropped to 2 when site C residues were substituted further confirmed this hypothesis [Yang X et al., (1998); Xu B et al., (1991); Treffry A et al., (1998)].

Moreover, the site C appears to be of variable importance for catalytic activity in ferritins from different organisms. In FtnA from *E.coli*, the site C appears to control the iron flux to the ferroxidase center and to modulate $Fe^{+2}$ binding at the adjacent iron sites A and B, working both as a transit site and as gated iron

pore. A strong interplay exists between the site C and the dinuclear site, suggesting the presence of inter- and intrasubunit negative cooperativity. Site C seems to slow iron oxidation and turnover at the dinuclear ferroxidase center, as the iron flux through the ferroxidase centre of FtnA is much slower than the eukaryotic H-chain one. Moreover, the loss of site C makes the center became structurally and functionally similar to the H-chain-type center [Bou-Abdallah F et al., (2014); Bou-Abdallah F et al., (2005); Treffry A et al., (1998)].

In Pf-Ft from *Pyrococcus furiosus*, instead, the site C seems to play a different role and contributes to iron oxidation and mineralisation. An electron transfer occurs from the $Fe^{+2}$ bound at the site C to the di-$Fe^{+3}$–protein complex at the dinuclear site. The ferroxidase center therefore acts as a stable catalytic center and accepts electrons derived from the oxidation of $Fe^{2+}$ at nearby site C. The resulting $Fe^{+3}$ then leaves the C site to the cavity and becomes part of the mineral core, while molecular oxygen is reduced to hydrogen peroxide to complete the cycle of the electron transfer chain [Tatur J et al., (2005); Honarmand Ebrahimi K et al., (2009); Bou-Abdallah F et al., (2010)].

Hence, even if the exact role of the site C in prokaryotic ferritins still remains undefined, it is generally accepted that it fulfils distinct tasks in different proteins, contributing to iron oxidation in some while acting as transit and holding site in others.

However, some major point regarding prokaryotic catalytic properties are still debated: a parallel mechanism for iron oxidation seems to occur, as a tyrosyl radical related to the highly conserved Tyr24 has been observed in both Ftna and Pf-Ft proteins. It has been proposed that the electron from this radical, along with three resulting from oxidation of $Fe^{2+}$ ions at sites A, B and C, would participate to the four-electron reduction of $O_2$ to water [Bradley JM et al., (2014)].

As for mammalian proteins, the mineral core building in prokaryotic ferritins results from multiple iron-oxidation pathways. At low iron flux, the catalytic reaction at ferroxidase center is dominant. At higher iron loading, iron

oxidation directly occurs on the mineral surface in an autocatalytic way. The hydrogen peroxide collaterally produced by the ferroxidase reaction further oxidises $Fe^{+2}$ ions, contributing to the mineral core growth and to the radical detoxification [Bou-Abdallah F et al., (2014)].

Among the bacterial structures, the *Archaeoglobus fulgidus* ferritin (Af-Ft) has recently emerged due to its unprecedented structural and biophysical features. Af-Ft shares a high sequence identity with human H-ferritin, *E. coli* ferritin A and *Pyrococcus furiosus* ferritin (31%, 37% and 50% respectively). Moreover, it is closely related to archetypal bacterial and eukaryotic ferritins in its iron binding mode, secondary and tertiary structure. In spite of the high degree of structural similarity, the quaternary structure of Af-Ft strikingly differs from the other three. In fact, whereas the archetypal ferritins have the canonical octahedral (4-3-2) architecture, the Af-Ft tetracosamer exhibits a tetrahedral (2-3) symmetry, which is typical of smaller dodecamer ferritin-like proteins (Fig. 1.10). This unusual assembly does not display the 4-fold channels and constrains the quaternary structure, thus leading to the appearance of four large triangular openings (~ 45 Å wide) in the protein shell. These large pores display positive electrostatic surface potential at the apices and provide the ferritin molecule with unconventional route for the movement of ions and larger molecules through internal cavity. The “open” quaternary structure of Af-Ft contrasts the “closed” paradigm of a typical ferritin cage and to date is considered unique among all other known structures [Johnson E et al., (2005)].

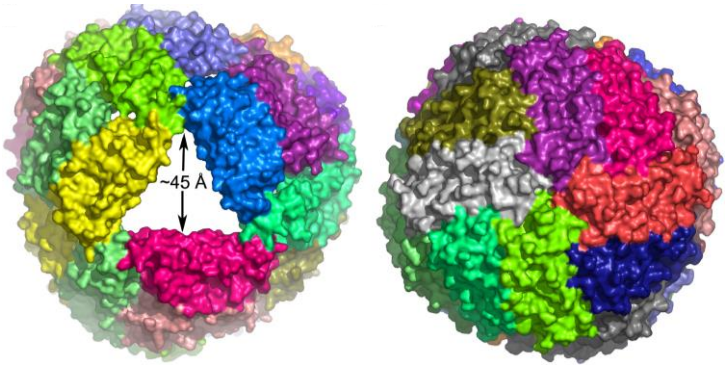


**1. 10: Three-dimensional structure of *Archaeoglobus fulgidus* ferritin.** On the left, three-dimensional representation of the unique "open" tetraeicosameric assembly of *Archaeoglobus fulgidus* ferritin (PDB code: 1S3Q). In detail, one of the four 45 Å-wide triangular pores at the 3-fold symmetry axis is shown. On the right, a closed archetypal tetraeicosameric ferritin (human H-ferritin, PDB code: 2FHA) is reported for comparison purposes [modified from Johnson E et al., (2005)].

Af-Ft also exhibits uncommon association-dissociation properties, as its self-assembly seems to be dependent on ionic strength instead of pH. Af-Ft nanocage largely exists as tetraeicosamer at high ionic strength, while the equilibrium shifts towards dimeric species at low ionic strength. Several hydrophobic contacts in fact occur at the subunit interfaces and play an important role in the stabilization of the assembled structure. Hence, salt-mediated association is driven by the improvement of hydrophobic interactions at high ionic strength [Swift J et al., (2009)].

The stability of the Af-Ft tetrahedral configuration is governed by two critical and non conserved residues in the helix E of the 4-helices bundle, namely Lys150 and Arg151 (Fig. 1.11). The side chain of Lys150 forms an hydrogen bond with the backbone O of Met111 that stabilizes the tetrahedral configuration. The Arg151 side chain, instead, sterically hinder the association

of helices E at the octahedral 4-fold interface, thus preventing the octahedral assembly [Johnson E et al., (2005)].

To unravel the structural role of these residues, a double mutant (namely Af-Ft-AA or Af-Ft K150A/R151A) has been recently developed by replacing Lys150 and Arg151 with two alanines. The replacement of these key residues produces an important rearrangement of the quaternary structure and flips a "symmetry switch" from the Af-Ft tetrahedral structure to the Af-Ft-AA octahedral symmetry. In Af-Ft-AA, the canonical "closed" architecture of the archetypal ferritins is restored due to the stabilization provided by the four mutant Ala151 residues at the 4-fold symmetry interfaces (Fig. 1.11). Although Af-Ft-AA retains salt-mediated assembly properties, its tetraeicosameric shell is much more stable compared to Af-Ft one, as a result of the improvement of the interface hydrophobic interactions provided by these mutations [Sana B et al., (2013)].

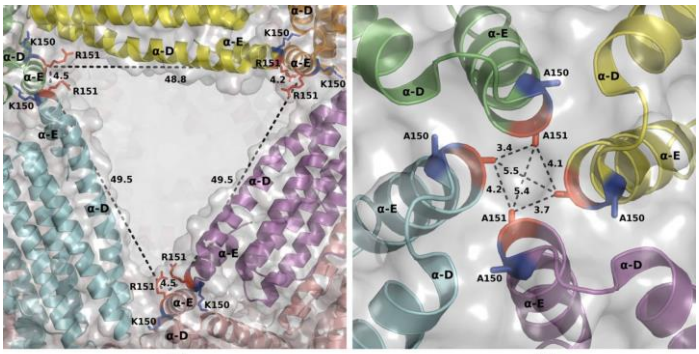


**1.11: comparison of ferritin shell pores in Af-Ft and Af-Ft-AA proteins.** (A) detailed view of the large triangular pore of wild type Af-Ft ferritin (PDB code: 1S3Q). Residues Lys150 and Arg151 are drawn as red and blue sticks and their relative intermolecular distance in reported.
(B) Detailed view of narrow pore of Af-Ft-AA mutant at the 4-fold simmetry axis (PDB code: 3KX9). Ala150 and Ala151 residues are shown with their relative intermolecular distance in evidence [modified from Sana B et al., (2013)].

# 1.4 Biotechnological applications of ferritins: state of art and future perspectives

The last few years have seen a growing interest in the development of biomedical nanodevices to improve the pharmacokinetic and toxicological profile of therapeutics or diagnostic probes. Several inorganic or polymeric nanoparticles have been designed, but just a few of them have been clinically approved due to their toxicity, non-selective biodistribution and general low clearance. Liposomes as well are suitable for improving drug bioavailability and reducing toxicity profile, but generally lack of method for targeting a specific tissue or cell type [Peer D et al., (2007); Mok H et al., (2013); Xing M et al., (2015)].

Protein nanodevices, instead, are particularly attractive as nanomedicine platforms: compared to polymeric materials, proteins are highly biocompatible and biodegradable materials, displaying as well lower toxicity although immunogenicity may be a significant drawback. Recombinant technologies allow to produce highly purified proteins at gram scale and several chemical or genetical manipulation can be employed to further modify their structure [Elzoghby AO et al., (2012); Maham A et al., (2009)].

In this context, ferritin is arising as an extremely promising scaffold for the development of smart nanocarriers. Both the inner and the outer surface of ferritin can be engineered, thus conferring several functionalities onto a single molecule. Its ability to assemble and disassemble in a pH-dependent manner allow to encapsulate a wide variety of molecules within the cavity, while the interactions with the inner surface prevent the leakage of the cargo. Figure 1.12 reports a general overview of currently employed strategies for drug loading and release using protein cages as smart nanocarriers.

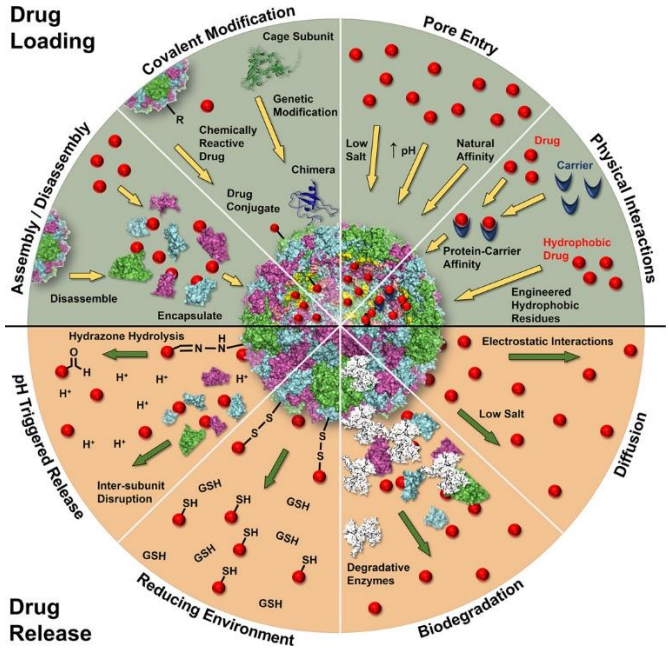


**Fig. 1.12: Biotechnological approaches for drug loading and release using protein cages** [ modified from Molino et al., (2014)].

Moreover, ferritin is endowed with attractive targeting features to specific cell types. Li and co-workers pointed out that extracellular ferritin interacts with cells through the Transferrin Receptor-1 (TfR-1) and undergoes internalization, being found in early and recycling endosomes [Li L et al., (2010)]. The pathway for tranferrin recognition and internalization by TfR-1 receptor is shown in Fig. 1.13. Most likely, ferritin molecule follow the same route. As TfR1 is overexpressed in many types of cancer cells, ferritin can provide the selective homing of drugs or probes to tumors. The cellular specificity of this protein has been further extended by addition on the outer surface of chemical or peptide targeting moieties, such as the RGD peptide, the anti-melanocyte stimulating hormone peptide, the extracellular domain of

myelin oligodendrocyte glycoprotein and several antibodies [Truffi M et al., (2016)].

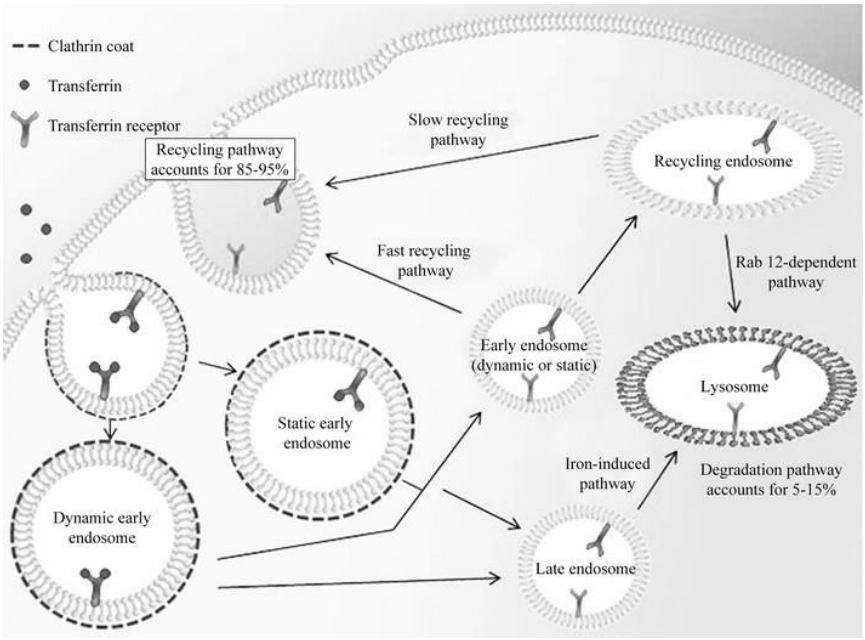


**Figure 1. 13. Transferrin-1 receptor-mediated endocytosis.** Upon binding, transferrin undergoes internalization through a clathrin-coated endocytosis mechanism thus reaching the cytoplasm. Transferrin enters the endosomes where dissociation of iron from transferrin occurs. The complex is then recycled back to the surface (85-95%) or undergo lysosomal degradation (5-15%) [modified from Tortorella et al., (2014)].

## 1.4.1: Therapeutic applications

The major limit of conventional chemotherapy is the lack of selectivity in the mechanism action, which leads to harmful side effects, drug resistance and difficulty in dosage selection. A drug delivery system is thus required to prevent the exposure of healthy cells to the drug and to ensure the proper delivery to cancer cells. The employment of engineered ferritin constructs provided encouraging results in this sense [Truffi M et al., (2016)].

Cisplatin has been successfully entrapped in the ferritin shell and the pharmacological properties of the resulting nanoparticles have been studied on tumour lines [Yang Z et al., (2007); Xing R et al., (2009); Ji XT et al., (2012)]. In particular, Falvo and co-workers recently developed a novel antibody–drug conjugate by chemically functionalising the cisplatin-loaded apoferritin with an antibody against the melanoma antigen CSPG4 [Falvo E et al., (2013)]. All these studied provided strong evidence of a general improvement of the cisplatin antiblastic efficacy even in tumor such as melanoma, which is totally refractory to traditional chemotherapy at its advanced stages.

The inner cavity of ferritin is also suitable for the incorporation of non-metal-containing drugs, despite lower interactions occur with the protein cage. Doxorubicin is a widely used anticancer drug but is affected by major toxicities and poor pharmacokinetic properties. The encapsulation within the protein cage yielded in an improvement of Doxorubicin bioavability and, due to targeted delivery, the tumor growth inhibition was achieved at lower doses compared to the plain drug [Liang M et al., (2014); Kilic MA et al., (2012)]. Recent findings also highlighted that Doxorubicin-loaded ferritin translocates into the nucleus and releases the drug directly into the nuclear compartment. Although the mechanism is not fully understood, this outcome suggests that ferritin is intrinsically able to undergo nuclear translocation and can be exploited for the development of a novel class of smart drug delivery system with nuclear target [Zhang L et al., (2015); Bellini M et al., (2014)].

The ability of ferritin to sequester transition metals can been further exploited in radiotherapy cancer treatment to deliver radioisotopes to the tumor. Hainfeld demonstrated that ~800 $^{235}U$ atoms can be encapsulated into each nanocage. The resulting nanoparticles provide enough radiation to kill surrounding tumor cells [Hainfeld JF et al., (1992)]. Moreover, a novel construct of human ferritin has been recently developed for the targeted delivery of small interfering RNA (siRNA) to cancer cells [Lee EJ et al., (2015)].

Self-assembling protein nanoparticles are currently studied also as novel potential platforms for vaccination and immunization purposes. While the 19th and early 20th century vaccines were made of killed or inactivated pathogens, modern ones contain highly purified antigens obtained by recombinant technologies. Modern vaccines are thus safer, but tend to induce lower levels of protective immunity. By fusing the antigen onto the monomeric subunit, ferritin shell can present multiple copies of antigens with higher stability and in a well-ordered manner. Numerous binding events can occur simultaneously between the nanoparticle and the host immune cells, thus resulting in the improvement of the immunogenicity. Moreover, since ferritin is composed by subunits related by three-fold axis symmetry, it is perfectly suitable for the presentation of trimeric antigens [López-Sagaseta J et al., (2015)].

Kanekiyo and co-workers fused the influenza virus haemagglutinin (HA) at the interface of adjacent subunits of *Helicobacter pylori* ferritin, so that it spontaneously assembled into eight trimeric viral spikes on the external surface. Injected in mice, the particle elicited the production of neutralising antibodies against different HA variants with an higher potency compared to a commercially available influenza vaccine. Moreover, no autoimmune reaction against the *Helicobacter pylori* ferritin was observed, despite the high degree of divergence from mammalian ferritin sequences [Kanekiyo M et al., (2013)]. For similar purposes, other groups linked antigens from Epstein–Barr virus and Hepatitis C virus onto the outer surface of ferritins [Kanekiyo M et al., (2015); He L et al., (2015)]. The satisfying outcomes support the hypothesis that ferritin may represent a useful scaffold for vaccination and immunization aims.

## 1.4.2: Bioimaging applications

The improvement of diagnostic technologies required the development of more sensitive and versatile diagnostic tools, in order to enhance screening accuracy and allow the early detection of malignancy onset [He D et al., (2015)].

Ferritin nanoparticle can be labelled with a wide range of dye molecules and tagged with targeting moieties. The resulting constructs can be used as optical imaging probes for both in vivo and in vitro imaging applications [Li X et al., (2012)]. Moreover, the pH-mediated procedure allows to combine differently engineered monomers into hybrid nanoparticles endowed with multiple functionalities [Lin X et al., (2011)].

Most of the diagnostic applications of ferritins are related to the versatility of the *in vitro* mineralization, which allows to internalize labelled heavy atoms and sequestrate them within the mineral core.

Magnetic Resonance Imaging (MRI), for instance, is an highly sensitive and non-invasive technique in tumor imaging that relies on the detection of proton spin alignment under a magnetic field. Paramagnetic contrast agents (such as $Gd^{+3}$) are required to increase the contrast between normal and pathological tissues, but most of them lack specificity for cancer cells. Their broad biodistribution results in the enhancement of all highly vascularized tissues and micrometastasis may not be detected. Hence, the development of novel targeted carrier for MRI contrast agents are still a major concern to overcome these problems.

The iron oxide nanoparticles synthesized inside the ferritin cavity can be employed as contrast agents due to their super-paramagnetic properties and the dark contrast they give in MRI images [Jin R et al., (2014); Uchida M et al., (2006)]. However, native iron containing ferritins often display unsatisfactory degree of cellular selectivity and provide just a poor MRI contrast [Vande VG et al., (2011)]. On this basis, novel recombinant ferritins have been tagged with homing peptides and loaded with elements with higher MRI contrast than iron,

such as gadolinium [Hooker JM et al., (2007)]. A five-nanometer gadolinium nanoparticle have been produced inside ferritin, whose relaxivity was up to 70 times higher than commercially available Gd-chelates [Sanchez P et al., (2009)]. Gadolinium-loaded ferritin has been further engineered with a peptide epitope specific for the neural cell adhesion molecule and successfully employed for the visualization of Endothelial tumour cells [Geninatti CS et al., (2006)]. Mn-loaded ferritin as well has been reported to be a good MRI contrast agent with optimal relaxivity properties [Kalman FK et al., (2010)].

The ferritin capability of internalizing and mineralizing heavy atoms has been also exploited for Positron Emission Tomography (PET) applications. Lin and co-workers managed to load the ferritin nanocage with $^{64}Cu$, a radioisotope commonly used for PET, and further functionalize the outer surface with a fluorescent dye and homing peptide. The obtained probe demonstrated to be suitable for both for PET and fluorescence dually functional imaging [Lin X et al., (2011)].

All these studies highlighted that engineered ferritins hold an impressive potential in targeted diagnostic applications. Moreover, their ability to internalize heavy atoms with broad selectivity suggests their employment as smart nanocarrier for the delivery of metal ions with relevant biomedical properties. Lanthanide ions, for example, are emerging as novel fluorescent probes due to their unique photophysical properties [Handl HL et al., (2005); Hemmila I et al., (2005); Bunzli J., (2006)]. Lanthanides display narrowband emission spectra, large Stokes shift (150-300 nm) and long fluorescence lifetimes, which have been exploited in time-resolved spectroscopy to overcome the short living background signals [Rajapakse HE et al., (2009)]. Unlike traditional organic dyes, they are unaffected by photobleaching or photochemical degradation, which results in prolonged detection [Pandya S et al., (2006)]. Moreover, their fluorescence can be greatly enhanced by Förster resonance energy transfer (FRET) from an appropriately placed sensitizer-fluorophore, a phenomenon often referred to as “antenna effect”. FRET requires spectral overlap between fluorophore emission and lanthanide

absorption spectra and its efficiency relies on the close proximity between the two species (~5-6 Å distance) [Gudgin Dickson EF et al., (1995)]. $Tb^{+3}$ and $Eu^{+3}$ have been widely exploited due to their more intense microsecond fluorescence in the visible region [Selvin PR, (2002); Bunzli JC, (2004)], although several other lanthanides are currently evaluated as candidates for cancer treatment, photodynamic therapy and radiation therapy [Teo RD et al., (2016)].

Proteins are widely known to act both as lanthanide-chelating agents and FRET-sensitizer, due to their acidic and aromatic moieties, and such behavior have been largely exploited to study protein structure, interaction and metal binding properties [Allen JE et al., (2006); Xu X et al., (2002); O'Neil JD et al., (1984)]. However, wide possibilities would arise in biomedical field by combining the optical properties of lanthanides with the biotechnological features of protein nanocarriers.

## 1.4.3: Other applications

Beyond biomedical field, the ferritin scaffold has been successfully employed for several other biotech applications. Just to mention some of the most interesting, the ferritin cage has been exploited as a reaction chamber for the mineralization of different non-physiological metals and metal complexes. Ferritin encapsulated metal nanoparticles display homogeneous shape and atomic composition and can be extracted from the protein envelop through chemical denaturation. The obtained metal particles can be used for the production of ordered semi-conductor arrays, quantum dots, and as anti-bacterial nanoparticles [Yoshimura H, (2006); He D et al., (2015)].
Recently, an industrial-scale process for the water treatment has been developed based on *Pyrococcus furiosus* ferritin [Jacobs JF et al., (2010)]. Ferritin sequesters phosphate within its core along with iron and this feature

can be applied to remove phosphate from water and prevent water pollution and biofouling. Compared to the current methods, the ferritin-based solution is cheaper, highly stable, suitable for recycling and endowed with an high capacity for phosphate binding.

# 2 Aim of the work

Ferritins are emerging as novel biotech platforms for biomedical applications due to their ability to encapsulate cargo molecules, broad functionalization possibilities and selective targeting properties. In this framework, the present work has been focused on the development and characterization of engineered mammalian and archaeal ferritin constructs to expand the scope of their nanotechnological applications.

Two ferritins from Archaea have been chosen as model to further investigate the biological and biophysical properties of prokaryotic homopolymers.

The molecular diffusion through the ferritin cavity appears to be a complex phenomenon that is only partially understood. Despite experimental observations demonstrated that the permeation of small molecule through the mammalian 3-fold channels is a charge-selective process [Yang X et al., (1996); Crichton RR et al., (2010); Douglas T et al (1998)], the molecular diffusion within archaeal ferritins have been little investigated. Differences in the shape, aminoacid composition and electrostatic properties of prokaryotic open pores within these ferritins suggest different routes for small molecules entry and expand the biotechnological relevance of these proteins. In the present work, the *Pyrococcus furiosus* ferritin (Pf-Ft), the "open" *Archaeoglobus fulgidus* ferritin and the "closed" *Archaeoglobus fulgidus* construct (Af-Ft K150A/R151A) have been chosen as model of prokaryotic ferritins. A set of engineered mutants have been obtained by placing a reactive cysteine residue per subunit in the same topological positions either inside or outside the internal cavity. The permeability of the prokaryotic protein shell toward diffusants has been characterized by studying within these mutants the cysteine reactivity toward the bulky and negatively charged DTNB molecule (5,5'-dithiobis-2-nitrobenzoic acid).

Moreover, *Archaeoglobus fulgidus* ferritin has been genetically engineered by changing the surface exposed loop connecting helices B and C to mimic the sequence of the analogous human H-chain ferritin loop. This novel "humanized" chimeric construct (named HumAf-Ft) thus combines the unique open structure and self-assembly properties of Af-Ft with the typical human

H-ferritin ability to bind the Transferrin Receptor TfR-1, which is overexpressed in several types of tumor cells. HumAfFt has been structurally and biophysically characterized and the improved cellular uptake has been demonstrated on HeLa cell line.

Among mammalian isoforms, instead, mouse H-ferritin has been chosen as favoured scaffold for the development of bioimaging tools with potential *in vivo* and *in vitro* applications.

To exploit lanthanide fluorescence properties and develop an intrinsically fluorescent nanoparticle, a novel construct has been developed by genetically fusing at the C-terminal end of mouse H-ferritin a lanthanide binding tag (LBT). LBTs are short peptides (20 or fewer aminoacids) that have been recently designed on the basis of calcium binding loop and selectively bind lanthanide ions at low-nanomolar affinities, thanks to six coordinating aminoacid side chains. They also include a tryptophan residue in its close proximity that provides strong FRET sensitization [Martin LJ et al., (2007)]. Our construct (named HFt-LBT) has been designed by locating the tag inside the inner cavity, so that the lanthanide ions diffusing through the surface pores can eventually bind to the LBT sequence. HFt-LBT would thus act both as carrier targeted to TfR-1 receptor and as a FRET sensitizer. Fluorescence improvement and lanthanide binding properties have been investigated by spectrophotometric measurements using $Tb^{+3}$ as lanthanide probe. The structural characterization has been carried out and cellular uptake by HeLa cell line has been assessed as well.

# 3 Materials and methods

# 3.1 Assembly and molecular permeability of Archaeal ferritin mutants

## *Point mutations and protein expression*

The genes encoding for bacterial ferritin from Af-Ft and Pf-Ft were cloned into the expression vector pET22b (Novagen). Point mutants Af-FtM54C, Af-FtM54C/K150A/R151A, Pf-FtG52C and Pf-FtP77C were obtained by PCR using QuickChange Mutagenesis kit (Stratagene). The recombinant plasmids were transformed into *E. coli* TOP 10 cells and the resulting colonies were screened by DNA sequencing. Plasmids bearing the desired mutations were transformed into BL21(DE3) *E. coli* strain for protein expression. For each mutant, protein overexpression was obtained as follows: 1 L LB broth medium was inoculated with 2 ml overnight culture of a single colony and the gene expression was induced with 1 mM IPTG when the absorbance at 600 nm reached 0.6. Cells were harvested by centrifugation after overnight induction at 37 °C and the cell pellets were stored at −20°C.

## *Protein purification*

Harvested cells form 1 L colture over-expressing Af-FtM54C and Af-FtM54C/K150A/R151A mutants were resuspended in 20 ml buffer A (25 mM HEPES pH 7.5, 20 mM $MgCl_2$) containing a cOmplete™ MiniProtease Inhibitor Cocktail Tablet (Roche) and disrupted by sonication. The soluble fraction was thermally purified by heating at 85 °C for 10 min followed by removal of denatured proteins by centrifugation at 14000 rpm for 30min at 4 °C. The supernatant was fractioned by ammonium sulfate precipitation. 70% ammonium sulfate pellet containing highly purified protein was resuspended in buffer A, dialysed versus the same buffer, sterile filtered and stored at 4 °C. Cells over-expressing Pf-FtG52C and Pf-FtP77C were sonicated in 25mMHEPES buffer at pH 7.5 containing 0.5 mM EDTA, 0.3 M NaCl and

cOmplete™ Mini Protease Inhibitor Cocktail Tablet. After sonication, the crude bacterial extract was digested with DNase for 1 h at 37 °C, heated at 55 °C for 10 min and then at 80 °C for 8min. Heat treatment was followed by centrifugation to remove insoluble material and ammonium sulfate precipitation.70% ammonium sulfate pellet was resuspended in 20mM HEPES pH 7.5 plus 150 mM NaCl, dialysed versus the same buffer and loaded onto a HiLoad 26/600 Superdex 200 pg column (GE Healthcare). Fractions containing highly purified protein were pooled, sterile filtered and store at 4 °C.

## *Preparation of ferritin-DTNB adducts*

All mutants were reduced with 3 mM TCEP (tris(2-carboxyethyl)phosphine) in their storage buffers and then loaded onto a desalting column (GE Healthcare) to remove the reducing agent. Each mutant was reacted with 40-fold molar excess of Ellman's Reagent (DTNB) per cysteine for 3 h at room temperature. Stock DTNB solutions were prepared in ethanol. The excess (non-reacted) reagent was removed by ultra-filtration using 100 kDa Amicon Ultra-15centrifugal devices (Millipore Corporate). The Ferritin–DTNB samples were analyzed by mass spectrometry as described below.

## *Stopped flow experiments*

Kinetic measurements were carried out on a thermostated Applied Photophysics stopped-flow apparatus (Leatherhead, UK) by mixing 8–10 μM protein solutions, previously reduced with TCEP, with solutions containing different concentrations of DTNB (from 0.2 to 0.7 mM after mixing) in 20 mM HEPES, 20 mM $MgCl_2$ pH 7.5. In order to avoid interference of the instrument phototube from the high concentrations of DTNB and the released chromophore 5-thio-2-nitro-benzoic acid(TNB), the reaction was followed at 430 nm and the extinction coefficient calculated to be 12205 $mM^{-1}$ $cm^{-1}$, as

determined from the extinction coefficient of 14150 $mM^{-1}$ $cm^{-1}$ at 412 nm [ Riddles PW et al., (1979)]. All fitting procedures were carried out by using the Matlab software (Mathworks,USA). Experimental traces were fitted by non-linear regression to either exponential of biexponential processes by using an Levenberg-Marquardt algorithm.

## *Self-assembly study*

$MgCl_2$ -mediated self-assembly of ferritin mutants was studied by incubating aliquots of proteins (1 mg/ml) with different salt concentrations in 25 mM HEPES buffer, pH 7.5. Molecular sizes of Af-FtM54C, Af-FtM54C/K150A/R151A, Pf-FtG52C and Pf-FtP77C was determined by size exclusion chromatography (SEC) using HiPrep 16/60 Sephacryl S300 column (GE Healthcare). The column was equilibrated with 25 mM HEPES, pH 7.5, containing $MgCl_2$ at the same concentration in which the protein was pre-incubated and the same buffer was used as mobile phase. Molecular weight of each mutant was determined by comparing their elution volumes with the elution volumes of standard proteins in the same salt concentration. Dynamic light scattering measurements (DLS) were performed using an ALV-5000 logarithmic correlator in combination with a standard optical set-up based on a He–Ne ($\lambda$ = 632.8 nm) 10 mW laser and a photomultiplier detector. The intensity autocorrelation functions were directly obtained as $g2(q, t) = \langle I(q, t)I(q, 0)\rangle/\langle I(q, 0)\rangle 2$, where q is the modulus of the scattering vector defined as $q = (4\pi n/\lambda)\sin(\theta/2)$ ($\theta = 90°$ in the present experiment). Quantitative analysis of the measurements was obtained through a fit of the data with a single exponential expression:$g2(q, t) = 1+be-t/\tau$ where b is the coherence factor and $\tau$ is the relaxation time related to the motion of the particles, specifically to the diffusion coefficient [Berne BJ et al., (1976)].

### *Protein LC–MS*

LC–MS was performed on protein samples before and after DTNB titration, after dialysis in distilled water in the presence of 0.1 mM EDTA, using a Waters Acquity UPLC connected to Waters Acquity Single Quad Detector. A Hypersil Gold C4 column was used: 1.9 μm, 2.1 × 50 mmat 254 nm observation wavelength; mobile phase: 95:5 water (0.1%formic acid):MeCN (0.1% formic acid); gradient over 6 min (to 5:75water (0.1% formic acid):MeCN (0.1% formic acid); flow rate: 0.4 ml $min^{-1}$; MS mode was set at a scan range: m/z = 250–2,000 (ES+); scan time: 0.25 s. Data were obtained *in continuum* mode by setting the electrospray source of the MS with a capillary voltage of 3.5 kVand a cone voltage of 50 V. $N_2$ gas was used as nebulizer and desolvation gas at a total flow of 300 l/h. Ion series were generated by integration of the ultraviolet-absorbance (at 254 nm) chromatogram over 1.2–1.8 min range. Mass spectra were subsequently reconstructed for proteins from the ion series using the MaxEnt 1algorithm on MassLynx software program.

# 3.2 A novel chimeric “Humanized” archaeal ferritin

### *“Humanized” Archaeoglobus ferritin design*

The gene encoding for a mutated ferritin from *Archaeoglobus fulgidus* was synthesised by GeneArt (ThermoFisher) and subcloned into a pET22b vector (Novagen) between the restriction sites NdeI and HindIII at 5′ and 3′ respectively. The recombinant plasmid was transformed into BL21(DE3) *E. coli* strain for protein expression.

## *Protein expression and purification*

*E. coli* cells, containing the HumAfFt plasmid, were grown and induced with 1 mM IPTG (isopropyl-β-D-1-thiogalactopyranoside) at $OD_{600}$ = 0.6. Cells were harvested by centrifugation 3 hours post induction at 37 °C. Cells harvested from 1 L culture were resuspended in 20 mM HEPES buffer, pH 7.5, containing 200 mM NaCl, 1 mM TCEP (tris(2-carboxiethyl)phosphine), and a cOmplete™ MiniProtease Inhibitor Cocktail Tablet (Roche). Cells were disrupted by sonication and the soluble fraction was purified by heat treatment at 78 °C for 10 minutes. Denatured *E. coli* proteins were removed by centrifugation at 15.000 rpm at 4 °C for 1 hour. The soluble protein was further purified by ammonium sulfate precipitation. The precipitated fraction at 70% ammonium sulfate was resuspended in 20 mM HEPES, 50 mM $MgCl_2$, pH 7.5 and dialyzed *versus* the same buffer. As a final purification step, the protein was loaded onto a HiLoad 26/600 Superdex 200 pg column previously equilibrated in the same buffer using an ÄKTA-Prime system (GE Healthcare). The purified protein was concentrated to obtain the final protein preparation of 1 mg $mL^{-1}$ and protein concentration was calculated by measuring the UV spectrum using an extinction coefficient of 32 400 $M^{-1}$ $cm^{-1}$. Protein yield was ∼40 mg $L^{-1}$ culture.

## *Self-assembly assessment in solution*

Size exclusion chromatography $MgCl_2$-mediated self-assembly was studied by size exclusion chromatography (SEC) using a Superdex 200 26/600 GL column (GE Healthcare). The molecular size of HumAfFt was determined under different conditions by comparing the elution volume with that of standard proteins. Composition of the mobile phase was 25 mM HEPES pH = 7.5 with different $MgCl_2$ concentrations accordingly to the composition of the protein buffer.

## *Crystallization and crystal structure determination*

The purified protein was concentrated to 20 mg $mL^{-1}$ and initial crystallization screening was performed using a Phenix Robot. Crystals were obtained by mixing in a 2 µL hanging drop 1 mM of the purified protein with a solution containing 22% (vol/vol) polyacrylic acid PAA, 0.1 M Tris, 0.02 M $MgCl_2$, pH 7.4, at 25 °C within a week, cryo-protected by increasing the precipitant concentration and flash-frozen in liquid nitrogen. Diffraction data have been collected at ID23-2 beamline at the European Synchrotron Radiation Facility (ESRF), Grenoble, France. Data were processed with XDS [Kabsch W, (2010)] and scaled with Aimless (ccp4 suite) at a final resolution of 2.87 Å. The structure was solved by Molecular Replacement with MolRep (ccp4 suite) using the open pore structure AfFt (PDB code 1S3Q) as the search model. Model Building and refinement were done using Coot [Emsley P et al., (2004)] and Refmac5, respectively. The final model was analyzed with PROCHECK [Laskowski RA et al., (1993)] and Molprobity [Chen VB et al., (2010)]. The Ramachandran plot showed that 97.8% of residues are in preferred regions, 2.2% in allowed regions and no outlier is observed. The final atomic coordinates and structure factors were deposited with the PDB Data Bank (http://www.rcsb.org) with accession code: 5LS9.

## *Cryo-Electron microscopy*

Holey-gold grids were prepared as described by Russo and Passmore [Russo CJ et al., (2014)] from Quantifoil R1.2/1.3 (Quantifoil Micro ToolsGmbH, Germany). 3 µL of HumAfFt (12 µM) was applied to the holey-gold grids after plasma cleaning with a mixture of $H_2$ and $O_2$. Grids were blotted for 4 seconds and vitrified by rapidly plunging into liquid ethane at −180 °C ([Dubochet J et al., (1988); Wagenknecht T et al., (1988)]) with a Vitrobot (FEI). Data acquisition was done using a FEI Titan Halo (FEI, Eindhoven) operating at 300 kV. Data sets were imaged with a Volta phase-plate (FEI, Eindhoven) [Danev

R et al., (2014)] and were collected with the automated data collection system EPU (FEI, Eindhoven) at a nominal magnification of 59 000 × on an FEI Ceta camera (FEI, Eindhoven) with a camera pixel size of 14 μm, corresponding to a calibrated pixel size of 1.49 Å on the specimen scale and with a dose of 50 $e^{-}/Å^{-2}$

The particles were picked with the reference-based automated particle picking procedure implemented in RELION 1.3 [Scheres SHW et al., (2015); Chen S et al., (2013)]. CTF correction was not applied since the data were collected within 200 nm of focus and the first CTF zero crossing was well beyond the achievable resolution of the dataset. Those particles were subjected to 2D classification using RELION with k = 100 classes. Good particles were then subjected to 3D classification using RELION with the number of classes K = 8. Resulting classes were refined with the autorefine procedure in RELION. Resolution estimation. Reported resolutions are based on the 'gold-standard' protocol with the FSC = 0.143 criterion using soft masks with an 8 pixel soft edge, and were corrected for the effects of the mask on the FSC curve using high resolution noise substitution **[**Chen S et al., (2013)]. Maps were visualized using UCSF Chimera [Pettersen EF et al., (2004)].

## *Cell line generation*

The HeLa cell line stably expressing an inducible TagRFP-FUS protein (HeLaTagRFP) was generated by transfection with epB-Puro-TT-RFP-FUS wt plasmid and the piggyBac transposase vector. Plasmid construction is described in Morlando M et al., (2012).

## *Protein FITC labeling*

HumAfFt, AfFt and Olo-transferrin were labeled with fluorescein-isothiocyanide (FITC, ThermoFisher) according to the manufacturer's standard protocol. Briefly, 2 mg $mL^{-1}$ of the purified protein was added with

10-fold molar excess of in protein storage buffer stirring for 2 hours at RT. The non-reacted dye was removed by gel filtration chromatography and the fluorescent dye to protein ratio was determined by UV spectroscopy. LC-MS spectrometry measurements on HumAfFt-FITC confirmed that >60% of monomers are FITC-labeled.

## *Cell cultures and ferritin internalization*

HeLa cells were grown at 37 °C in Eagle's MEM supplemented with 10% (v/v) FBS, Glutamax (Invitrogen) and penicillin–streptomycin solution (Sigma). When needed, the cells were induced with doxycycline 0.2 μg $mL^{-1}$. The internalization assay was performed as follows: after seeding the cells on the relevant substrate depending on the experiment, cells were left one day to attach and then incubated with FITC-ferritin nanoparticles (AfFt-FITC, HumAfFt-FITC or Tf-FITC as specified in each experiment) at the final concentration of 30 μg $ml^{-1}$ for the time indicated (1 h, 3 h or 20 h).

## *Flow cytometry analysis*

For flow cytometry analysis HeLa cells were seeded on multiwell plates. Cells were incubated with FITC-ferritin nanoparticles as described previously, then washed two times with PBS, detached with trypsin-EDTA (Euroclone), washed with PBS and resuspended in BD-FACS flow buffer. Half of each sample was treated with Trypan Blue (TB; Sigma) to quench the FITC signal from membrane-bound nanoparticles that were not internalized. The quenching was performed with 0.04% TB for 10 min on ice. Control cells were treated in the same way but without FITC-ferritin incubation. Internalization of ferritins before and after TB treatments was measured at the BD LSFORTESSA (BD Biosciences, San Jose, CA, USA) equipped with a 488 nm laser and FACSDiva software (BD Biosciencesversion 6.1.3). Live cells were first gated by forward and side scatter area (FSC-A and SSC-A) plots,

then detected in the green channel for FITC expression (530/30 nm filter) and side scatter parameter. The gate for the final detection was set in the control sample. Data were analyzed using FlowJo9.3.4 software (Tree Star, Ashland, OR, USA).

### *Confocal microscopy of live cells*

To visualize ferritin internalization by live cells using a confocal microscope, HeLa TagRFP cells were seeded on a μ-slide 8-well ibiTreat (ibidi) and induced with 0.2 μg $mL^{-1}$ of doxycycline. Cells were then incubated with FITC-ferritin nanoparticles as previously described for 20 h and, before microscopy, cells were washed two times with an imaging medium (DMEM without phenol red, 10% FBS, 10 mM Hepes, Glutamax and penicillin–streptomycin solution) to eliminate the unbound FITC-nanoparticles. The confocal laser-scanning microscope used was an Olympus FV10i platform equipped with a built-in incubator. Images were acquired with a 60×/1.2NA water-immersion objective, LD lasers, 473 nm and 559 nm, and filter sets for FITC and TRITC. Phase-contrast images were acquired simultaneously.

# 3.3 Engineered mammalian ferritin for lanthanide binding

### *2.1 Protein design, expression and purification.*

A synthetic gene encoding for mouse H-chain ferritin (HFt) fused with a lanthanide binding peptide (LBT) was designed, synthesized, and optimized for *Escherichia coli* codon usage by Geneart (Geneart AG). LBT sequence

YIDTNNDGWIEGDELLA [Martin LJ et al., (2007)] was added to the C-terminal of HFt generating HFt-LBT construct, that was subcloned into pET22-b vector (Novagene) between NdeI/XhoI restriction sites. HFt-LBT was overexpressed in *Escherichia coli* BL21 cells upon induction with 1 mM IPTG (Isopropyl-β-D-1-thiogalactopyranoside) at $OD_{600}$=0.6. Cells were harvested by centrifugation 16 hours post induction at 37°C. Cells harvested from 1 L culture were resuspended in 20 mM HEPES buffer, pH 7.5, containing 200 mM NaCl, 1 mM TCEP (tris(2-carboxiethyl)phosphine), and a cOmplete TM Mini Protease Inhibitor Cocktail Tablet (Roche). Cells were disrupted by sonication and the soluble fraction was purified by heat treatment at 78°C for 10 minutes. Denatured *E. coli* proteins were removed by centrifugation at 15.000 rpm at 4°C for 1 hour. The soluble protein was further purified by ammonium sulfate precipitation. The precipitated fraction at 70% ammonium sulfate, was resuspended in 20 mM HEPES, 50 mM $MgCl_2$, pH 7.5 and dialyzed versus the same buffer. As final purification step, the protein was loaded onto a HiLoad 26/600 Superdex 200 pg column previously equilibrated in the same buffer using an ÄKTA-Prime system (GE Healthcare). Purified protein was concentrated to obtain the final protein preparation of 1 mg/mL and protein concentration was calculated by measuring the UV spectrum using an extinction coefficient of 32400 $M^{-1}cm^{-1}$. Protein yield was ~50 mg/l culture.

## *Fluorescence spectroscopy*

Fluorescence spectra and titrations were performed using FluoroMax 4 (Horiba) spectrofluorimeter with a Haake D8 refrigerated bath at 20 °C. Emission spectra were recorded between 450 and 560 nm, in order to include the luminescent maxima of Tb(III) (490 and 545 nm). The excitation wavelength was chosen at 295 nm to minimize the overlap of second order diffraction (570 nm) with the Tb(III) emission at 545 nm. Emission spectra were taken with excitation and emission band passes of 4 and 8 nm and corrected for the blank contribution and the instrument response at 295 nm in

a quartz cell of 1 cm pathlength. Emission spectra were normalized to 1 at 545 nm.

Fluorescence measurements were performed using 1 μM apoHFt-LBT and apoHFt as a control in 100 mM MES buffer pH 6.4. A 50 mM $TbCl_3$ (Aldrich) stock solution was also prepared in MES buffer at pH 6.4. Fluorescence spectra were recorded upon 30 min incubation with excess of $TbCl_3$ in buffer solution followed by a washing step to remove the unbound metal. Titration data were obtained by addition of aliquots of $TbCl_3$ in buffer solution under continuous stirring.

## *Cryo-Electron microscopy*

After plasma cleaning with a mixture of $H_2$ and $O_2$, 3 μl of a solution containing 1 μM HFt-LBT Tb(III) complex was applied to holey-gold grids from Quantifoil R1.2/1.3 (Quantifoil Micro Tools GmbH), prepared as described [Chen S et al., (2013)]. After 30 s waiting time, grids were blotted for 3 seconds at 100% humidity with filter paper and vitrified by rapidly plunging into liquid ethane at −180 °C [32, 33] with a Vitrobot Mark IV (FEI).

Data acquisition was performed using a FEI Titan Halo (FEI, Eindhoven) operating at 300 kV, while the specimen was maintained at liquid nitrogen temperatures. Datasets were collected with an automated data collection system [Winn MD et al., (2011)] on a K2 Summit direct detector camera (Gatan, Pleasanton) operating in super-resolution mode, with a calibrated pixel size of 1.15 Å on the object scale and a magnification of 59 000×. Images were typically recorded with a defocus range between −0.7 and −3.0 μm and a dose of electrons on the specimen plane between 10 and 20 electrons/$Å^2$.

Data analysis was completely carried out using RELION 2.0 [Adams PD et al., (2010)]. CTF correction was done using MotionCor2 [McCoy AJ et al., (2007)]. Particles were picked and extracted from the original micrographs with the reference-based automated particle picking procedure implemented in RELION [Emsley P et al., (2004)]. Particles were then 2D classified using 100 classes. 2D good classes were selected and then subjected to 3D classification with 8 classes, using as reference model the mouse H-ferritin structure (PDB

code 3WNW). Resulting good classes were refined with the 3D Autorefine procedure in RELION.
The final 3D map resolution is calculated with the FSC = 0.143 criterion, based on the 'gold-standard' protocol [Laskowski RA et al., (1993)], using soft masks with a 4 pixel soft edge, and has been corrected for the effects of the mask on the FSC curve using high-resolution noise substitution [Chen VB et al., (2010)]. This final map was visualized using UCSF Chimera [Zheng H et al, (2017)].

## *Crystallization and X-ray structure determination.*

Crystals of apoHFt-LBT and HFt-LBT in complex with Tb(III) were obtained by mixing in a 2µl hanging drop the purified protein at 15 mg/ml with a solution containing 1.8/2.0 M ammonium sulfate and 0.1 M Tris, pH 8.5, at 25° C within a week, cryo-protected by extensively washing the crystals in sodium malonate and flash-frozen in liquid nitrogen. Diffraction data were collected at XRD1 beamline at the Elettra Synchrotron, Trieste, Italy.
Data were processed with XDS [Russo CJ et al., (2014)] and scaled with Aimless [Dubochet J et al., (1998)] at a final resolution of 2.85 and 2.65 Å. The structures were solved by Molecular Replacement with Phaser [Wagenknecht T et al., (1988); Suloway C et al (2005)] using the structure of mouse H-chain modified ferritin (PDB code 3WNW) as search model. Model building and refinement were done using Coot [Scheres SH, (2012)] and Refmac5, respectively. The final model was analyzed with PROCHECK [Zheng SQ et al., (2016)] and Molprobity[Scheres SHW, (2015)]. Ramachandran Plot showed more than 98 % residues are in preferred regions and no outlier is observed in both structures. The validation of metal binding sites was performed using CheckMyMetal web server [Rosenthal PB et al., (2003)]). The final atomic coordinates and structure factors were deposited with the PDB Data Bank (www.rcsb.org) with accession code (5OBA and 5OBB, respectively). Complete data collection and refinement statistics are reported in Supplementary Data (Table 1).

## *Cell cultures and ferritins internalization*

Human prostate cancer cell line DU-145 (ATCC® HTB81™), human colorectal cancer cell line HCT-116 (ATCC® CCL-247™), human breast cancer cell line MDA-MB-231 (ATCC® HTB-26™) and human ovarian cancer cell line SKOV-3 (ATCC® HTB-77™) were cultured in DMEM medium containing 10% FBS, 100 μg/ml streptomycin and 100 U/ml penicillin G in a humidified 37 °C incubator. The internalization assay was performed as follow: cells were detached using trypsin, then washed twice with PBS and resuspended in non-supplemented DMEM medium containing FITC-ferritin nanoparticles (HFt-LBT or mouse HFt as a control) at the final concentration 0.5 mg/ml for 1 hour in a humidified 37 °C incubator. After incubation cells were washed three times with PBS and subjected for confocal microscopy and flow cytometry analysis.

## *Confocal microscopy*

Following internalization step described above, cells were seeded into 8-well Nunc™ Lab-Tek™ Chambered Coverglass with 200 μl DMEM medium containing 10% FBS, 100 μg/ml streptomycin and 100 U/ml penicillin G per well. Chambers with cells were then incubated on ice until microscopic visualization. Images were acquired using an inverted confocal microscope IX70 FV 500 (Olympus), with 488 nm laser, 20x objective lens and emission filter 505-560 nm. Image processing was performed using ImageJ software (National Institutes of Health, www.imagej.nih.gov/ij/).

## *Flow cytometry analysis*

Cells were incubated with FITC-ferritin nanoparticles as described previously then washed three times with PBS, and resuspended in FACS buffer (2% FBS, 1 mM EDTA). Internalization of ferritins before and after treatments was measured at the BD FACSAria™ III equipped with a 488 nm laser. Cells were first gated by forward and side scatter area (FSC-A and SSC-A) plot and for singlets population (FSC-H and SSC-A), then detected in the channel for FITC

expression (530/30nm filter) and side scatter parameter. The gate for the final detection was set according to the gate set on the control sample. Data were analyzed using BD FACSDIVA™ and FlowJosoftwares.

# 4 Results and Discussions

# 4.1 Assembly and molecular permeability of Archaeal ferritin mutants

## 4.1.1: Molecular design of Archaeal ferritin mutants

Molecular diffusion in and out of the ferritin cavity appears to be a complex phenomenon that is only partially understood. Several works demonstrated that in mammalian ferritins small organic molecules can access to the inner cavity through the same negatively charged 3-fold channels that govern metal ions fluxes [Yang X et al., (2000); Zhang B et al., (2006)]. In both vertebrate L- and H-chains this process is charge-selective, as only molecules endowed with cationic properties can permeate the 3-fold channels while negatively charged probes are completely excluded [Yang X et al., (1996); Crichton RR et al., (2010); T. Douglas T et al (1998)]. Electrostatic properties and lining aminoacids of archaeal 3-fold channels importantly diverge from those of mammalian, thus implying different routes for small molecules entry within these ferritins. However, the diffusion of small molecules within archaeal ferritins have been little investigated.

To this purpose, we engineered a set of Pf-Ft, Af-Ft ("open") and Af-Ft K150A/R151A ("closed") mutants by placing reactive cysteine residues in the same topological positions either inside the 24-mer cavity (namely in Af-FtM54C, Af-FtM54C/K150A/R151A and Pf-FtG52C mutants) or outside the 24-mer cage (in the Pf-FtP77C mutant). In this framework, the access to the reactive sulfidryls is totally unhindered on the protein external surface in Pf-FtP77C, partially hindered in the internal cavity in Af-FtM54C and totally hindered in the internal cavity in Af-FtM54C/K150A/R151A and Pf-FtG52C (see Fig. 4.1). Assembly properties of these mutants were investigated. Moreover, the permeability of ferritin shell towards molecular diffusants was assessed by probing in kinetic measurements the reactivity of the cysteine

residue towards the bulky and negatively charged DTNB (5,5′-dithiobis-2-nitrobenzoic acid) molecule.

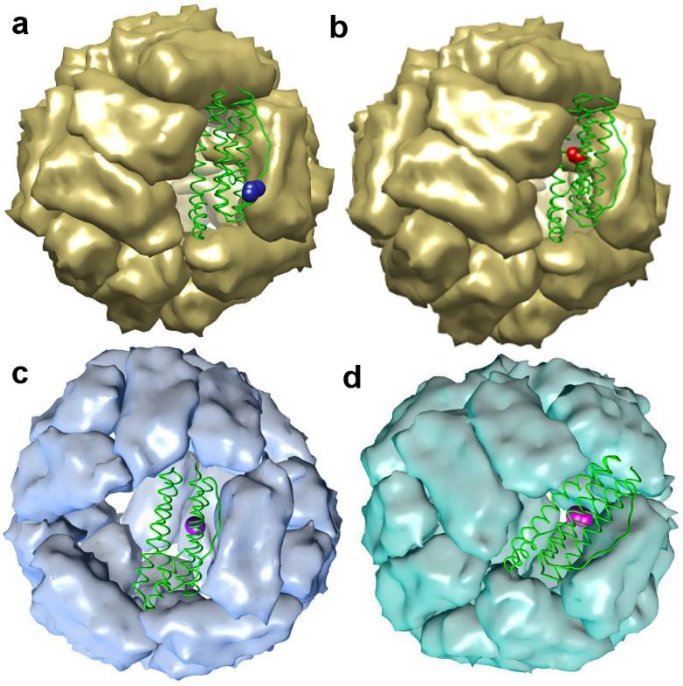


**Fig. 4.1: Three-dimensional structures of the ferritin mutants.** A monomer is depicted as green ribbon and the cysteine residues are represented in CPK style for clarity. a) Pf-Ft P77C: the external cysteine is shown as blue spheres. b) Pf-Ft C52C: the internal cysteine is depicted in red. c) Af-Ft 54C: the internal cysteine is depicted in purple. d) Af-Ft M54C/K150A/R151A: the internal cysteine in magenta. Molecular graphics and analyses were performed with the UCSF Chimera package [Pettersen EF et al., (2004)].

## 4.1.2: Structural and association properties of Archaeal Ferritin mutants

The association state of the engineered ferritin mutants was studied as a function of $MgCl_2$ concentration by Dynamic Light Scattering (DLS) and Size-Exclusion chromatography (SEC). As expected, Pf-Ft mutants retained their tetraeicosameric structure independently of salt concentration (see Fig. 4.2) while the self-assembly of both Af-Ft mutants was strongly dependent on ionic strength.

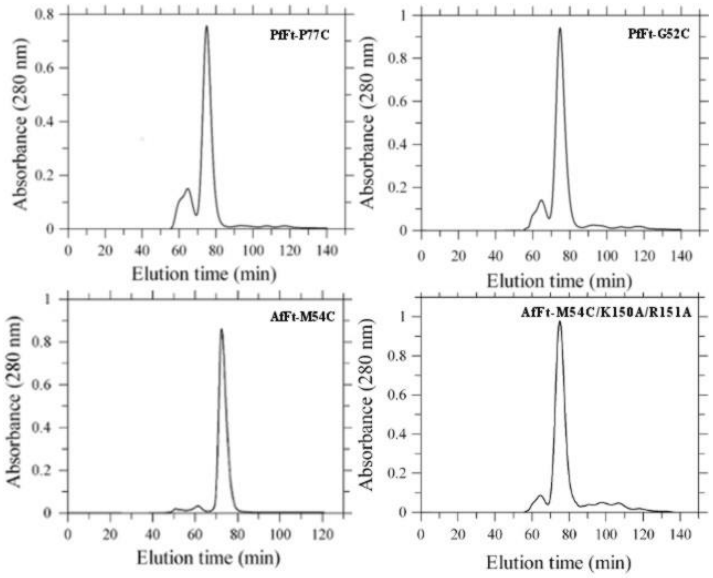


**Figure 4.2: Size exclusion chromatography profiles of ferritin mutants**. The characteristic SEC profiles obtained at 20mM HEPES pH. 7.4, 20mM $MgCl_2$, for mutants PfFt-P77C, PfFt-G52C, AfFt-M54C and AfFt-M54C/K150A/R151A (right to left, top to bottom) are represented.

A full characterization of Af-FtM54C is reported in Fig. 4.3. As shown by DLS measurements (Fig 4.3(a)), the shape of the curve obtained in the presence of salt was significantly different from that without salt. The fitting curves appeared to interpolate very well experimental data in presence of divalent cations, while an heterogeneous and polydisperse population was observed in the absence of added salt. This profile pointed out that in the absence of divalent cations Af-Ft mutants largely exists as a mixture of both low molecular weight species (most likely dimers [Treffry A et al., (1984); Johnson E et al., (2005); Sana B et al., (2013)]) and high molecular weight polymers arranged in a proportion even higher than the canonical 24-mers (the latter specie was present in much lower amount). The addition of $MgCl_2$ at 5–10 mM concentration induced a very sharp transition in both Af-Ft mutants resulting in the formation of homogeneous and stable 24-mer species. At 20 mM $MgCl_2$ concentration, all proteins investigated were consistent with a stable 24-mer assembly.

Notably, we used $MgCl_2$ as polymerizing salt in spite of NaCl as previously described. Sana and co-workers reported that at least 100 mM NaCl was required to make the Af-Ft K150A/R151A mutant exists as a stable tetraeicosamer, while even higher NaCl concentrations were needed for the wild type Af-Ft [Sana B et al., (2013), Johnson E et al, (2005)]. In our experiments instead the full assembly of both Af-FtM54C and Af-FtM54C/K150A/R151A mutants was achieved at 20 mM $MgCl_2$, thus probing that divalent cations such as $Mg^{2+}$ and $Ca^{2+}$ are more effective in promoting the 24-mer association with respect to NaCl.

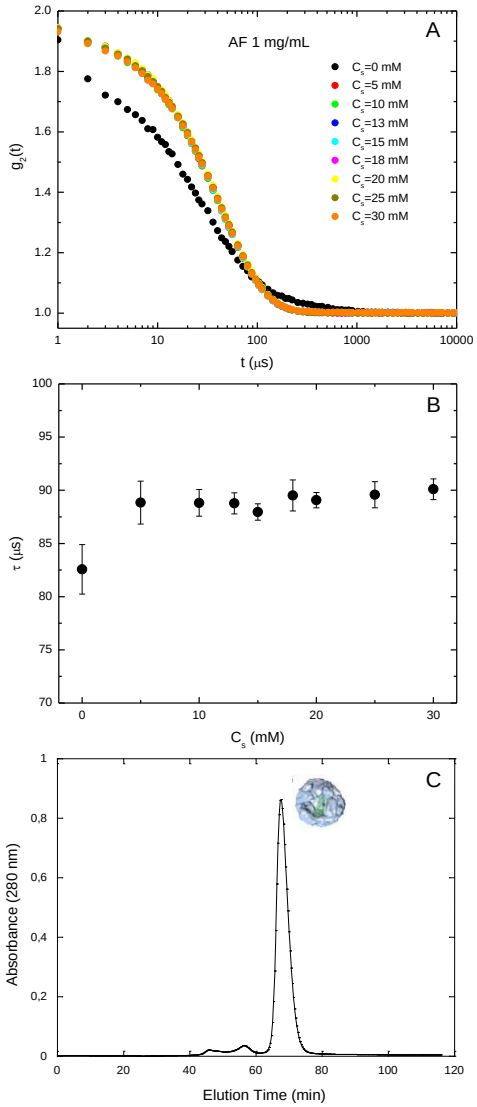


**Fig. 4.3. Polymeric assembly of *Archaeoglobus fulgidus* ferritin mutants.** A) Dynamic Light Scattering intensity correlation functions of Af-FtM54C at different $MgCl_2$ concentrations indicated in the legend. The curves at different $MgCl_2$ are all superimposed. B) Dynamic Light scattering relaxation time of Af-FtM54C as a function of $MgCl_2$ concentrations. C) Gel filtration profiles of Af-FtM54C at 20 mM $MgCl_2$.

## 4.1.3: Molecular diffusion properties of Archaeal Ferritin mutants

After confirming the quaternary structure of these mutants, the permeability of the archaeal protein shell towards molecular diffustants was assessed. The inner cavity accessibility for each mutant was characterized by probing the thiol reactivity of cysteine residue towards the bulky and negatively charged DTNB (5,5′-dithiobis-2-nitrobenzoic acid) molecule. DTNB is a ~6 Å diameter probe that quickly reacts with protein thiol groups cleaving the disulphide bond to yield the coloured dianionic specie $TNB^{-2}$. This reaction is stoichiometric, as each mole of protein reactive thiol releases one mole of $TNB^{-2}$ [Riddles PW et al., (1979)]. Moreover, neither *Pyrococcus furiosus* nor *Archaeoglobus fulgidus* native proteins bears other reactive cysteine residues apart from the one we genetically introduced, thus ruling out the possibility of spurious reactivity of DTNB molecule.

The kinetics of the disulfide exchange reaction of DTNB with cysteine residues were followed by stopped-flow spectroscopy and recorded up to 1000 seconds. For each mutant, a complete set of time courses was carried out under pseudo-first order conditions by increasing DTNB concentration while keeping protein concentration constant. As shown in Fig 4.4, all the obtained kinetics displayed multiexponential profiles while the time scales were significantly different within the four ferritin mutants.

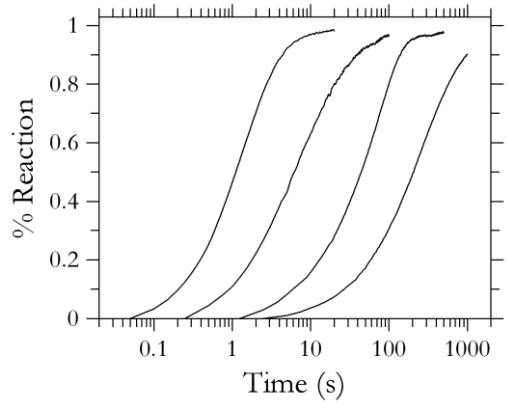


**Fig. 4.4. Kinetics of DTNB binding to Af-Ft and Pf-Ft mutants.** Comparison of the reaction time scales of all mutants; from left to right, Pf-Ft P77C, Af-Ft M54C, Af-Ft M54C/K150A/R151A, and Pf-Ft G52C. All mutants were 5 µM except Af-Ft M54C which was 4 µM, and DTNB was 0.7 mM.

All measured traces have been fitted by non-linear regression to either exponential or bioexponential processes and the apparent second-orded constants are reported in Table 4.1 and Fig 4.5. As expected, the Pf-Ft P77C mutant bearing the cysteine residue on the convex outer surface displayed the fastest reactivity as compared to Pf-Ft G52C, which carries the mutation inside the ferritin tetraeicosamer. The Af-Ft mutants had an intermediate behaviour in the reaction with DTNB. Quite unexpectedly the Af-FtM54C mutant, in which the internal cysteine reacts with DTNB in a facilitated way through the four 45-Å large triangular openings in the protein shell, could only be fit by a biexponential process in which the fastest second-order rate constant was of the same order of magnitude determined for the Pf-Ft P77C mutant (Table 4.1). Finally, closure of the openings by introduction of the K150A/R151A mutations in Af-M54C brought about a significant quenching of the ligand binding rate.

| *Protein* | *Cysteine position* | $k_{OBS}$ ($M^{-1}s^{-1}$) |
|---|---|---|
| Pf-Ft P77C | external | 908 ± 122 |
| Pf-Ft G52C | internal | 5 ± 1 |
| Af-Ft M54C open | internal | fast: 198 ± 65<br>slow: 51 ± 21 |
| Af-Ft M54C/K150A/R151A closed | internal | 26 ± 2 |

**Table 4.1. Apparent second-order constants for ferritin mutants as determined by the DTNB reaction.**

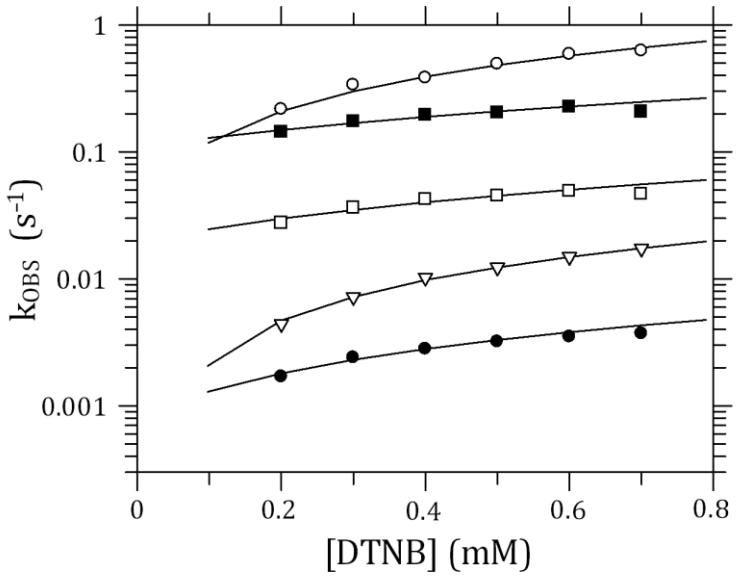


**Figure 4.5: Pseudo-first order plot of the observed rate constants as a function of DTNB concentration.** Open and closed circles: Pf-Ft P77C and Pf-Ft G52C, respectively; closed and open square: the fast and slow phases of Af-Ft M54C, respectively; open triangles: Af-Ft M54C/K150A/R151A. All reported concentrations are after mixing and experiments were carried out at 20 °C in 20 mM Hepes, 20 mM $MgCl_2$, pH 7.5.

Additional LC–MS measurements were performed on the four ferritin mutants after titration with DTNB in comparison with unreacted proteins (see Fig. 4.6). Unreacted ferritins were eluted as monomers of molecular weight of about 21 kDa while DTNB reacted proteins showed a shifted peak of +198 ± 2 Da, in agreement with the expected molecular weight of the thio-nitrobenzoic moiety. In all samples the reaction was complete with the exception of Pf-Ft G52C protein, in which 18 % of unreacted protein was present.

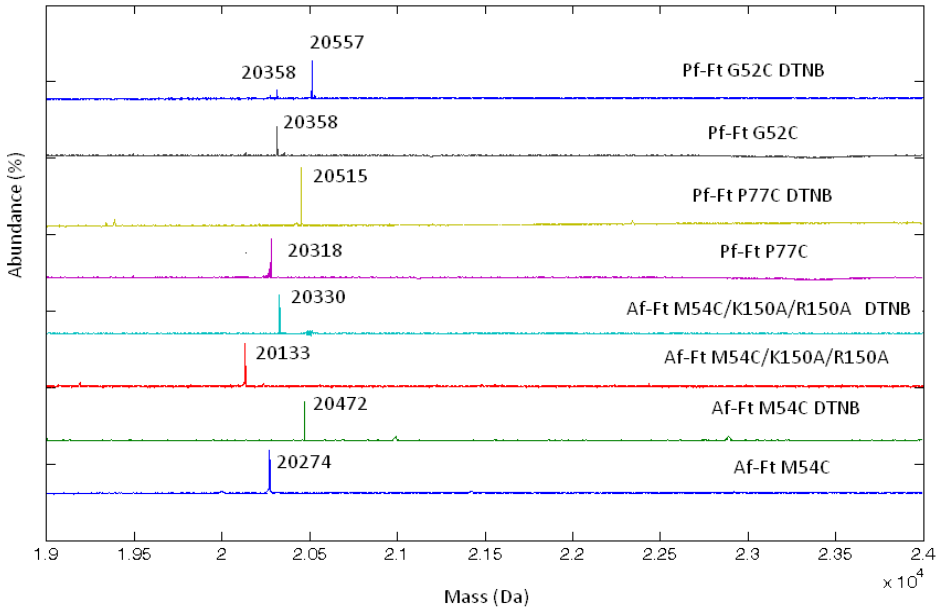


**Fig. 4.6: Ferritin mutants LC–MS measurements.** LC–MS measurements carried out on Af-FtM54C, Af-FtM54C/K150A/R151A, Pf-FtG52C and Pf-FtP77C after titration with DTNB in comparison with unreacted proteins. Each mutant is eluted as monomer (21 kDa) and DTNB reacted proteins show a shifted peak of +198 ± 2 Dalton, in agreement with the expected molecular weight of the thio-nitrobenzoic moiety.

These data demonstrated that the bulky and negatively charged DTNB molecule can permeate archaeal ferritin shells even in their fully assembled and closed structure. This behaviour is quite relevant in view to the opposite properties displayed by mammalian ferritin, that allows the exclusive entry of positively or neutral species [Crichton RR et al., (2010); Douglas T et al., (1998)]. Charge selectivity was demonstrated in horse spleen ferritin (HoSF) and human H-chain ferritin (HuHF) and correlated to the hydrophilic and negatively charged nature of threefold channels. Negatively charged nitroxide probes were in fact completely excluded from the interior of the protein, while positively charged and polar nitroxide radicals penetrated the protein shell to interact with the iron core [Yang X et al., (1996); Desideri A et al., (1991)]. At the same time, the genetical introduction of positively charged groups along the 3-fold channels switched the electrostatic properties of the pores and allowed the entry of negatively charged probes in mutated ferritins [Harrison PM et al., (1986); Treffry A et al., (1984); Yang X et al., (2000)].

Notably, the first-order half-lives that have been observed for the permeation of positively charged compounds in mammalian ferritins are in the same time range of those we found in DTNB uptake in fully closed Af-FtM54C/K150A/R151A and Pf-FtG52C ferritins. Since in both mammalian and prokaryotic ferritins the 4-fold channels are too narrow to allow the migration of any molecular species except for protons, we concluded that that even in archaeal ferritin the 3-fold channels represent the only possible route for the entry and the exit of small organic molecules.

The different specificity of the prokaryotic ferritin towards charged diffusants can be explained by comparing the lining aminoacids of the 3-fold channels between *Archaeoglobus fulgidus*, *Pyrococcus furiosus* and human H-chain (as reported in Fig 4.7). In all these proteins, the outer entrance of the pore is defined by C-terminal ends of helices C while the inner entrance by N-termini of helices D. Pf-Ft and HuHF share a similar arrangement in the outer region of the channel that is rich in negative aminoacids (Glu109, Glu110 and Glu111), while differ in the central site due to the presence of polar and

positively charged residues in Pf-Ft (Tyr114 and Arg117) [Beheraa RK et al., (2014)].

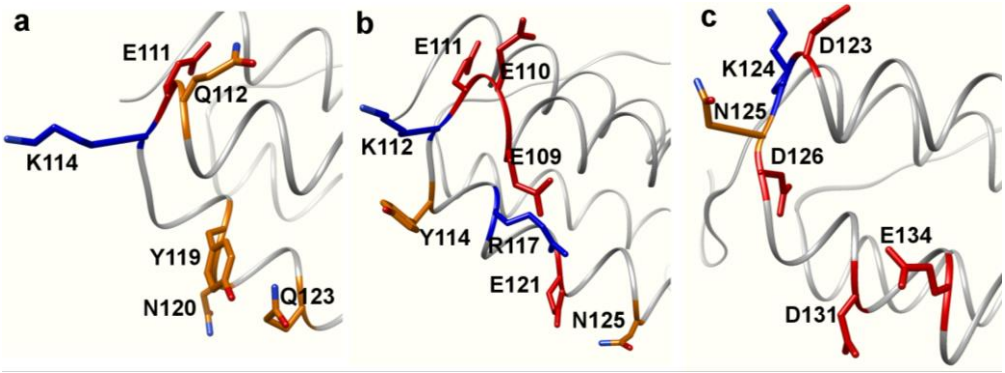


**Fig. 4.7:** Profile view of the lining amino acids in the threefold channel in a) Af-Ft (PDB ID: 1SQ3) and b) Pf-Ft ((PDB ID: 2JD6) with respect to c) HuHF (PDB ID: 2FHA). The exterior of the shell lies on the left side and the inner cavity on the right side of each cartoon as shown schematically. Positive, negative and polar residues are depicted as blue, red and orange sticks, respectively.

The outer entrance of Af-Ft pore, instead, does not display the negative cluster characteristic of HuHF: only one glutamate (Glu113; PBD ID: 1SQ3 and 3KX9) is located to the entrance while two acidic residues lining HuHF channels (Asp131 and Glu134) (PDB ID:2FHA) are replaced by neutral and positively charged residues (Tyr119 and Asn 120). Hence, the threefold channels of archaeal ferritins are less negatively charged than the mammalian ones and possibly allow the entrance of negatively charged compounds.

The pores of Af-Ft, in particular, are endowed with the lowest negative electrostatic potential due to their singular aminoacidic arrangement. This is supported by the evidence that the DTNB entry rate into Af-

FtM54C/K150A/R151A mutant is 5 fold faster than in the Pf-FtG52C protein (see Table 4.1). Such finding is relevant in view of the fact that the last two proteins are assimilated to closed cages with thiols in topologically equivalent positions. Of course, the "open" Af-FtM54C displays the typical four 45 Å wide triangular pores that are characterized by the presence of a group of positive charged residues located at the three apices [Johnson E et al., (2005)]. These large openings provide a preferential path into the cavity for large ligand entry, as demonstrated by the 8 fold faster DTNB reaction rate with the internal thiol with respect to the closed Af-FtM54C/K150A/R151A mutant.

These findings pointed out that archaeal ferritins from *Pyrococcus furiosus* and *Archaeoglobus fulgidus* are able to incorporate bulky and negatively charged species even in their fully "closed" forms. Molecular diffusion most likely occurs through the threefold channels, whose nature appears less restrictive with respect to that of vertebrate proteins. This feature can be arguably related to the presence of positively charged residues in the middle of the threefold channel, that favour entrance of negatively charged species in the archaeal proteins. As a last comment, it must also be pointed out that the dimensions of the currently used probe slightly exceed the diameter of the threefold channel as inferred from crystal structure coordinates. A mechanism of rotameric adjustment of relevant aminoacid side chains is thus necessary in order to allow for the entry/exit of small organic molecules. Recent demonstration of multiple conformers in aminoacids lining the inner entrance to the ferritin cavity may explain the necessary plasticity of the threefold channels in ferritins [Beheraa RK et al., (2014)].

# 4.2: A novel chimeric “Humanized” archaeal ferritin

## 4.2.1: Molecular design of chimeric HumAf-Ft

Human H-ferritin (HuHF) has been proficiently used as nanocarrier for cancer diagnosis and therapy [Liang M et al., (2014); Vannucci L et al., (2015); Falvo E et al., (2013); Vannucci L et al., (2012)], due to its ability to selectively deliver bioimaging or therapeutic agents to tumor cells overexpressing the transferrin receptor TfR-1 [Fan K et al., (2012)]. TfR-1 represents a preferred target for human H-ferritin, as specific interactions occur between the extracellular moiety of the receptor and the epitopes of H-ferritin subunit [Heger Z et al., (2014); Li L et al., (2010)]. However, the extremely acidic conditions required for the encapsulation of payload compounds within the protein shell implies a certain degree of pH-resistance to the drug and still represents a major experimental limit. This procedure generally leads to suboptimal load of cargo material and, due to the pH jump, the protein reassembly is only partially reversible [Zhen Z et al., (2014); Mihee K et al., (2011)].

The *Archaeoglobus fulgidus* ferritin is certainly a more versatile scaffold for the incorporation of diverse substructures inside the protein cavity, either by an assembly/disassembly process at neutral pH or by diffusion through the large triangular pores on the surface. Notable examples have been reported in recent literature [Sana B et al., (2015)]. Nevertheless, human H-chain ferritin and *Archaeoglobus* ferritin display a sequence identity lower than 31% (PDB code 3AJO and 1S3Q, respectively), which runs against the possibility of recognition of Af-Ft by TfR-1 receptors in mammalian cells.

On this basis, we engineered the *Archaeoglobus fulgidus* ferritin by mutating the surface exposed loop of 12 amino acids connecting B and C helices to

reproduce the sequence of the analogous human H-chain ferritin loop. This chimeric construct, named “Humanized Archaeoglobus ferritin” (HumAf-Ft), was developed to combine the unique structural and cargo incorporation properties of Af-Ft with the TfR-1-mediated binding and cellular uptaking characteristic of HuHF.

HumAf-Ft has been designed on the basis of preliminary investigation of the external surface of human H-homopolymer, aimed to identify the putative region involved in TfR-1 receptor interaction. Despite the high degree of accessibility, neither the N-terminal regions nor the outer entrance of 3-fold channels seem to be required for the receptor recognition or uptake, as confirmed by the evidence that N-terminal or C-terminal deleted human H-homopolymers are still efficiently taken up by target cells [Levi S et al., (1988)]. The most exposed area of ferritin outer surface, instead, is represented by the long external loop of 12 aminoacids connecting B and C helices (up to 19 aa including the turn regions). Therefore the BC loop, besides its structural role in stabilization of the interdimer interface, [Bernacchioni C et al., (2014)] appeared to be the best candidate for TfR1 receptor recognition of the ferritin molecule.

As shown in Fig. 4.8, the BC loops of two adjacent subunits run in an antiparallel fashion establishing significant, mutual interactions. Thus the BC loops of adjacent subunits display the same overall geometry in both HuHF and Af-Ft, though each couple of loops adopts a different symmetry along the spherical surface of the protein cage, given the different dimer–dimer positioning within each complete 24-mer structure.

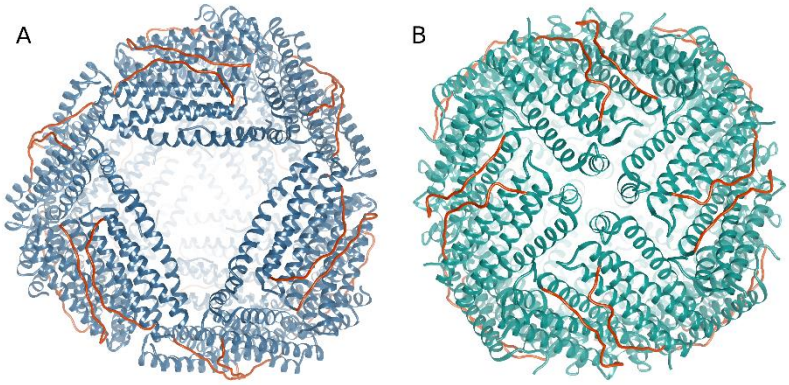


**Fig. 4.8 Three-dimensional structures determined by X-ray crystallography.** A cartoon representation of (A) HumAf-Ft and (B) HuHF (pdb code 3AJO). Models are coloured in blue and green, respectively, and the external loop connecting the helices B and C of each monomer is shown as red ribbons. Molecular graphics were performed using a UCSF Chimera package. [Pettersen EF et al., (2004)]

In order to preserve the unique assembly properties of Af-Ft, while implementing a potential cellular uptake, we decided to exploit this external loop by mutating 9 residues into the corresponding residues found in HuHF, according to the sequence alignment shown in Fig. 4.9. In particular, the nine amino acids sequence IFLQDIKKP, typical of a human H ferritin homopolymer, located at the center of the 12 aa loop was inserted in place of VKLYAVEEP (from residue 70 to 79 in Af-Ft numbering, see Fig. 4.9). In addition, a cysteine residue in position 54 (Af-Ft numbering) has been introduced by point mutation in order to provide a conjugation site of potential thiol reactive derivatives into the cavity.

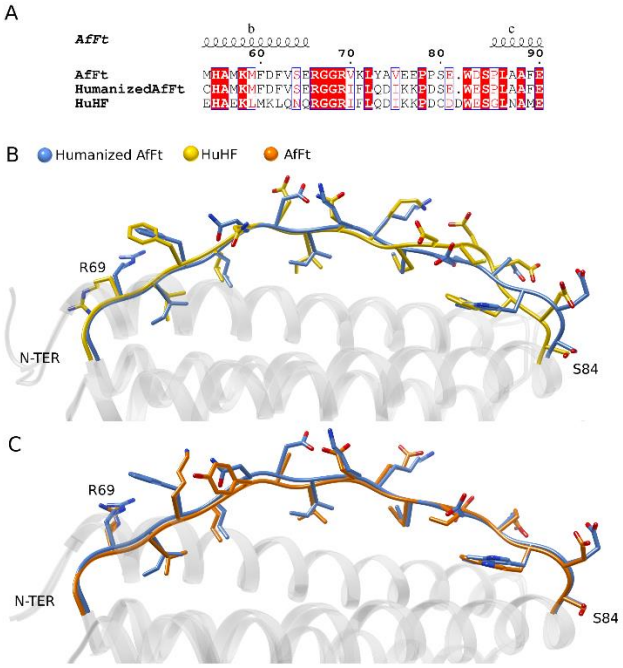


**Fig. 4.9 Structure-based sequence alignment of Af-Ft, HumAf-Ft, and HuHF.** (A) Close-up view of the sequence alignment. Elements of secondary structure for the Af-Ft are shown on the top. White characters in a red background indicate strict conservation while residues with poor conservation are drawn in black on a white background. Alignments were made using CLUSTAL Omega, and the figure was generated using ENDSCRIPT. [Robert X et al., (2014)]. The structural superposition of the region from R69 and S84 (Af-Ft numbering) is shown in (B) HumAfFt (in blue) vs. HuHF (in yellow) and in (C) HumAfFt (in blue) vs. Af-Ft (in orange). Residues are depicted as sticks indicating N atoms in blue, O atoms in red and S atoms in yellow.

## 4.2.2: Structural and biophysical properties of HumAf-Ft

The overall assembly properties of chimeric protein HumAf-Ft were assessed by size exclusion chromatography (SEC) as a function of $MgCl_2$ concentration. $MgCl_2$ was used as polimerizing agent on the basis of our previously reported work on archaeal ferritins. Identical peak-positions confirmed that HumAf-Ft retains the $MgCl_2$-mediated disassembly/assembly equilibrium of native Af-Ft, which occurs under neutral pH conditions. As shown in the Fig. 4.10, at low ionic strength HumAf-Ft mainly existed as dimeric species, while the increasing of $MgCl_2$ concentration triggered the self-assembly of dimers into a stable polymeric structure of ~500 kDa (corresponding to the expected molecular weight of tetraeicosameric structure). As mentioned for the archaeal mutants in the previous part, the full assembly of HumAfFt 24-mer was reached at 20 mM $MgCl_2$.

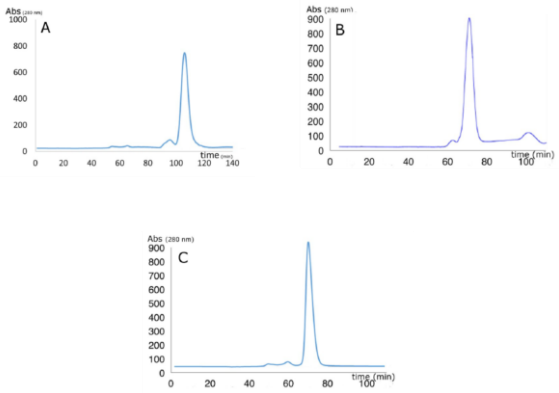


**Fig. 4.10: $MgCl_2$-mediated self-assembly of HumAf-Ft by Size Exclusion Chromatography (SEC).** All chromatograms are obtained using as mobile phase 25 mM HEPES pH = 7.5 with 0 mM $MgCl_2$ (A), 7 mM $MgCl_2$ (B) and 20 mM $MgCl_2$ (C). The main peak observed in A (~107 min) is consistent with the molecular weight of dimeric species, while the main peak in C (~70 min) with the tetraeicosameric structure. At intermediate salt concentration (B) both species exist in a ratio dependent on $Mg^{+2}$ concentration.

The three-dimensional structure of HumAf-Ft has been characterized by X-ray crystallography and Cryo-electron microscopy. HumAf-Ft was crystallized in the presence of $Mg^{2+}$in order to maintain the 24-mer assembly and the three-dimensional structure was solved by X-ray diffraction. Notably, the conditions required for the crystallization of HumAf-Ft was different respect to the wild type Af-Ft.

The structure of HumAf-Ft has been determined at a 2.87 Å resolution. It crystallized in the C2221 space group, as also observed for wild type Af-Ft. The overall folding corresponded to the wild type structure (PDB code 1S3Q) with a rmsd value of 0.4 Å and displayed four wide triangular pores on the surface (Fig. 4.8). B factor analysis shows a mean B factor of 66 Å2 with the exception of the loop region between the D and E helices, which displays higher B factors and a poor electron density on the side chains from 146 to 151 residues. Conversely, the BC loop is well organized and the analysis of the difference electron density (Fo–Fc) map clearly showed the presence of the mutated residues in the loop between the helices B and C as well as the M54C mutation, pointing towards the inner cavity.

The loop region, including the conserved terminal turns, spans from amino acid 68 to amino acid 86. The sequence alignment and the structural superposition between HumAf-Ft and the human H-homopolymer, as well as between HumAf-Ft and Af-Ft, are shown in Fig. 4.9 B and C. As observed also for HuHF structure, several non-covalent interactions occur at the dimeric interface between the two antiparallel BC loops, contributing to the stabilization of overall ferritin assembly. The main interactions consist of a hydrogen bond between Arg69(NH2) and Ser80 (O) at 2.8 Å distance and two salt bridges, namely Lys71 (NZ)–Glu77 (OE1) at 3.0 Å distance and Glu81 (OE2)–Arg69 (NH1) at 2.7 Å distance. An additional weak salt bridge is also established by Glu81 (OE2) and Arg69 (NH2) at 3.0 Å of distance. Other interactions as well are conserved between HuHF and HumAf-Ft and measured the same distances. Conversely, the salt bridge between Lys71 and Glu77

observed in HuHF is absent in HumAf-Ft, since these positions were mutated into a phenylalanine (Phe71) and a lysine (Lys77).

Moreover, Cryo-electron microscopy (Cryo-EM) measurements with HumAf-Ft in solution have been carried out in order to confirm the three-dimensional structure of the protein in a near-native environment. These measurements were done in collaboration with Prof. Amédée Des Georges (The City University of New York Advanced Science Research Center). Single ferritin particles were visualized at a nominal resolution of 33 Å demonstrating that their shape and dimensions correspond to that of wild type Af-Ft in its 24-mer assembly (Fig. 4.11 A). The canonical triangular pores of Af-Ft on the protein surface were clearly observable in a bi-dimensional view (Fig. 4.11 B) and better displayed in a three-dimensional reconstruction as shown in Fig. 4.11 C.

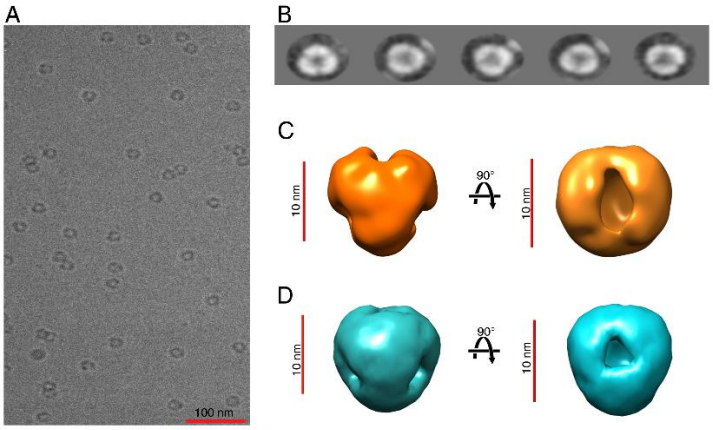


**Fig. 4.11 Electron microscopy characterization of humanized Archaeoglobus fulgidus ferritin.** (A) Sample micrograph of the HumAf-Ft data set. Scale bar: 100 nm. (B) Five representative 2D class averages obtained with RELION. (C) 3D reconstruction of HumAfFt obtained with RELION and visualized with UCSF Chimera.35 Map final resolution: 33.1 Å. Scale bars: 10 nm. Left: side view. Right: top view. (D) Archaeoglobus fulgidus ferritin crystal structure (from 16) filtered to 30 Å, shown for comparison. Scale bars: 10 nm. Left: side view. Right: top view.

## 4.2.3: TfR-1 binding and cellular uptake of HumAf-Ft

The capability of HumAf-Ft to gain access to eukaryotic cancer cells via TfR-1 receptor was assessed on HeLa cells by flow cytometry and confocal microscopy analysis. This part of the work has been carried out in collaboration with Dr. Valeria de Turris (Center for Life Nanoscience, Istituto Italiano di Tecnologia).

TfR-1 receptor is overexpressed in fast replicating and iron avid tumor cells but not in healthy cells. Previous works demonstrated that TfR-1 is capable of selectively internalizing human H-ferritin and responsible for its uptake into endosomes and lysosomes [Li L et al., (2010)].

To confirm that the modification on the external BC loop accounts for the internalization by HeLa cells, the uptake efficiency of HumAf-Ft was assessed in comparison to transferrin (the physiological ligand of TfR-1) and wild type Af-Ft. In this framework, time course experiments were carried out on cells treated with the same amount (30 μg $ml^{-1}$) of Af-Ft-FITC, HumAf-Ft-FITC and transferrin-FITC (TF-FITC) and analysed by flow cytometry. As a baseline for FITC fluorescence, control cells not incubated with FITC-ferritins were used. Moreover, to exclude any signal generated from outside particles sticking on the cell membrane due to unspecific binding or remains from the washing steps, trypan blue quenching was performed before using FACS. In Fig. 4.12, the FACS analysis is summarized, shown as the percentage of cells internalizing the nanoparticles at different times.

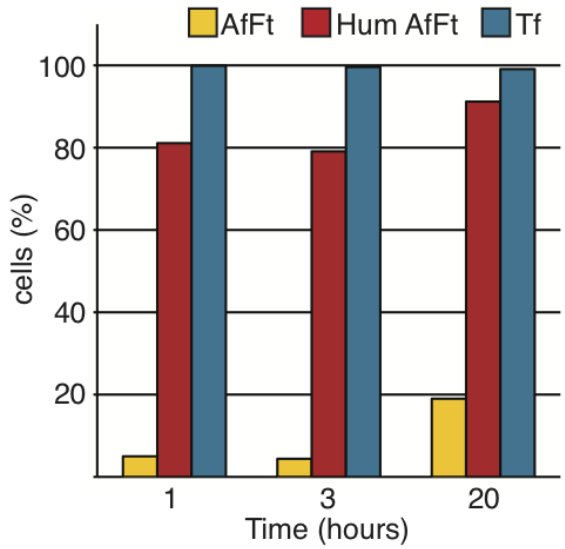


**Fig. 4.12: HumAf-Ft internalization.** Humanized AfFt is internalized with higher efficiency than the original ferritin. Ferritins taken up in HeLa cells have been quantified by flow cytometry. Cells have been treated with 30 μg $ml^{-1}$ of AfFt-FITC, HumAfFt-FITC and transferrin-FITC (Tf). The percentage of cells internalizing the nanoparticles at the time indicated is shown. For each sample 30 000 events gated on live cells have been acquired.

After one hour incubation, HumAf-Ft and transferrin displayed very close levels of cellular internalisation. Notably, HumAf-Ft was uptaken in a much higher extent compared to wild type Af-Ft (81% and 5% respectively). Similar results were obtained after longer incubation time (20 hours), as the uptake levels for the humanized samples are increased to more than 90% whereas for native Af-Ft they are still less than 20%. We hypothesize that the increment for Af-Ft sample is most likely due to unspecific pinocytosis mechanism.

Moreover, RNAi experiment against the transferrin receptor were performed and the cellular uptake of HumAf-Ft was investigated by FACS (Fig. 4.13). HumAf-Ft uptake was reduced of 50% after 48 hours of siRNA transfection, confirming the involvement of TfR1 in the internalization process.

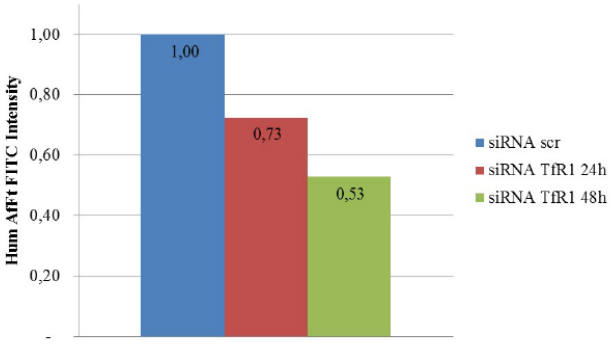


**Figure 4.13: TfR1 silencing causes a decreased Hum AfFt uptake.** HeLa cells transfected with control (scr) and specific anti-TfR1 (TfR1) siRNA for 24 and 48 hours, were incubated with Hum AfFt-FITC. After 3 hours cells were collected, washed and analyzed at the cytometer for the FITC fluorescent intensity. Compared to the FITC intensity in control cells (scr) we obtained an uptake reduction of almost 50% after 48 hours of RNAi.

The uptake of HumAf-Ft was visualized by confocal microscopy performing the internalization assay directly on an ibidi 8-well μ-slide. Cells were incubated for 20 hours before confocal microscopy and HeLa TagRFP cell lines were used in order to have a reference fluorescence signal confirming that we were imaging inside the cell. This cell line contains a TagRFP-FUS protein under the control of a doxycycline-inducible promoter that allows for a controlled expression of the protein and hence permits visualization of the nucleus in the red channel. Just before imaging, the cells were washed to eliminate the unbound FITC-nanoparticles and then acquired by confocal laser-scanning microscopy. Confocal representative images of the entire field

of view of live HeLa TagRFP cells alone (control) or incubated with HumAf-Ft-FITC or TF-FITC are shown in Fig. 4.14A. A detailed view of the boxed region in panel A is shown in Fig. 4.14B. Images confirmed the high extent of HumAf-Ft internalization and highlight a cellular distribution in the cytoplasm and in the perinuclear space comparable to that observed in the case of transferrin, thus suggesting a typical clathrin-coated endocytosis pathway, mediated by TfR1.

Taken together, these data revealed that the 12 amino acids' loop is necessary and sufficient for binding to the transferrin receptor. By mutating this region to reproduce the H-human analogous one, the archaeal ferritin scaffold has been endowed with the unprecedented ability to gain access to eukaryotic cancer cells with efficiency comparable to transferrin one. The engineered HumAf-Ft described here combines the versatility in assembly and cargo incorporation of Af-Ft by binding to TfR1 and by cellular uptake of HuHF.

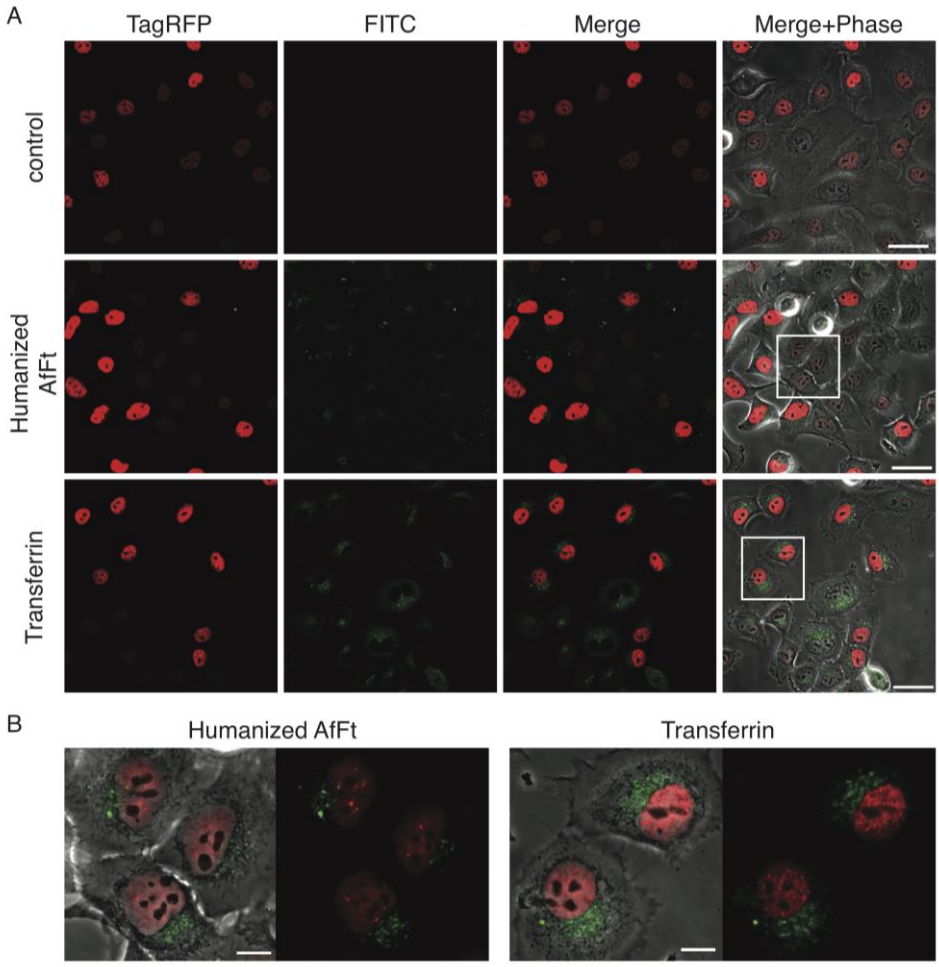


**Fig. 4.14 Ferritin internalization observed at the confocal microscope.** Cells were plated on an 8-well μ-slide (ibidi), induced with doxycycline to express TagRFP and then incubated with 30 μg ml−1 of humanized AfFt-FITC or transferrin-FITC for 20 h. After washing, cells were live-imaged using a confocal microscope. (A) Confocal images of live HeLa TagRFP cells are shown as single, merged channels and overlay images with the phase contrast. Scale bars: 40 μm. (B) Images are a magnified view of the region highlighted by the white inset in panel A; merged channels and the overlay with the phase contrast images are shown. Scale bars: 10 μm.

# 4.3 Engineered mammalian ferritin for lanthanide binding

## 4.3.1: Molecular design of HFt-LBT

HFt-LBT construct was designed in order to exploit the unique photophysical properties of lanthanide ions and to develop a smart bioluminescent platform for imaging applications.

Several chelating agents are currently employed to prevent the precipitation of trivalent lanthanide ions under physiological conditions and to sensitize their fluorescence by a Förster resonance energy transfer (FRET) mechanism. The fluorophore moiety of these compounds absorbs in the UV region and transfer the absorbed energy to the emitting level of the lanthanide, providing a relevant enhancement of luminescence signal [Hemmila I et al., (2005); Bunzli J, (2006); Rajapakse HE et al., (2009); Gudgin Dickson EF et al., (1995)]. However, these ligands must also fulfill several biochemical requirements to work properly and generally lack of targeting mechanism, thus reducing their versatility in bioimaging and diagnostic applications.

On the basis of known properties of $Ca^{2+}$ binding loop from Troponin-C EF hand motif, a novel co-expression tag named “lanthanide-binding tags” (LBT) has been recently developed for the incorporation of lanthanide ions into biomolecules. LBTs are short peptides (20 or fewer encoded aminoacids) capable of selective binding lanthanides over other common metal ions with low-nanomolar affinities. LBT sequence comprises six metal-binding residues for lanthanide coordination and a Trp residue in close proximity that provides strong FRET sensitization to the bound Terbium or Europium ions [Franz KJ et al., (2003); Nitz M et al., (2003); Martin LJ et al., (2007)]. The inner coordination sphere of Tb(III) bound to this sequence is also free from water

molecules [Nitz M et al., (2004)], a key feature for luminescence experiments, given the quenching effect of O-H vibration [Horrocks WD et al., (1979)]. These tags have been so far employed in fluorescence microscopy [Goda N et al., (2007); Shirakawa M et al., (2007)] and luminescence resonance energy transfer (LRET) studies [Sculimbrene BR et al., (2006)].

On this basis, our HFt-LBT construct has been developed by genetically fusing a LBT sequence at the C-terminal end of heavy chain of mouse ferritin (HFt). The tag has been designed to be located inside the inner cavity, such that lanthanide ions diffusing through the surface pores can eventually bind to the LBT sequence (see Fig. 4.12). The construct would thus act both as lanthanide FRET sensitizer and carrier targeted to TfR-1 receptors.

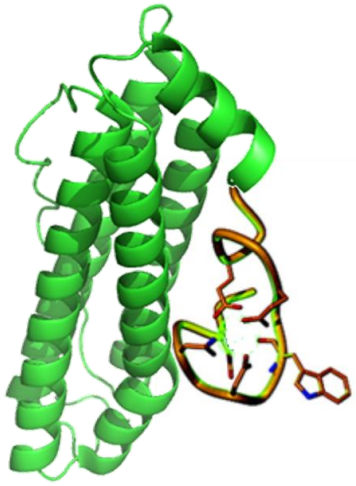

**Fig. 4.12: Schematic structure of HFt-LBT monomer.** The LBT sequence has been genetically fused at the C-terminal end of HFt protein (in green). The six Glutamate residues for Tb(III) coordination and the Tryptophan residue for FRET sensitization are placed in evidence.

## 4.3.2: Luminescent properties of HFt-LBT-Tb(III) complex

Fluorescence spectroscopy studies have been carried out in order to assess the luminescent properties of HFt-LBT-Tb(III) complex in comparison to the native HFt-Tb(III) complex. Native HFt have been used as control since mammalian apoferritin naturally bind Tb(III) within its iron binding sites [Stefanini S et al., (1983)]. In particular, it was demonstrated that mammalian apo-ferritins could bind more than one Tb(III) ion per subunit, corresponding respectively to ferroxidase site, threefold channel and nucleation centre [Treffry A et al., (1984); Bou-Abdallah F et al., (2003)]. Upon excitation between 280-295 nm, the Tb(III)-ferritin complex showed characteristic emission bands at 490 and 544 nm, due to the FRET sensitization effect provided by aromatic aminoacids [Bou-Abdallah F et al., (2003)]. However, the distance between Terbium ions and aromatic moieties in native ferritin isoforms made the FRET efficiency very poor and suboptimal for any type of fluorescence based measurement.

In Fig. 4.13 are reported the static emission spectra that were obtained from both Terbium saturated HFt-LBT and wild type mouse HFt upon excitation at 295 nm. The excitation of the tryptophan residue in the center of the LBT provided an excellent FRET sensitization to the bound Terbium atom, as demonstrated by the sustained narrow emission band at the 544 nm which is typical of Terbium excited state decay. The intensity of the Terbium emission peak at 544 nm for HFt-LBT was at least two orders of magnitude higher with respect to HFt, indicating that the presence of the LBT effectively sensitizes the Terbium signal. The Terbium emission band at 544 nm for the HFt-LBT Tb(III) complex was detectable up to 4 pM protein concentration. Moreover, extensive dialysis or size exclusion chromatography could not remove bound Tb(III), thus confirming that HFt-LBT construct exhibited high affinity Tb(III) binding.

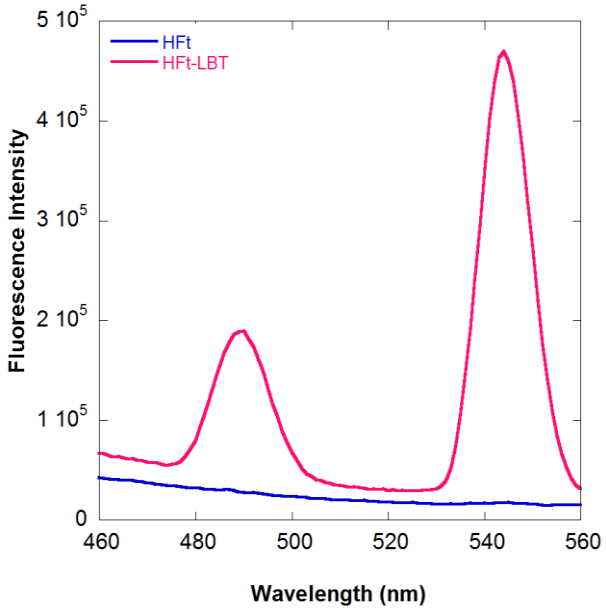


**Figure 4.13: Fluorescence spectra of HFt-LBT Tb(III) complex.** Fluorescence spectra of HFt-LBT-Tb(III) complex (red line) and wild type mouse HFt-Tb(III) complex (blue line) at the same protein concentration (1 μM). Spectra were recorded after 1 h incubation time with $TbCl_3$ in 0.1 M MES buffer pH 6.4.

Fluorescence titration analysis were carried out on HFt-LBT by adding free Tb(III) ions to the apo-protein. All measurements were conducted at pH 6.4 in MES buffer in order to avoid the precipitation of Terbium hydroxides, that are easily formed at neutral pH values. As shown in Fig. 4.14 (A) and (B), the titration endpoint was reached at 1.7 equivalent amount of Tb(III) per subunit. Analogous titrations carried out on wild type mouse HFt demonstrated a negligible fluorescence contribution provided by Terbium bound to the canonical metal binding sites (*i.e.* ferroxidase site, threefold channel and nucleation centre).

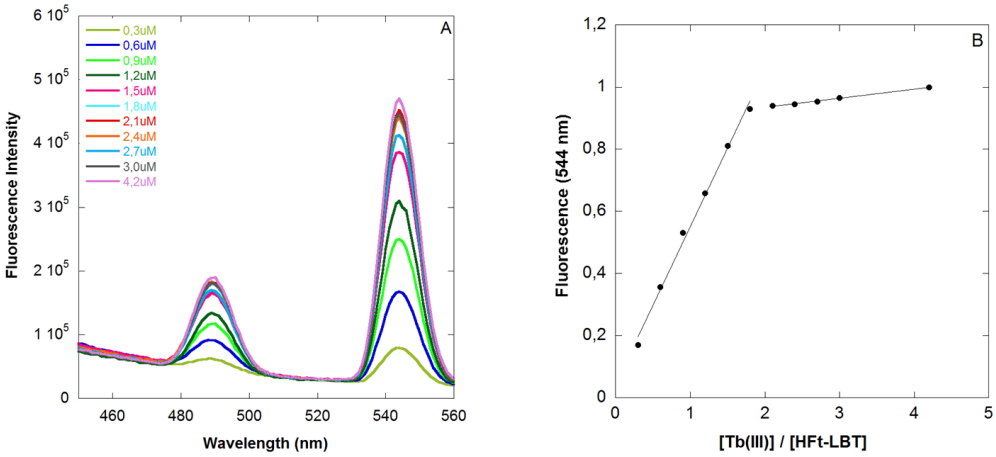


**Figure 4.14: Fluorescence titration of HFt-LBT with Tb(III).** A) Fluorescence titration of HFt-LBT (1 μM) with incremental concentration of Tb(III) (0–4 equivalents) in 0.1 M MES buffer pH 6.4. Emission spectra were recorded in 1 cm pathlength cuvette upon excitation at 295 nm. B) Fluorescence intensity of HFt-LBT-Tb(III) complex as a function of the Tb(III)/HFt-LBT ratio. Fluorescent intensity was recorded at 545 nm and normalized to the emission maximum.

Taken together, these data confirmed that tryptophan moiety within the LBT accounts for most of the improved fluorescence signal of Terbium and no spurious effect can be related to the native metal binding sites [Stefanini S et al., (1983); Treffry A et al., (1984); Bou-Abdallah F et al., (2003)]. The thermodynamics of the Terbium binding process was however complex due to presence of these additional binding sites. In particular, the maximum of observed fluorescence signal was reached at 1.7 Tb(III) ions per subunit, suggesting that the Trp residue within the tag may act as an antenna system not only for the Tb(III) ion bound within the LBT sequence but also for the other Tb(III) atoms present in the ferroxidase site or in the threefold channels.

## 4.3.3: Structural characterization of HFt-LBT

The three-dimensional structure of HFt-LBT was investigated both as crystals by X-ray crystallography and in solution by and cryo-EM microscopy. In particular, Cryo-EM measurements were carried out in collaboration with Prof. Amédée Des Georges (The City University of New York Advanced Science Research Center). The structures of apo HFt-LBT and HFt-LBT-Tb(III) complex have been determined by X-ray crystallography at a 2.85Å and 2.65 Å resolution, respectively. They both crystallized in I222 space group with 24 identical subunits in the asymmetric unit (ASU) with a solvent content of 64,7%. For cryo-EM measurements, instead, a plasma cleaned solution of HFt-LBT Tb(III) was applied to holey-gold grids and vitrified. The complete 7.1 Å resolution map of the protein structure in solution is shown in Fig.4.15. The overall results demonstrated that the presence of LBT at the C-terminal end does not affect the three-dimensional assembly of the HFt-LBT, which corresponds to the native H-chain mouse ferritin (PDB code 3WNW) with a*rmsd* value of 0.1 Å. Moreover, these results also confirmed that the genetically fused tags point to the interior cavity.

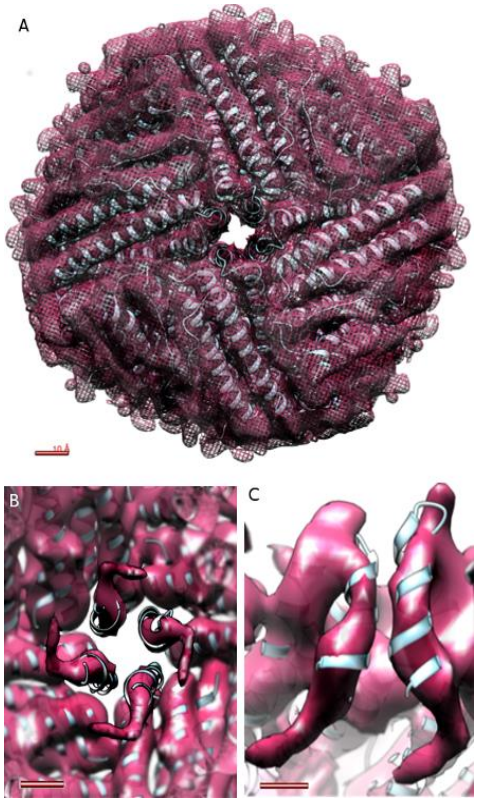


**Figure 4.15: 3D postprocess final maps of HFt-LBT Tb(III) from Cryo EM analysis.** Data were obtained with RELION and visualized with UCSF Chimera. Light blue: X-ray diffraction data of the crystal Terbium structure. Pink: experimental Cryo-EM electronic density map. Map resolution: 7.1 Angstroms. Scale bar=10 Angstroms. A: external view; B: internal view; C: focus on one internal C-terminal helix.

As expected, the high flexibility of the peptide arm connecting the LBT to the C-terminal sequence did not allow to obtain a complete resolution of the local structure [Barthelmes D et al., (2015)]. However, the analysis of selected 2D

classes obtained from cryo-EM measurements revealed significant densities within the internal cavity that can be attributed to the lanthanide binding tags. Such data provided the identification of low resolution but definite patterns relative to the first 6-7 aminoacids of the tag, though the possible multiple orientations of the loop region precluded the observation of the Tb(III) complex.

To further confirm the presence of Tb(III) ions within the HFt-LBT structure, crystals obtained from Tb(III)-treated and untreated protein were subjected to X-ray emission scans ranging from 4.0 to 8.0 KeV. Characteristic L and M X-ray line energies of Terbium have been clearly identified in the HFt-LBT-Tb(III) crystals. The crystals of Tb(III)-untreated HFt-LBT, instead, lacked these emission energies and displayed the characteristic energies lines of residual iron atoms.

In HFt-LBT-Tb(III) structure, 24 Terbium ions have been positioned and successfully refined with a 75% occupancy in each ferroxidase site of the protein scaffold and 8 Terbium ions have been positioned with 100 % occupancy in each three-fold axes. In the ferroxidase center, each Terbium ion is located in a trigonal planar coordination to OE1-Gln141 and to OE1 and OE2-Glu62, and to OE2-Glu27, in a range 2.6-3.2 Å distance (Figure 4.16 A). In the 3-fold center, the Terbium ion is tetrahedrally coordinated to OE1-Glu134 of the three subunits, (at 2.2-2.4 Å distance) (Figure 4.16 B). However, the high flexibility of C-terminal end did not allow to visualize by X-ray diffraction the Tb(III) atoms bound to the LBT sequence.

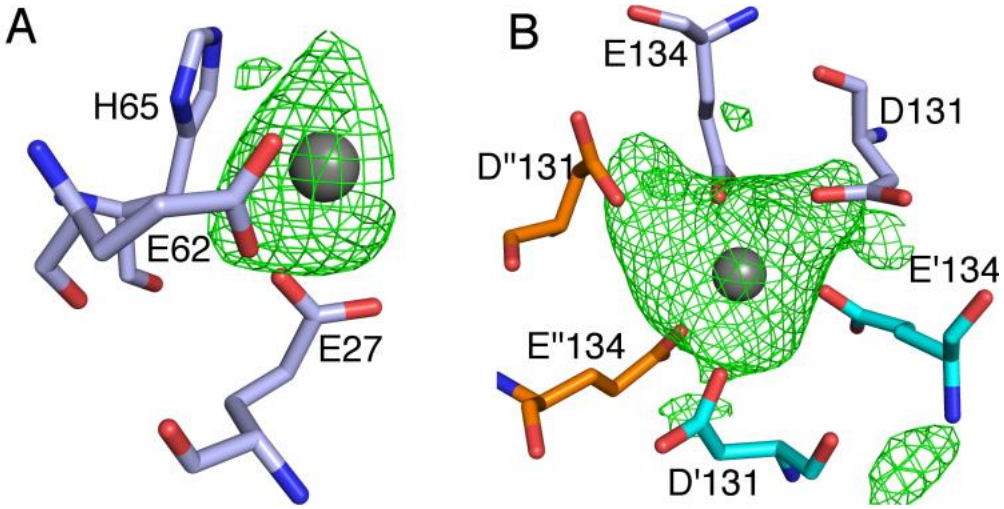


**Figure 4.16: Terbium binding sites from X-ray crystallography.** The omit map contoured at 3 σ is shown as a green mesh A) In the ferroxidase center: a Tb(III), is shown as a grey sphere and B) in the 3-fold axes: the residues Glu131 and Glu134 of three different monomers are depicted as sticks in light blue, cyan and orange, respectively.

In summary, HFt-LBT construct is capable of high affinity binding of 24 Tb(III) atoms at each tag and 18, out of 24 available (occupancy in X-ray structure corresponded to 75%), at the ferroxidase binding site. In addition, 8 fully occupied sites are observed at the entrance of the threefold channels for a total of 50 Terbium atoms within the whole 24-mer. Moreover, these data further confirmed our hypothesis that the LBT segment keeps a certain degree of mobility even inside the ferritin cavity. Such flexibility allows to the Trp residue of the tag to come in close proximity and to provide FRET sensitization even to the Terbium atoms bound to the native metal binding sites.

## 4.3.4: HFt-LBT as fluorescent bioimaging probe

The ability of HFt-LBT construct to be recognized and uptaken by TfR-1 receptor was assessed in selected human tumor cell lines by flow cytometry and confocal microscopy. The wild type mouse HFt was used as control. This part of the work has been carried out in close collaboration with Prof. Magdalena Król (Warsaw University of Life Sciences) and Tomasz Rygiel (Medical University of Warsaw).

Preliminary data of confocal microscopy revealed that the direct excitation of Trp residue within LBT sequence at 290-375 nm yielded very poor imaging results, due to the very high fluorescence background within the Terbium emission interval. Following measurements have been then carried out on HFt-LBT-Tb(III) and wild type mouse HFt stained with FITC.

Cancer cell lines were treated with the same amount (0.5 mg/ml) of FITC-labeled HFt-LBT-Tb(III) or HFt, using control cells untreated with FITC-ferritins as baseline for FITC fluorescence. Moreover, in order to exclude any signal generated from outside particles sticking on the cell membrane due to unspecific binding or remaining from the washing steps, Trypan blue quenching was performed before FACS acquisition.

FACS analysis revealed that HFt-LBT-Tb(III) nanoparticles are efficiently taken up by all cells of each cell line. Moreover, confocal microscopy allowed to visualize HFt-LBT-Tb(III) nanocages within cytoplasm, as shown in Figure 4.17. These results confirmed the high extent of both HFt-LBT-Tb(III) and wild type mouse HFt internalization and highlight similar cellular distribution in the cytoplasm and in the perinuclear space. In particular, DU145 (from a central nervous system metastasis, of primary prostate adenocarcinoma origin), MDA-MB-231 (from invasive ductal carcinoma, Hepatoma cell line and SK-OV-3 (highly resistant ovarian cancer cell line) were demonstrated for the first time to display a high uptake of both wild type mouse HFt and HFt-

LBT-Tb(III). These cancer cell lines overexpress TfR-1 molecule and are subject of cancer therapy studies focused on this receptor.

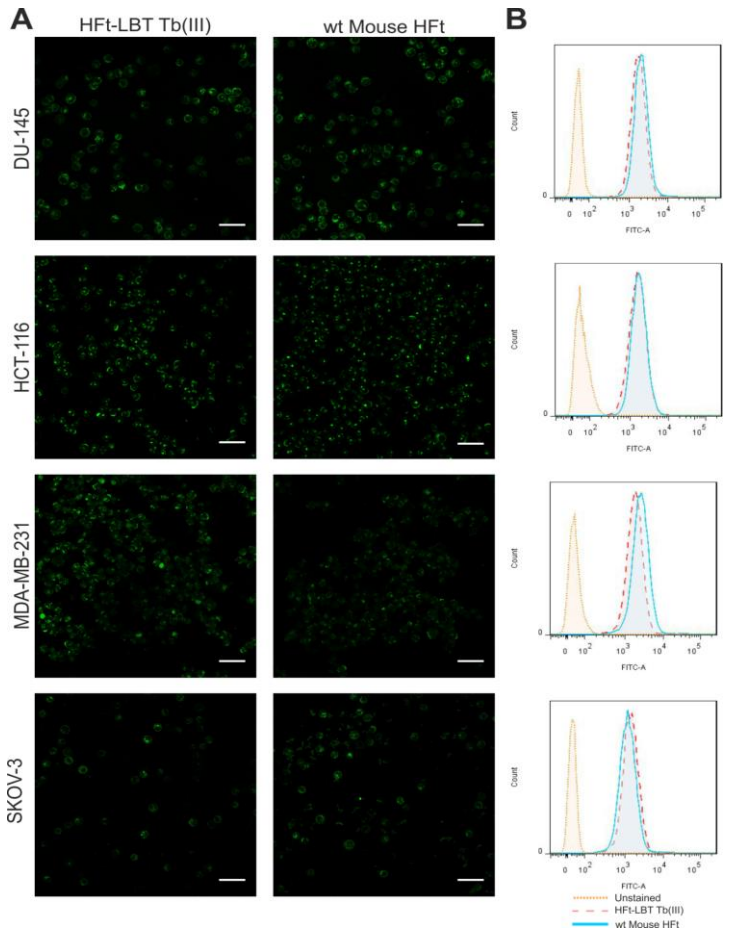


**Figure 4.17: Confocal microscopy images and flow cytometry analysis of HFt-LBT Tb(III) uptake by selected tumor cell lines.** DU-145, HCT-116, MDA-MB-231 and SKOV-3 cancer cells were incubated with either HFt-LBT Tb(III) or wild type mouse HFt (0.5 mg/ml) for 60 min. A) Images acquired by confocal microscopy showing side by side comparison of cellular distribution of HFt-LBT Tb(III) and HFt conjugated with FITC. Scale bar = 50 μm. B) Flow cytometry analysis of HFt-LBT Tb(III) and HFt cellular uptake.

In conclusion, these data highlighted that mammalian ferritin retained their overall assembly and the TfR-1 recognition properties even upon addition of short peptide sequences at the C-terminal end. Moreover, the insertion of appropriate metal binding tags inside the cavity provided specific additional metal sites in topologically selected positions. Such approach represents a valuable alternative to the quasi random metal clusters insertion into the ferritin cavity that has been commonly used by free diffusion of metal ions through the open pores on the surface of the macromolecule or by disassembly-reassembly of the 24-mer structure ("encapsulation" procedure) [Falvo E et al., (2016)].

# 5 Conclusions

The aim of this work was the development and the characterization of novel engineered ferritin constructs to widespread the biotechnological applications of these proteins.

In the last few years the human ferritin has emerged as a smart and highly biocompatible nanocarrier, due to its ability to encapsulate therapeutic compounds or diagnostic probes within the inner cavity and to target TfR-1 overexpressing tumor cells. However, the currently employed encapsulation procedure is critically affected by the pH-jump required for the cage disassembly. This step represents a major limit for the drug stability and usually leads to the suboptimal cargo incorporation. Moreover, the strict charge selectivity of mammalian cage towards molecular diffusants further reduces the versatility of these tools in biotechnological applications.

On this basis, part of this work has been focused on investigating some unprecedented features displayed by archaeal ferritins in comparison to the mammalian isoforms.

The assembly study carried out on *Archaeoglobus fulgidus* mutants pointed out that all the developed constructs retained the association/dissociation properties typical of wild type form, which depends on ionic strength instead of pH. This behaviour was kept even when relevant modifications to the primary sequence were introduced, such as for HumAf-Ft construct. In all cases, the structural transition between dimeric species and stable 24-mer was achieved at neutral pH conditions and within a very narrow range of salt concentration, when divalent cations were used as polymerizing agents (*i.e.* 0-20 mM for $Mg^{+2}$). Further structural investigations will be addressed to identify the specific residues that account for this property. On the side of material science, the availability of a cations dependent self-assembling cage provides the basis of a unique "molecular carpentry" tools.

In addition, the investigation of the molecular permeability of the protein shell carried out on *Archaeoglobus fulgidus* and *Pyrococcus furiosus* mutants demonstrated that the archaeal 3-fold channels have significantly divergent

properties respect to the mammalian ones. Although molecular diffusion into archaeal ferritin is a complex phenomenon, even closed and apparently impermeable ferritins did allow the entry of 8–10 Å long organic molecules with no necessity of 24-mer disassembly. Unlike mammalian protein shell, the protein matrix in archaeal ferritins did not provide a significant barrier against bulky, negatively charged ligands such as DTNB. The comparison of lining aminoacids between archaeal and human 3-fold channels also highlighted the residues responsible for the divergent selectivity towards molecular diffusants.

Taken together, these findings are relevant in view of the multiple biotechnological applications that envisage ligand encapsulation within the internal cavity. Moreover, they represent a valuable background for the development on novel eukaryotic ferritin constructs endowed with improved assembly and permeability features.

In the same framework, the "Humanized" Archaeoglobus ferritin (HumAf-Ft) was developed in order to characterize the interaction between the ferritin scaffold and TfR-1 receptor and the resulting uptake by eukaryotic cells. Our results demonstrated that our chimeric construct actually combines the versatility in assembly and cargo incorporation properties of Af-Ft with the capability of HuHF to bind toTfR-1 and undergo cellular internalization. Moreover, we demonstrated that the 12 amino acids' sequence of human ferritin BC loop is necessary and sufficient for binding to the transferrin receptor. However, *in vivo* applications will have to wait for the evaluation of possible immunological responses against non-human epitopes present on the protein surface. In fact, though the mutated loops appear to account for most of the solvent exposed surface, N-terminal and pore lining regions might still offer structural motifs for non-self-recognition by the immune system.

The second part of this work has been focused on engineering the eukaryotic ferritin scaffold to obtain a diagnostic probe for bioimaging applications. The HFt-LBT construct was designed to selectively bind trivalent lanthanide ions within the inner cavity. The characterization of this chimeric protein demonstrated that appropriate tags can be placed inside the cavity without

affecting the overall assembly and provide specific additional metal binding sites in topologically selected positions. This approach represents a valuable alternative to the quasi random encapsulation of metal payload that is achieved with the current loading strategy. The guided allocation of metal sites inside the cavity also foresees the rationale positioning of more efficient antenna systems respect to the lanthanide sites, in order to assess the best geometry for efficient FRET sensitization. Further engineering of such metal binding sites would foster most advanced applications, such as the construction of up-converting nanoparticles or ultrabright fluorescent organic polymer for single molecule detection. Moreover, HFt-LBT combines the ability of incorporating lanthanide ions with the ability of targeting TfR-1 overexpressing tumor cells. Hence, this construct can be exploited in biomedical applications for the delivery of lanthanide radioisotopes currently investigated as tumor detection probes, therapeutic radionuclides or MRI contrast agents.

# 6 Glossary

# List of abbreviations

| | |
|---|---|
| **ADC** | Antibody-drug conjugates |
| **Bfr** | Bacterioferritin |
| **cryo-EM** | Cryo electron microscopy |
| **Dps** | DNA-binding protein from starved cells |
| **HuHF** | human H-chain ferritin |
| **HuLF** | human L-chain ferritin |
| **FtnA** | *E. coli* ferritin |
| **Pf-Ft** | *Pyrococcus furiosus* ferritin |
| **Af-Ft** | *Archaeoglobus fulgidus* ferritin |
| **Af-Ft-AA** | *Archaeoglobus fulgidus* ferritin “closed” double mutant |
| **MRI** | Magnetic resonance imaging |
| **ROS** | Reactive oxygen species |
| **Tf** | Transferrin |
| **TfR-1** | Human transferrin receptor 1 |

# 7 Bibliography

Adams PD, Afonine PV, Bunkoczi G, Chen VB, Davis IW, Echols N, Headd JJ, Hung LW, Kapral GJ, Grosse-Kunstleve RW, McCoy AJ, Moriarty NW, Oeffner R, Read RJ, Richardson DC, Richardson JS, Terwilliger TC, Zwart PH. PHENIX: a comprehensive Python-based system for macromolecular structure solution. *Acta Cryst. D.* 2010; 66**:**213-221

Allen JE, McLendon GL. Tryptophan and tyrosine to terbium fluorescence resonance energy transfer as a method to "map" aromatic residues and monitor docking. *Biochem Biophys Res Commun.* 2006; 349(4):1264-8.

Andrews SC. Iron storage in bacteria. *Adv Microb Physiol.* 1998; 40:281-351.

Andrews SC, Arosio P, Bottke W, Briat JF, von Darl M, Harrison PM, Laulhère JP, Levi S, Lobreaux S, Yewdall SJ. Structure, function, and evolution of ferritins. *J Inorg Biochem.* 1992; 47(3-4):161-74.

Andrews SC. The Ferritin-like superfamily: evolution of the biological iron storeman from a rubrerythrin-like ancestor. *Biochim. Biophys. Acta* 2010; 1800:691–705.

Arosio P, Elia L, Poli M. Ferritin, cellular iron storage and regulation. *IUBMB Life.* 2017; 69(6):414-422.

Barthelmes D, Granz M, Barthelmes K, Allen KN, Imperiali B, Prisner T and Schwalbe H. Encoded loop-lathanide-binding tags for log-range distance measurements in proteins by NMR and EPR spectroscopy. *J. Biomol. NMR* 2015; 63**:**275-282.

Beheraa RK, Theil EC. Moving $Fe^{2+}$ from ferritin ion channels to catalytic OH centers depends on conserved protein cage carboxylates. *Proc. Natl. Acad. Sci. U. S. A.* 2014; 111:7925–7930.

Bellini M, Mazzucchelli S, Galbiati E, Sommaruga S, Fiandra L, Truffi M, Rizzuto MA, Colombo M, Tortora P, Corsi F, Prosperi D. Protein nanocages for self-triggered nuclear delivery of DNA-targeted chemotherapeutics in Cancer Cells. *J Control Release.* 2014; 196:184-96.

Bernacchioni C, Ghini V, Pozzi C, Di Pisa F, Theil EC, Turano P. Loop electrostatics modulates the intersubunit interactions in ferritin. *ACS Chem Biol.* 2014; 9(11):2517-25.

Berne BJ, Pecora R. Dynamic Light Scattering. Wiley, New York, 1976.

Bou-Abdallah F, Woodhall MR, Velásquez-Campoy A, Andrews SC, Chasteen ND, Thermodynamic analysis of ferrous ion binding to Escherichia coli ferritin EcFtnA. *Biochemistry* 2005; 44:13837–13846.

Bou-Abdallah F, Zhao G, Biasiotto G, Poli M, Arosio P, Chasteen ND. Facilitated diffusion of iron(II) and dioxygen substrates into human H-chain ferritin. A fluorescence and absorbance study employing the ferroxidase center substitution Y34W. *J Am Chem Soc.* 2008; 130(52):17801-11.

Bou-Abdallah F. The iron redox and hydrolysis chemistry of the ferritins. *Biochim Biophys Acta.* 2010; 1800(8):719-31.

Bou-Abdallah F, Yang H, Awomolo A, Cooper B, Woodhall MR, Andrews SC, Chasteen ND. Functionality of the three-site ferroxidase center of Escherichia coli bacterial ferritin (EcFtnA). *Biochemistry*. 2014; 53(3):483-95.

Bou-Abdallah F, Arosio P, Levi S, Janus-Chandler C and Chasteen ND. Defining metal ion inhibitor interactions with recombinant human H- and L-chain ferritins and site-directed variants: an isothermal titration calorimetry study. *J. Biol. Inorg. Chem.* 2003; 8(4):489-497.

Bradley JM, Moore GR, Le Brun NE. Mechanisms of iron mineralization in ferritins: one size does not fit all. *J Biol Inorg Chem.* 2014; 19(6):775-85.

Bradley JM, Moore GR, Le Brun NE. Diversity of $Fe^{2+}$ entry and oxidation in ferritins. *Curr Opin Chem Biol.* 2017; 37:122-128.

Bunzli J. Benefiting from the unique properties of lanthanide ions. *Acc. Chem. Res.* 2006; 39:53-61.

Bunzli JC Luminescent lanthanide probes as diagnostic and therapeutic tools. *Met. Ions. Biol. Syst.* 2004; 42:39-75

Carmona F, Poli M, Bertuzzi M, Gianoncelli A, Gangemi F, Arosio P. Study of ferritin self-assembly and heteropolymer formation by the use of Fluorescence Resonance Energy Transfer (FRET) technology. *Biochim Biophys Acta.* 2017; 1861(3):522-532.

Chasteen ND, Harrison PM. Mineralization in ferritin: an efficient means of iron storage. *J Struct Biol.* 1999; 126(3):182-94.

Chen H, Zhang S, Xu C, Zhao G. Engineering protein interfaces yields ferritin disassembly and reassembly under benign experimental conditions. *Chem Commun (Camb).* 2016; 52(46):7402-5.

Chiancone E, Ceci P. The multifaceted capacity of Dps proteins to combat bacterial stress conditions: detoxification of iron and hydrogen peroxide and DNA binding. *Biochim. Biophys. Acta* 2010; 1800(8):798–805.

Chen H, Zhang S, Xu C, Zhao G. Engineering protein interfaces yields ferritin disassembly and reassembly under benign experimental conditions. *Chem Commun (Camb).* 2016; 52(46):7402-5.

Chen VB, Arendall WB, Headd JJ, Keedy DA, Immormino RM, Kapral GJ, Murray LW, Richardson JS, Richardson DC. MolProbity: allatom structure validation for macromolecular crystallography. *Acta Crystallogr., Sect. D: Biol. Crystallogr*. 2010; 66:12–21.

Chen S, McMullan G, Faruqi AR, Murshudov GN, Short JM, Scheres SH, Henderson R. High-resolution noise substitution to measure overfitting and validate resolution in 3D structure determination by single particle electron cryomicroscopy. *Ultramicroscopy*, 2013; 135: 24–35.

Clerté S, Dautant A, Langlois d'Estaintot B, Gallois B, Mizunoe Y, Wai SN, Précigoux G Expression, purification, crystallization and preliminary X-ray diffraction results from Campylobacter jejuni ferritin. *Acta Crystallogr D Biol Crystallogr*. 1999; 55:299-301.

Crichton RR, Declercq JP. X-ray structures of ferritins and related proteins. *Biochim Biophys Acta*. 2010; 1800(8):706-18.

Crichton RR. Iron Metabolism: From Molecular Mechanisms to Clinical Consequences. *John Wiley & Sons, Hoboken*; 2016.

Danev R, Buijsse B, Khoshouei M, Plitzko JM, Baumeister W. Volta potential phase plate for in-focus phase contrast transmission electron microscopy. *Proc.Natl. Acad. Sci. U. S. A.*, 2014; 111:15635–15640.

Desideri A, Stefanini S, Polizio F, Petruzzelli R, Chiancone E. Iron entry route in horse spleen apoferritin. Involvement of the three-fold channels as probed by selective reaction of cysteine-126 with the spin label 4-maleimido-tempo. *FEBS Lett.* 1991; 287:10–14.

Douglas T, Ripoll DR. Calculated electrostatic gradients in recombinant human H-chain ferritin. *Protein Sci.* 1998; 7(5):1083-91.

Drysdale, J. Ferritin Phenotypes: Structure and Metabolism. *Novartis Foundation Symposia*. 2008; 41-78.

Dubochet J, Adrian M, Chang JJ, Homo JC, Lepault J, McDowall AW, Schultz P. Cryo-electron microscopy of vitrified specimens. *Q. Rev. Biophys.* 1988; 21: 129–228.

Ebrahimi KH, Hagedoorn PL, Jongejan JA, Hagen WR. Catalysis of iron core formation in *Pyrococcus furiosus* ferritin. *J Biol Inorg Chem.* 2009; 14(8):1265-74.

Ebrahimi KH, Hagedoorn PL, Hagen WR. A conserved tyrosine in ferritin is a molecular capacitor. *Chembiochem*. 2013; 14(9):1123-33.

Elzoghby AO, Samy WM, Elgindy NA. Protein-based nanocarriers as promising drug and gene delivery systems. *J Control Release* 2012; 161(1):38-49.

Emsley P, Cowtan K. Coot: model-building tools for molecular graphics. *Acta Crystallogr., Sect. D: Biol.Crystallogr.*, 2004; 60:2126–2132.

Falvo E, Tremante E, Fraioli R, Leonetti C, Zamparelli C, Boffi A, Morea V, Ceci P, Giacomini P. Antibody-drug conjugates: targeting melanoma with cisplatin encapsulated in protein-cage nanoparticles based on human ferritin. *Nanoscale* 2013; 5(24):12278-85.

Falvo E, Tremante E, Arcovito A, Papi M, Elad N, Boffi A, Morea V, Conti G, Toffoli G, Fracasso G, Giacomini P and Ceci P. Improved Doxorubicin Encapsulation and Pharmacokinetics of Ferritin-Fusion Protein Nanocarriers Bearing Proline, Serine, and Alanine Elements. *Biomacromolecules* 2016; 17(2):514-522.

Fan K, Cao C, Pan Y, Lu D, Yang D, Feng J, Song L, Liang M and. Yan X. Magnetoferritin nanoparticles for targeting and visualizing tumour tissues. *Nat. Nanotechnol*., 2012; 7:459–464.

Franz KJ, Nitz M and Imperiali B. Lanthanide-binding tags as versatile protein coexpression probes. *Chembiochem.* 2003; 4(4) 265-271.

Geninatti Crich S, Bussolati B, Tei L, Grange C, Esposito G, Lanzardo S, Camussi G, Aime S. Magnetic resonance visualization of tumor angiogenesis by targeting neural cell adhesion molecules with the highly sensitive gadolinium-loaded apoferritin probe. *Cancer Res*. 2006; 66(18):9196-201.

Gerl M, Jaenicke R. Mechanism of the self-assembly of apoferritin from horse spleen. Cross-linking and spectroscopic analysis. *Eur Biophys J.* 1987; 15(2):103-9.

Gerl M, Jaenicke R, Smith JM, Harrison PM. Self-assembly of apoferritin from horse spleen after reversible chemical modification with 2,3-dimethylmaleic anhydride. *Biochemistry*. 1988; 27(11):4089-96.

Goda N, Tenno T, InomataK, Iwaya N and Sasaki Y. LBT/PTD dual tagged vector for purification, cellular protein delivery and visualization in living cells *Biochim. Biophys. Acta* 2007; 1773(2):141-614

Gudgin Dickson EF, Pollak A, Diamandis EP. Time-resolved detection of lanthanide luminescence for ultrasensitive bioanalytical assays. *Photochem. Photobiol. B* 1995; 27(1):3-19.

Ha Y, Shi D, Small GW, Theil EC, Allewell NM. Crystal structure of bullfrog M ferritin at 2.8 A resolution: analysis of subunit interactions and the binuclear metal center. *J Biol Inorg Chem.* 1999; 4(3):243-56.

Haikarainen T, Papageorgiou AC. Dps-like proteins: structural and functional insights into a versatile protein family. *Cell Mol Life Sci.* 2010; 67(3):341-51.

Hainfeld JF. Uranium-loaded apoferritin with antibodies attached: molecular design for uranium neutron-capture therapy. *Proc Natl Acad Sci U S A.* 1992; 89(22):11064-8.

Handl HL, Gillies R. Lanthanide-based luminescent assays for ligand-receptor interactions. *J. Life Sci.* 2005; (77):361-371

Harrison P. The structure and function of ferritin. *Biochemical Education*. 1986; 14(4):154-162.

Harrison PM, Hempstead PD, Artymiuk PJ, Andrews SC. Structure-function relationships in the ferritins. *Met Ions Biol Syst.* 1998; 35:435-77.

Harrison PM, Treffry A, Lilley TH. Ferritin as an iron-storage protein: mechanisms of iron uptake. *J. Inorg. Biochem.* 1986; 27:287–293.

Heger Z, Skalickova S, Zitka O, Adam V and Kizek R. Apoferritin applications in nanomedicine. *Nanomedicine*. 2014; 9:2233–2245.

Hemmila I and Laitala VJ. Progress in lanthanides as luminescent probes. *Fluoresc.* 2005; 15:529-542.

Hempstead PD, Yewdall SJ, Fernie AR, Lawson DM, Artymiuk PJ, Rice DW, Ford GC, Harrison PM. Comparison of the three-dimensional structures of recombinant human H and horse L ferritins at high resolution. *J Mol Biol.* 1997; 268(2):424-48.

He D, Marles-Wright J. Ferritin family proteins and their use in bionanotechnology. *N Biotechnol.* 2015; 32(6):651-7.

He L, Cheng Y, Kong L, Azadnia P, Giang E, Kim J, Wood MR, Wilson IA, Law M, Zhu J. Approaching rational epitope vaccine design for hepatitis C virus with meta-server and multivalent scaffolding. *Sci Rep.* 2015; 5:12501.

Hemmila I, Laitala VJ. Progress in lanthanides as luminescent probes. *Fluoresc*. 2005; 15:529-542

Hooker JM, Datta A, Botta M, Raymond KN, Francis MB. Magnetic resonance contrast agents from viral capsid shells: a comparison of exterior and interior cargo strategies. *Nano Lett.* 2007; 7(8):2207-10.

Horrocks WD Jr and Sudnick DR. Lanthanide ion probes of structure in biology. Laser-induced luminescence decay constants provide a direct measure of the number of metal-coordinated water molecules. *J. Am. Chem. Soc.* 1979; 101:334-340.

Huard DJ, Kane KM, Tezcan FA. Re-engineering protein interfaces yields copper-inducible ferritin cage assembly. *Nat Chem Biol.* 2013; 9(3):169-76.

Hudson AJ, Andrews SC, Hawkins C, Williams JM, Izuhara M, Meldrum FC, S Mann, Harrison PM, Guest JR. Overproduction, purification and characterization of the Escherichia coli ferritin. *Eur. J. Biochem.* 1993; 218:985–995.

Jacobs JF, Hasan MN, Paik KH, Hagen WR, van Loosdrecht MC. Development of a bionanotechnological phosphate removal system with thermostable ferritin. *Biotechnol Bioeng.* 2010; 105(5):918-23.

Ji XT, Huang L, Huang HQ. Construction of nanometer cisplatin core-ferritin (NCC-F) and proteomic analysis of gastric cancer cell apoptosis induced with cisplatin released from the NCC-F. *J Proteomics.* 2012; 75(11):3145-57.

Jin R, Lin B, Li D, Ai H. Superparamagnetic iron oxide nanoparticles for MR imaging and therapy: design considerations and clinical applications. *Curr Opin Pharmacol.* 2014; 18:18-27.

Johnson E, Cascio D, Sawaya MR, Gingery M, Schröder I. Crystal structures of a tetrahedral open pore ferritin from the hyperthermophilic archaeon Archaeoglobus fulgidus. *Structure*. 2005; 13(4):637-48.

Kabsch W. Integration, scaling, space-group assignment and post-refinement. *Acta Crystallogr., Sect. D: Biol.Crystallogr.*, 2010; 66:133–144.

Kálmán FK, Geninatti-Crich S, Aime S. Reduction/dissolution of a beta-MnOOH nanophase in the ferritin cavity to yield a highly sensitive, biologically compatible magnetic resonance imaging agent. *Angew Chem Int Ed Engl.* 2010; 49(3):612-5.

Kanekiyo M, Wei CJ, Yassine HM, McTamney PM, Boyington JC, Whittle JR, Rao SS, Kong WP, Wang L, Nabel GJ. Self-assembling influenza nanoparticle vaccines elicit broadly neutralizing H1N1 antibodies. *Nature*. 2013; 499(7456):102-6.

Kanekiyo M, Bu W, Joyce MG, Meng G, Whittle JR, Baxa U, Yamamoto T, Narpala S, Todd JP, Rao SS, McDermott AB, Koup RA, Rossmann MG, Mascola JR, Graham BS, Cohen JI, Nabel GJ. Rational Design of an Epstein-Barr Virus Vaccine Targeting the Receptor-Binding Site. *Cell.* 2015; 162(5):1090-100.

Kilic MA, Ozlu E, Calis S. A novel protein-based anticancer drug encapsulating nanosphere: apoferritin-doxorubicin complex. *J Biomed Nanotechnol.* 2012; 8(3):508-14.

Kim M, Rho Y, Jin KS, Ahn B, Jung S, Kim H, Ree M. pH-dependent structures of ferritin and apoferritin in solution: disassembly and reassembly. *Biomacromolecules*. 2011; 12(5):1629-40.

Kwak Y, Schwartz JK, Haldar S, Behera RK, Tosha T, Theil EC, Solomon EI. Spectroscopic studies of single and double variants of M ferritin: lack of conversion of a biferrous substrate site into a cofactor site for $O_2$ activation. *Biochemistry*. 2014; 53(3):473-82.

Laskowski RA, MacArthur MW, Moss DS, Thornton JM. PROCHECK - a program to check the stereochemical quality of protein structures. *J. Appl.Crystallogr*. 1993; 26:283–29125.

Lee EJ, Lee SJ, Kang YS, Ryu JH, Kwon KC, Jo E, Yhee JY, Kwon IC, Kim K, Lee J. Engineered proteinticles for targeted delivery of siRNA to cancer cells. *Adv. Funct. Mater*. 2015; 25:1279–1286.

Levi S, Luzzago A, Cesareni G, Cozzi A, Franceschinelli F, Albertini A and Arosio P. Mechanism of ferritin iron uptake: activity of the H-chain and deletion mapping of the ferro-oxidase site. A study of iron uptakeand ferroxidase activity of human liver, recombinant H-chain ferritins, and of two H-chain deletion mutants. *J. Biol. Chem.*, 1988; 263: 18086–18092.

Levi S, Rovida E. Neuroferritinopathy: From ferritin structure modification to pathogenetic mechanism. *Neurobiol Dis.* 2015; 81:134-43.

Li L, Fang CJ, Ryan JC, Niemi EC, Lebrón JA, Björkman PJ, Arase H, Torti FM, Torti SV, Nakamura MC, Seaman WE. Binding and uptake of H-ferritin are mediated by human transferrin receptor-1. *Proc Natl Acad Sci U S A.* 2010; 107(8):3505-10.

Liang M, Fan K, Zhou M, Duan D, Zheng J, Yang D, Feng J, Yan X. H-ferritin-nanocaged doxorubicin nanoparticles specifically target and kill

tumors with a single-dose injection. *Proc Natl Acad Sci U S A*. 2014; 111(41):14900-5.

Lin X, Xie J, Niu G, Zhang F, Gao H, Yang M, Quan Q, Aronova MA, Zhang G, Lee S, Leapman R, Chen X. Chimeric ferritin nanocages for multiple function loading and multimodal imaging. *Nano Lett.* 2011; 11(2):814-9.

Le Brun NE, Crow A, Murphy MEP, Mauk AG, Moore GR: Iron core mineralisation in prokaryotic ferritins. *Bioch Biophys Acta* 2010; 1800:732-744.

Li X, Qiu L, Zhu P, Tao X, Imanaka T, Zhao J, Huang Y, Tu Y, Cao X. Epidermal growth factor-ferritin H-chain protein nanoparticles for tumor active targeting. *Small*. 2012; 8(16):2505-14.

Li L, Fang CJ, Ryan JC, Niemi EC, Lebrón JA, Björkman PJ, Arase H, Torti FM, Torti SV, Nakamura MC and Seaman WE. Binding and uptake of H-ferritin are mediated by human transferrin receptor-1. *Proc. Natl. Acad. Sci. U. S. A.*, 2010; 107: 3505–3510.

Liang M, Fan K, Zhou M, Duan D, Zheng J, Yang D, Feng J and. Yan X. H-ferritin-nanocaged doxorubicin nanoparticles specifically target and kill tumors with a singledose injection, *Proc. Natl. Acad. Sci. U. S. A.*, 2014; 111:14900–14905.

Lin X, Xie J, Niu G, Zhang F, Gao H, Yang M, Quan Q, Aronova MA, Zhang G, Lee S, Leapman R, Chen X. Chimeric ferritin nanocages for multiple function loading and multimodal imaging. *Nano Lett*. 2011; 11(2):814-9.

López-Sagaseta J, Malito E, Rappuoli R, Bottomley MJ. Self-assembling protein nanoparticles in the design of vaccines. *Comput Struct Biotechnol J*. 2015; 14:58-68.

Maham A, Tang Z, Wu H, Wang J, Lin Y. Protein-based nanomedicine platforms for drug delivery. *Small*. 2009; 5(15):1706-21.

Martin LJ, Hähnke MJ, Nitz M, Wöhnert J, Nicholas R, Silvaggi, Allen KR, Schwalbe H, Imperiali B. Double-Lanthanide-Binding Tags: Design, Photophysical Properties, and NMR Applications. *J. Am. Chem. Soc*. 2007; 129 (22): 7106–7113.

McCoy AJ, Grosse-Kunstleve RW, Adams PD, Winn MD, Storoni LC, Read RJ. Phaser crystallographic software. *J. Appl. Crystallogr.* 2007; 40:658-674.

Melman G, Bou-Abdallah F, Vane E, Maura P, Arosio P, Melman A. Iron release from ferritin by flavin nucleotides. *Biochim Biophys Acta.* 2013; 1830(10):4669-74.

Mihee K, Yecheol R, Kyeong SJ, Byungcheol A, Sungmin J, Heesoo K and Moonhor R. pH-dependent structures of ferritin and apoferritin in solution: disassembly and reassembly. *Biomacromolecules,* 2011; 12:1629–1640.

Mok H, Zhang M. Superparamagnetic iron oxide nanoparticle-based delivery systems for biotherapeutics. *Expert Opin Drug Deliv*. 2013; 10(1):73-87.

Molino NM, Wang SW2. Caged protein nanoparticles for drug delivery. *Curr Opin Biotechnol*. 2014; 28:75-82.

Morlando M, Dini Modigliani S, Torrelli G, Rosa A, Di Carlo V, Caffarelli E, Bozzoni I. FUS stimulates microRNA biogenesis by facilitating co-transcriptional Drosha recruitment. *EMBO J*., 2012; 31:4502-4510.

Nitz M, Franz KJ, Maglathlin RL and Imperiali B. A powerful combinatorial screen to identify high-affinity terbium(III)-binding peptides. *Chembiochem.* 2003; 4(4):272-276

Nitz M, Sherawat, M, Franz KJ, Peisach E and Allen KN. Structural origin of the high affinity of a chemically evolved lanthanide-binding peptide *Angew. Chem. Int. Ed.Engl.* 2004; 43(28):3682-3685

O'Neil JD, Dorrington KJ, Hofmann T. Luminescence and circular-dichroism analysis of terbium binding by pig intestinal calcium-binding protein (relative mass = 9000). *Can J Biochem Cell Biol*. 1984; 62(6):434-42.

Otsuka S, Maruyama H, Listowsky I. Structure, assembly, conformation, and immunological properties of the two subunit classes of ferritin. *Biochemistry* 1981; 20(18):5226-32.

Outten FW, Theil EC. Iron-based redox switches in biology. *Antioxid Redox Signal.* 2009; 11(5):1029-46.

Pandya S, Yu J, Parker D. Engineering emissive europium and terbium complexes for molecular imaging and sensing. *Dalton Trans.* 2006; (23):2757-66.

Peer D, Karp JM, Hong S, Farokhzad OC, Margalit R, Langer R. Nanocarriers as an emerging platform for cancer therapy. *Nat Nanotechnol*. 2007; 2(12):751-60.

Pettersen EF, Goddard TD, Huang CC, Couch GS, Greenblatt DM, Meng EC. Ferrin TE. UCSF Chimera–a visualization system for exploratory research and analysis, *J. Comput. Chem.* 2004; 25:1605–1612.

Pozzi C, Di Pisa F, Lalli D, Rosa C, Theil E, Turano P, Mangani S. Time-lapse anomalous X-ray diffraction shows how $Fe^{2+}$ substrate ions move through ferritin protein nanocages to oxidoreductase sites. *Acta Crystallogr D Biol Crystallogr* 2015; 71:941-953.

Pozzi C, Di Pisa F, Bernacchioni C, Ciambellotti S, Turano P, Mangani S: Iron binding to human heavy-chain ferritin. *Acta Crystallogr D Biol Crystallogr* 2015; 71:1909-1920.

Rajapakse HE, Reddy DR, Mohandessi S, Butlin NG, Miller LW. Luminescent terbium protein labels for time-resolved microscopy and screening. *Angew. Chem. Int.* 2009; 48:4990-4992

Ratnayake DB, Wai SN, Shi Y, Amako K, Nakayama H, Nakayama K. Ferritin from the obligate anaerobe Porphyromonas gingivalis: purification, gene cloning and mutant studies. *Microbiology*. 2000; 146:1119-27.

Riddles PW, Blakeley RL, Zerner B. Ellman's reagent: 5,5'-dithiobis(2-nitrobenzoic acid) - a reexamination. *Anal Biochem*. 1979; 94(1):75-81.

Robert X and Gouet P. Deciphering key features in protein structures with the new ENDscript server. *Nucleic Acids Res.*, 2014; 42:320–324.

Rosenthal PB, Henderson R. Optimal determination of particle orientation, absolute hand, and contrast loss in single-particle electron cryomicroscopy *J. Mol. Biol.* 2003; 333:721–745.

Rucker P, Torti FM, Torti SV. Role of H and L subunits in mouse ferritin. *J Biol Chem.* 1996; 271(52):33352-7.

Russo CJ, Passmore LA. Ultrastable gold substrates for electron cryomicroscopy. *Science*. 2014; 346:1377–1380.

Sana B, Johnson E, Le Magueres P, Criswell A, Cascio D, Lim S. The role of nonconserved residues of *Archaeoglobus fulgidus* ferritin on its unique structure and biophysical properties. *J Biol Chem.* 2013; 288(45):32663-72.

Sana B, Johnson E and Lim S. The unique self-assembly/disassembly property of *Archaeoglobus fulgidus* ferritin and its implications on molecular release from the protein cage. *Biochim. Biophys. Acta*, 2015; 1850:2544–2551.

Sánchez P, Valero E, Gálvez N, Domínguez-Vera JM, Marinone M, Poletti G, Corti M, Lascialfari A. MRI relaxation properties of water-soluble apoferritin-encapsulated gadolinium oxide-hydroxide nanoparticles. *Dalton Trans*. 2009; (5):800-4.

Santambrogio P, Levi S, Arosio P, Palagi L, Vecchio G, Lawson DM, Yewdall SJ, Artymiuk PJ, Harrison PM, Jappelli R, Cesareni G. Evidence that a salt bridge in the light chain contributes to the physical stability difference between heavy and light human ferritins. *J Biol Chem*. 1992; 267(20):14077-83.

Scheres SHW. Semi-automated selection of cryo-EM particles in RELION-1.3. *J. Struct. Biol*. 2015; 189:114–122.

Scheres SHW. "RELION: Implementation of a Bayesian Approach to Cryo-EM Structure Determination. *J. Struct. Biol.* 2012; 180(3):519-530.

Sculimbrene BR and Imperiali B. Lanthanide-binding tags as luminescent probes for studying protein interactions *J. Am. Chem. Soc.* 2006; 128:7346-7352

Selvin PR. Principles and biophysical applications of lanthanide-based probes. *Annu. Rev. Biophys. Biomembr*. 2002; 31:275-302.

Shirakawa M and Hiroaki H. LBT/PTD dual tagged vector for purification, cellular protein delivery and visualization in living cells *Biochim. Biophys. Acta* 2007; 1773,141-146

Stefanini S, Cavallo S, Wang CQ, Tataseo P, Vecchini P, Giartosio A, Chiancone E. Thermal stability of horse spleen apoferritin and human recombinant H apoferritin. *Arch Biochem Biophys*. 1996; 325(1):58-64.

Stefanini S, Chiancone E, Antonini E and Finazzi-Agro A. Binding of Terbium to apoferritin: a fluorescence study *Arch. Biochem. Biophys.* 1983; 222(2):430-434.

Stillman TJ, Hempstead PD, Artymiuk PJ, Andrews SC, Hudson AJ, Treffry A, Guest JR, Harrison PM. The high-resolution X-ray crystallographic structure of the ferritin (EcFtnA) of Escherichia coli; comparison with human H ferritin (HuHF) and the structures of the $Fe^{3+}$ and $Zn^{2+}$ derivatives. *J. Mol. Biol.* 2001; 307:587–603.

Su XC, Huber T, Dixon NE and Otting G. Site-specific labelling of proteins with a rigid lanthanide-binding tag. *Chembiochem.* 2006; 71:599-1604.

Suloway C, Pulokas J, Fellmann D, Cheng A, Guerra F, Quispe J, Stagg S, Potter CS, Carragher B. Automated molecular microscopy: the new Leginon system *Struct. Biol.* 2005; 151:41–60.

Swift J, Butts CA, Cheung-Lau J, Yerubandi V, Dmochowski IJ. Efficient self-assembly of *Archaeoglobus fulgidus* ferritin around metallic cores. *Langmuir*. 2009; 25(9):5219-25.

Takahashi T, Kuyucak S. Functional properties of threefold and fourfold channels in ferritin deduced from electrostatic calculations. *Biophys J*. 2003; 84(4):2256-63.

Tatur J, Hagen WR, Matias PM. Crystal structure of the ferritin from the hyperthermophilic archaeal anaerobe *Pyrococcus furiosus*. *J Biol Inorg Chem*. 2007; 12(5):615-30.

Tatur J, Hagen WR. The dinuclear iron-oxo ferroxidase center of *Pyrococcus furiosus* ferritin is a stable prosthetic group with unexpectedly high reduction potentials. *FEBS Lett*. 2005; 579(21):4729-32.

Theil EC, Behera RK, Tosha T. Ferritins for Chemistry and for Life. *Coord Chem Rev*. 2013; 257(2):579-586.

Teo RD, Termini J, Gray HB1. Lanthanides: Applications in Cancer Diagnosis and Therapy. *J Med Chem*. 2016; 59(13):6012-24.

Tortorella S, Karagiannis TC. Transferrin receptor-mediated endocytosis: a useful target for cancer therapy. *J Membr Biol*. 2014; 247(4):291-307.

Tosha T, Behera RK, Theil EC. Ferritin ion channel disorder inhibits Fe(II)/O2 reactivity at distant sites. *Inorg Chem*. 2012; 51(21):11406-11.

Toussaint L, Bertrand L, Hue L, Crichton RR, Declercq JP. High-resolution X-ray structures of human apoferritin H-chain mutants correlated with their activity and metal-binding sites. *J Mol Biol*. 2007; 365(2):440-52.

Treffry A, Zhao ZW, Quail MA, Guest JR, Harrison PM. The use of zinc(II) to probe iron binding and oxidation by the ferritin (EcFtnA) of Escherichia coli. *J. Biol. Inorg. Chem.* 1998; 3:682–688.

Treffry A, Zhao ZW, Quail MA, Guest JR, Harrison PM. How the presence of three iron binding sites affects the iron storage function of the ferritin (EcFtnA) of Escherichia coli. *FEBS Lett*. 1998; 432:213–218.

Treffry A, Harrison PM. Spectroscopic studies on the binding of iron, terbium, and zinc by apoferritin. *J. Inorg. Biochem.* 1984; 21(1):9-20.

Truffi M, Fiandra L, Sorrentino L, Monieri M, Corsi F, Mazzucchelli S. Ferritin nanocages: A biological platform for drug delivery, imaging and theranostics in cancer. *Pharmacol Res*. 2016; 107:57-65.

Uchida M, Flenniken ML, Allen M, Willits DA, Crowley BE, Brumfield S, Willis AF, Jackiw L, Jutila M, Young MJ, Douglas T. Targeting of cancer cells with ferrimagnetic ferritin cage nanoparticles. *J Am Chem Soc.* 2006; 128(51):16626-33.

Uchida M, Kang S, Reichhardt C, Harlen K, Douglas T. The ferritin superfamily: Supramolecular templates for materials synthesis. *Biochim Biophys Acta.* 2010; 1800(8):834-45.

Vande Velde G, Rangarajan JR, Toelen J, Dresselaers T, Ibrahimi A, Krylychkina O, Vreys R, Van der Linden A, Maes F, Debyser Z, Himmelreich U, Baekelandt V. Evaluation of the specificity and sensitivity of ferritin as an MRI reporter gene in the mouse brain using lentiviral and adeno-associated viral vectors. *Gene Ther*. 2011; 18(6):594-605.

Vannucci L, Falvo E, Failla CM, Carbo M, Fornara M, Canese R, Cecchetti S, Rajsiglova L, Stakheev D, Krizan J, Boffi A, Carpinelli G, Morea V and Ceci P. In Vivo Targeting of Cutaneous Melanoma Using an Melanoma Stimulating Hormone-Engineered Human Protein Cage with Fluorophore and Magnetic Resonance Imaging Tracers. *J. Biomed. Nanotechnol*., 2015; 11:81–92.

Vannucci L, Falvo E, Fornara M, Di Micco P, Benada O, Krizan J, Svoboda J, Hulikova-Capkova K, Morea V, Boffi A and Ceci P. Selective targeting of melanoma by PEG-masked protein-based multifunctional nanoparticles. *Int. J. Nanomed*., 2012; 7:1489–1509.

Wagenknecht T, Grassucci R, Frank J. Electron microscopy and computer image averaging of iceembedded large ribosomal subunits from Escherichia coli. *J. Mol. Biol.* 1988; 199:137–147.

Waidner B, Greiner S, Odenbreit S, Kavermann H, Velayudhan J, Stähler F, Guhl J, Bissé E, van Vliet AH, Andrews SC, Kusters JG, Kelly DJ, Haas R, Kist M, Bereswill S. Essential role of ferritin Pfr in Helicobacter pylori iron metabolism and gastric colonization. *Infect Immun*. 2002; 70(7):3923-9.

Watt RK, Hilton RJ, Graff DM. Oxido-reduction is not the only mechanism allowing ions to traverse the ferritin protein shell. *Biochim. Biophys. Acta* 2010; 1800(8):745–759.

Winn MD, Ballard CC, Cowtan KD, Dodson EJ, Emsley P, Evans PR, Keegan RM, Krissinel EB, Leslie AG, McCoy A, McNicholas SJ, Murshudov GN, Pannu NS, Potterton EA, Powell HR, Read RJ, Vagin A, Wilson KS. Overview of the CCP4 suite and current developments *Acta Crystallogr. D Biol. Crystallogr*. 2011; 67(4):235-242.

Wo¨hnert J, Franz KJ, Nitz M, I mperiali B and Schwalbe H. Protein alignment by a coexpressed lanthanide-binding tag for the measurement of residual dipolar couplings. *J. Am.Chem. Soc.* 2003; 125:13338-13339

Yang X, Arosio P, Chasteen ND. Molecular diffusion into ferritin: pathways, temperature dependence, time, and concentration effects. *Biophys. J.* 2000; 78:2049–2059.

Yang X, Chastee ND. Molecular diffusion into horse spleen ferritin: a nitroxide radical spin probe study. *Biophys. J.* 1996; 71:1587–1595.

Yang X, Chen-Barrett Y, Arosio P, Chasteen ND. Reaction paths of iron oxidation and hydrolysis in horse spleen and recombinant human ferritins. *Biochemistry*. 1998; 37(27):9743-50.

Yang Z, Wang X, Diao H, Zhang J, Li H, Sun H, Guo Z. Encapsulation of platinum anticancer drugs by apoferritin. *Chem Commun (Camb).* 2007; (33):3453-5.

Yoshimura H. Protein-assisted nanoparticle synthesis. *Colloid Surf A Physicochem Eng Asp* 2006; 282–283:464–70.

Xing R, Wang X, Zhang C, Zhang Y, Wang Q, Yang Z, Guo Z. Characterization and cellular uptake of platinum anticancer drugs encapsulated in apoferritin. *J Inorg Biochem*. 2009; 103(7):1039-44.

Xing M, Yan F, Yu S, Shen P. Efficacy and Cardiotoxicity of Liposomal Doxorubicin-Based Chemotherapy in Advanced Breast Cancer: A Meta-Analysis of Ten Randomized Controlled Trials. *PLoS One*. 2015 Jul 23; 10(7):e0133569. eCollection 2015.

Xu B, Chasteen ND. Iron oxidation chemistry in ferritin. Increasing Fe/O2 stoichiometry during core formation. *J Biol Chem*. 1991; 266(30):19965-70.

Xu X, Liu Q, Liu Y, Xie Y. Terbium(III) fluorescence probe studies on metal ion-binding sites in anticoagulation factor I from Agkistrodon acutus venom. *J Protein Chem*. 2002; 21(2):123-9.

Zhang Y, Orner BP. Self-assembly in the ferritin nano-cage protein superfamily. *Int J Mol Sci*. 2011; 12(8):5406-21.

Zhang L, Li L, Di Penta A, Carmona U, Yang F, Schöps R, Brandsch M, Zugaza JL, Knez M. H-Chain Ferritin: A Natural Nuclei Targeting and Bioactive Delivery Nanovector. *Adv Healthc Mater*. 2015; 4(9):1305-10.

Zhang B, Watt RK, Gálvez N, Domínguez-Vera JM, Watt GD. Rate of iron transfer through the horse spleen ferritin shell determined by the rate of formation of Prussian blue and Fe-desferrioxamine within the ferritin cavity, *Biophys. Chem*. 2006; 120:96–105.

Zhao G1, Bou-Abdallah F, Arosio P, Levi S, Janus-Chandler C, Chasteen ND. Multiple pathways for mineral core formation in mammalian apoferritin. The role of hydrogen peroxide. *Biochemistry*. 2003; 42(10):3142-50.

Zhen Z, Tang W, Todd T, Xie J. Ferritins as nanoplatforms for imaging and drug delivery. *Expert Opin Drug Deliv*. 2014; 11(12):1913-22.

Zheng H, Cooper DR, Porebski PJ, Shabalin IG, Handing KB, Minor W. Check My Metal: a macromolecular metal-binding validation tool *Acta Crystallogr. D Struct. Biol.* 2017; 73(3):223-233.

Zheng SQ, Palovcak E, Armache JP, Cheng Y, Agard DA. Anisotropic Correction of Beam-induced Motion for Improved Single-particle Electron Cryo-microscopy. *Nature Methods* 2016; 14:331–332.

# APPENDIX I

Biochimica et Biophysica Acta 1861 (2017) 450–456

Contents lists available at ScienceDirect

Biochimica et Biophysica Acta

journal homepage: www.elsevier.com/locate/bbagen

# Probing bulky ligand entry in engineered archaeal ferritins

Lorenzo Calisti [a], Irene Benni [a], Matilde Cardoso Trabuco [a], Paola Baiocco [b], Barbara Ruzicka [c], Alberto Boffi [a,d], Elisabetta Falvo [d], Francesco Malatesta [a], Alessandra Bonamore [a,*]

[a] Department of Biochemical Sciences "Alessandro Rossi Fanelli", Sapienza University of Rome, P.le Aldo Moro 5, I-00185 Rome, Italy
[b] Center for Life Nano Science@Sapienza, Istituto Italiano di Tecnologia, V.le Regina Elena 291, Rome I-00185, Italy
[c] Istituto dei Sistemi Complessi del Consiglio Nazionale delle Ricerche (ISC-CNR) Sede Sapienza and Dipartimento di Fisica, Sapienza University of Rome, P.le Aldo Moro 5, I-00185 Rome, Italy
[d] Istituto di Biologia e Patologia Molecolari, Consiglio Nazionale delle Ricerche (IBPM-CNR) Sede Sapienza University of Rome, P.le Aldo Moro 5, I-00185 Rome, Italy

ARTICLE INFO

*Article history:*
Received 31 May 2016
Received in revised form 1 September 2016
Accepted 11 October 2016
Available online 15 October 2016

*Keywords:*
Self-assembly
Binding kinetics
Nano-scaffold
Ferritin

ABSTRACT

*Background:* A set of engineered ferritin mutants from *Archaeoglobus fulgidus* (Af-Ft) and *Pyrococcus furiosus* (Pf-Ft) bearing cysteine thiols in selected topological positions inside or outside the ferritin shell have been obtained. The two apo-proteins were taken as model systems for ferritin internal cavity accessibility in that Af-Ft is characterized by the presence of a 45 Å wide aperture on the protein surface whereas Pf-Ft displays canonical (three-fold) channels.
*Methods:* Thiol reactivity has been probed in kinetic experiments in order to assess the protein matrix permeation properties towards the bulky thiol reactive DTNB (5,5′-dithiobis-2-nitrobenzoic acid) molecule.
*Results:* Reaction of DTNB with thiols was observed in all ferritin mutants, including those bearing free cysteine thiols inside the ferritin cavity. As expected, a ferritin mutant from Pf-Ft, in which the cysteine thiol is on the outer surface displays the fastest binding kinetics. In turn, also the Pf-Ft mutant in which the cysteine thiol is placed within the internal cavity, is still capable of full stoichiometric DTNB binding albeit with an almost 200-fold slower rate. The behaviour of Af-Ft bearing a cysteine thiol in a topologically equivalent position in the internal cavity was intermediate among the two Pf-Ft mutants.
*Conclusions and general significance:* The data thus obtained indicate clearly that the protein matrix in archaea ferritins does not provide a significant barrier against bulky, negatively charged ligands such as DTNB, a finding of relevance in view of the multiple biotechnological applications of these ferritins that envisage ligand encapsulation within the internal cavity.



## 1. Introduction

Ferritins from a variety of species have emerged as versatile scaffolds for a number of diverse nanotechnological applications spanning from the synthesis of metal nanoparticles to drugs or diagnostics delivery. The most notable property of ferritins resides in their ability to sequester metals as well as small molecules within their internal cavities. Ferritin proteins are by far the best-studied biomineralisation scaffolds in that these proteins are able to accommodate up to 4500 iron atoms in an iron (III) oxide form within the central cavity. Iron (II) is oxidised within the ferroxidase centers located at the entrance of ferritin pores (threefold channels on the protein surface) and subsequently transferred to the central cavity and mineralised as iron (III) oxide nanocrystals. Thereafter, under physiological reducing conditions, the iron (III) oxide can be reverted to iron (II) and diffuses out of the cavity, most likely through negatively charged pores in the ferritin shell, formed between subunits [1]. These channels allow for the entry and exit of cations during mineralisation and demineralisation and display a relatively broad selectivity thus allowing for the accumulation of a variety of metal ions, with a preference for divalent cations. These properties have been used to develop ferritin as a drug delivery platform [2]. At physiological pH ferritin exists as a stable 24-mer, whereas in highly acidic or basic solutions it disassembles reversibly thereby spontaneously reassembling as neutral pH is restored. The reversible subunit assembly has been used to trap molecules in solution within its cavity simply by changing pH in the presence of the desired molecule. This property has been used to load the cavity with metal containing drugs, such as the cancer drug cisplatin [3,4], and the iron chelator desferrioxamine B [5,6], as well as a variety of organic and inorganic compounds, including metal nanoparticles.

The incorporation of non-metal-containing drugs within ferritin is however challenging due to the limited interactions with the ferritin shell, and the diffusion of these molecules through the surface pores. Strategies to overcome these problems have focused on complexing

* Corresponding author.
*E-mail addresses:* alessandra.bonamore@uniroma1.it, alessandra.bonamore@gmail.com (A. Bonamore).

http://dx.doi.org/10.1016/j.bbagen.2016.10.007
0304-4165/

drugs with transition metals, such as Cu(II), prior to their internalisation [7], or the addition of charged accessory molecules such as poly-L-aspartic acid to optimise loading of ferritin with drugs [8]. By combining the loading of ferritin with drugs and surface modification with peptide epitopes and labels, ferritin can be specifically targeted to particular cell types and tumours for efficient delivery of therapeutic agents [9]. Thus far, ferritins and other protein nanocages show a great deal of promise that will hopefully transfer to a clinical setting.

Nevertheless, molecular diffusion in and out of the ferritin cavity appears to be a complex phenomenon that is only partially understood. The pathway of iron entry inside the ferritin cavity is characterized by the presence of eight protein ion channels positioned around the three-fold symmetry axes of the cage and delimited by three proximal subunits. Such ion channels are about 15 Å in length and 5–6 Å in diameter. Because hydrated ions have diameters of about 6.5 Å, partial dehydration is thought to occur for ion passage through the channel. On this basis, possible entry of larger ligands of physiological interest (e.g. iron III reductants) or other small organic molecules may seem unlikely. However, a large number of experimental observations, mostly carried out on mammalian ferritins heteropolimers or recombinant H and L homopolimers, pointed out that small organic molecules can permeate the protein shell, possibly through the same negatively charged three-fold channels that govern metal ions fluxes [10–12]. The permeation of small molecules into ferritins at physiological temperature and pH has been shown to be a charge-selective process in both native, H and L-chains of several mammalian proteins having similar channel structures [13]. A number of studies thus supported the hypothesis that the threefold channels are indeed the primary avenues of entry into the protein cavity of small molecules endowed with cationic properties [14]. The complete exclusion of the negatively charged probes from the interior of these proteins has been elegantly demonstrated by means of spin labeled molecules [11]. At the same time, the permeability of the same molecules in mutated proteins bearing positively charged groups along the three fold channels has been demonstrated [15,16]. More recently, however, many different ferritins from phylogenetically distinct trees have been identified and characterized. Among these, highly thermostable ferritins from Archaea emerged as privileged scaffolds in view of their remarkable thermal stability, easy expression in high yields in common *E. coli* cells and, at least in a few examples, uncommon association-dissociation properties. In particular, archaeal ferritins from *Archaeoglobus fulgidus* (Af-Ft) and *Pyrococcus furiosus* (Pf-Ft) emerged as most interesting tools for diverse applications. In spite of the high sequence similarity (50 and 70% amino acid sequence identity and similarity, respectively), Pf-Ft and Af-Ft do not share the same quaternary assembly. In fact, whereas the Pf-Ft 24-mer has the canonical 432 point-group symmetry, the Af-Ft 24-mer displays a 23 point-group symmetry typical of smaller 12-mer ferritin-like proteins. This unusual assembly does not display the 4-fold channels and constrains the quaternary structure thus leading to the appearance of four large triangular openings about 45 Å wide in the protein shell [17]. To date, Af-Ft assembly, here referred to as an "open" structure, is considered unique among all other known structures of tetraeicosameric ferritins. The stability of this tetrahedral configuration is governed by two critical residues in the helix E of the 4-helices bundle, namely K150 and R151. Indeed, the structure of Af-Ft K150A/R151A mutant reported by Sana et al. [18], shows a typical "closed" octahedral symmetry.

However, diffusion of small molecules within archaeal ferritins have been little investigated. Differences in the nature, shape and properties of open pores within these ferritins thus provide novel possible routes for small molecules entry/incorporation thus expanding the scope of possible biotechnological applications of these proteins. In the present work, we have engineered a set of Pf-Ft, Af-Ft ("open") and Af-Ft K150A/R151A ("closed") mutants by placing reactive cysteine residues in the same topological positions either inside or outside the internal cavity. The reactivity of the bulky, negatively charged DTNB molecule has been probed in the set of available mutants.

## 2. Materials and methods

### 2.1. Point mutations and protein expression

The genes encoding for bacterial ferritin from Af-Ft and Pf-Ft were cloned into the expression vector pET22b (Novagen). Point mutants Af-FtM54C, Af-FtM54C/K150A/R151A, Pf-FtG52C and Pf-FtP77C were obtained by PCR using QuickChange Mutagenesis kit (Stratagene). The recombinant plasmids were transformed into *E. coli* TOP 10 cells and the resulting colonies were screened by DNA sequencing. Plasmids bearing the desired mutations were transformed into BL21(DE3) *E. coli* strain for protein expression. For each mutant, protein over-expression was obtained as follows: 1 L LB broth medium was inoculated with 2 ml overnight culture of a single colony and the gene expression was induced with 1 mM IPTG when the absorbance at 600 nm reached 0.6. Cells were harvested by centrifugation after overnight induction at 37 °C and the cell pellets were stored at −20 °C.

### 2.2. Protein purification

Harvested cells form 1 l colture over-expressing Af-FtM54C and Af-FtM54C/K150A/R151A mutants were resuspended in 20 ml buffer A (25 mM HEPES pH 7.5, 20 mM $MgCl_2$) containing a cOmplete™ Mini Protease Inhibitor Cocktail Tablet (Roche) and disrupted by sonication. The soluble fraction was thermally purified by heating at 85 °C for 10 min followed by removal of denatured proteins by centrifugation at 14000 rpm for 30 min at 4 °C. The supernatant was fractioned by ammonium sulfate precipitation. 70% ammonium sulfate pellet containing highly purified protein was resuspended in buffer A, dialysed versus the same buffer, sterile filtered and stored at 4 °C. Cells over-expressing Pf-FtG52C and Pf-FtP77C were sonicated in 25 mM HEPES buffer at pH 7.5 containing 0.5 mM EDTA, 0.3 M NaCl and cOmplete™ Mini Protease Inhibitor Cocktail Tablet. After sonication, the crude bacterial extract was digested with DNase for 1 h at 37 °C, heated at 55 °C for 10 min and then at 80 °C for 8 min. Heat treatment was followed by centrifugation to remove insoluble material and ammonium sulfate precipitation. 70% ammonium sulfate pellet was resuspended in 20 mM HEPES pH 7.5 plus 150 mM NaCl, dialysed versus the same buffer and loaded onto a HiLoad 26/600 Superdex 200 pg column (GE Healthcare). Fractions containing highly purified protein were pooled, sterile filtered and store at 4 °C.

### 2.3. Preparation of ferritin-DTNB adducts

All mutants were reduced with 3 mM TCEP (tris(2-carboxyethyl)phosphine) in their storage buffers and then loaded onto a desalting column (GE Healthcare) to remove the reducing agent. Each mutant was reacted with 40-fold molar excess of Ellman's Reagent, (DTNB) per cysteine for 3 h at room temperature. Stock DTNB solutions were prepared in ethanol. The excess (non-reacted) reagent was removed by ultra-filtration using 100 kDa Amicon Ultra-15 centrifugal devices (Millipore Corporate). The Ferritin–DTNB samples were analyzed by mass spectrometry as described below.

### 2.4. Stopped flow experiments

Kinetic measurements were carried out on a thermostated Applied Photophysics stopped-flow apparatus (Leatherhead, UK) by mixing 8–10 μM protein solutions, previously reduced with TCEP, with solutions containing different concentrations of DTNB (from 0.2 to 0.7 mM after mixing) in 20 mM HEPES, 20 mM $MgCl_2$ pH 7.5. In order to avoid interference of the instrument phototube from the high concentrations of DTNB and the released chromophore 5-thio-2-nitro-benzoic acid (TNB), the reaction was followed at 430 nm and the extinction coefficient calculated to be 12205 $mM^{-1}$ $cm^{-1}$, as determined from the extinction coefficient of 14150 $mM^{-1}$ $cm^{-1}$ at 412 nm [19]. All fitting

procedures were carried out by using the Matlab software (Mathworks, USA). Experimental traces were fitted by non-linear regression to either exponential of biexponential processes by using an Levenberg-Marquardt algorithm.

### 2.5. Self-assembly study

$MgCl_2$ -mediated self-assembly of ferritin mutants was studied by incubating aliquots of proteins (1 mg/ml) with different salt concentrations in 25 mM HEPES buffer, pH 7.5. Molecular sizes of Af-FtM54C, Af-FtM54C/K150A/R151A, Pf-FtG52C and Pf-FtP77C was determined by size exclusion chromatography (SEC) using HiPrep 16/60 Sephacryl S300 column (GE Healthcare). The column was equilibrated with 25 mM HEPES, pH 7.5, containing $MgCl_2$ at the same concentration in which the protein was pre-incubated and the same buffer was used as mobile phase. Molecular weight of each mutant were determined by comparing their elution volumes with the elution volumes of standard proteins in the same salt concentration.

Dynamic light scattering measurements (DLS) were performed using an ALV-5000 logarithmic correlator in combination with a standard optical set-up based on a He–Ne ($\lambda = 632.8$ nm) 10 mW laser and a photomultiplier detector. The intensity autocorrelation functions were directly obtained as $g_2(q, t) = \langle I(q, t)I(q, 0)\rangle/\langle I(q, 0)\rangle^2$, where q is the modulus of the scattering vector defined as $q = (4\pi n/\lambda)\sin(\theta/2)$ ($\theta = 90°$ in the present experiment). The raw measurements as directly obtained, without any data corrections are shown in Fig. 1 for different samples without added salt (black symbols) and at different $MgCl_2$ concentrations between 5 and 30 mM (colored symbols as described in the legend. Quantitative analysis of the measurements was obtained through a fit of the data with a single exponential expression: $g_2(q, t) = 1 + be^{-t/\tau}$ where b is the coherence factor and $\tau$ is the relaxation time related to the motion of the particles, specifically to the diffusion coefficient [20].

### 2.6. Protein LC–MS

LC–MS was performed on protein samples before and after DTNB titration, after dialysis in distilled water in the presence of 0.1 mM EDTA, using a Waters AcquityuPLC connected to Waters Acquity Single Quad Detector. A Hypersil Gold C4 column was used: 1.9 μm, 2.1 × 50 mm at 254 nm observation wavelength; mobile phase: 95:5 water (0.1% formic acid):MeCN (0.1% formic acid); gradient over 6 min (to 5:75 water (0.1% formic acid):MeCN (0.1% formic acid); flow rate: 0.4 ml $min^{-1}$; MS mode was set at a scan range: $m/z = 250–2{,}000$ (ES+); scan time: 0.25 s. Data were obtained in continuum mode by setting the electrospray source of the MS with a capillary voltage of 3.5 kV and a cone voltage of 50 V. $N_2$ gas was used as nebulizer and desolvation gas at a total flow of 300 l/h. Ion series were generated by integration of the ultraviolet-absorbance (at 254 nm) chromatogram over 1.2–1.8 min range. Mass spectra were subsequently reconstructed for proteins from the ion series using the MaxEnt 1 algorithm on MassLynx software program.

## 3. Results

### 3.1. Assessment of ferritin mutants assembly

In order to assess the association state of the engineered ferritin mutants Af-FtM54C, Af-FtM54C/K150A/R151A, Pf-FtG52C and Pf-FtP77C, all proteins were studied by DLS and SEC as a function of $MgCl_2$ concentration. A full characterization of Af-FtM54C association state is reported in Fig. 1. Data relative to the other mutants are reported as Supplementary materials (Figs. S1, S2 and S3). Fig. 1 clearly shows that the shape of the curve without added salt is significantly different from that observed in the presence of added salt. This behavior is confirmed by data fitting obtained as described under Methods section. The fitting

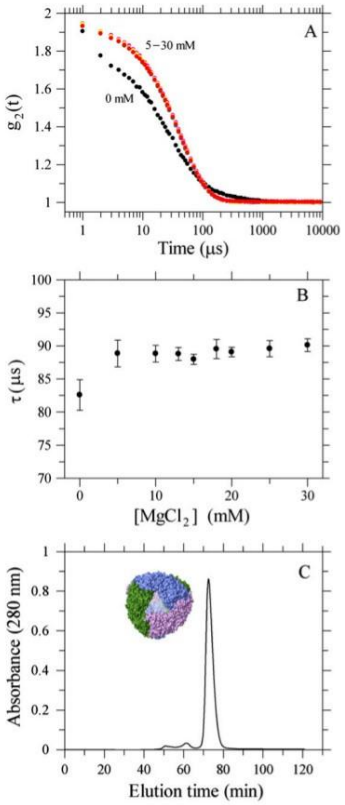


**Fig. 1.** Polymeric assembly of *Archaeoglobus fulgidus* ferritin mutants. A) Dynamic Light Scattering intensity correlation functions of Af-FtM54C at different $MgCl_2$ concentrations indicated in the legend. The curves at different $MgCl_2$ are all superimposed. B) Dynamic Light scattering relaxation time of Af-FtM54C as a function of $MgCl_2$ concentration. C) Gel filtration profiles of Af-FtM54C at 20 mM $MgCl_2$.

curves appears to interpolate very well experimental data in presence of salts whereas are less accurate for samples without added salt, where the addition of polydispersity is necessary.

Pf-Ft mutants are stable 24-mers (~490 kDa) independent of salt concentration, whereas the self-assembly of Af-Ft mutants was strongly dependent on ionic strength. $MgCl_2$ was used as polymerizing salt at variance with previous reports [18] in which NaCl was used. As a result, it appeared that at our working concentration (20 mM $MgCl_2$) all the proteins are structured as a stable 24-meric cage. It is noticeable that the 24-mer to dimer ratio increases with increasing $MgCl_2$ concentration from 0 to 20 mM, whereas at least 100 mM NaCl concentration of NaCl are needed to reach full polymerization (data not shown). Thus, it appears that divalent cations such as $Mg^{2+}$ and $Ca^{2+}$ are more effective in promoting the 24-mer association with respect to NaCl. The

comparison between SEC and DLS data on Af-FtM54C and Af-FtM54C/K150A/R151A however need further comments. First of all, the heterogeneous, polydisperse population observed in the absence of divalent cations is manifest in the presence of both low molecular weight species (presumably dimers as reported in refs. [16–18]) and distributed high molecular weight polymers (present in much lower amount), apparently in a proportion even higher than the canonical 24-mers. Addition of $MgCl_2$ at 5–10 mM concentration brings about a very sharp transition in both Af-Ft mutants resulting in the formation of homogeneous and stable 24-mer species. At 20 mM $MgCl_2$ concentration, all proteins investigated are consistent with a stable 24-mer assembly.

### 3.2. Kinetics of DTNB binding to Pf-Ft and Af-Ft mutants

The kinetics of the disulfide exchange reaction of DTNB with cysteine residues on ferritin mutants were carried out by stopped-flow spectroscopy. The kinetics, determined under pseudo-first order conditions, appeared to be multiexponential and were followed to the maximum time possible with the instrument (1000 s). Independent experiments performed by using UV-visible absorption spectroscopy and LC–MS (see below) confirmed the essentially complete cysteine reactivity. As Fig. 2A shows, the time scales of the four ferritin mutants are significantly different. As expected, the Pf-Ft P77C mutant bearing the cysteine residue on the convex outer surface displayed the fastest reactivity as compared to Pf-Ft G52C which carries the mutation inside the ferritin tetraeicosamer. A complete set of time courses of the Pf-Ft P77C mutant has been carried out increasing DTNB concentration and reported in Supplementary Materials (Fig. S4). Within the observed time frame all traces could be fit to a simple relaxation process with apparent second-order rate constants of *ca.* 900 $M^{-1}$ $cm^{-1}$ (see also Table 1). The Af-Ft mutants had an intermediate behaviour in the reaction with DTNB. Quite unexpectedly the Af-Ft M54C mutant, in which the internal cysteine reacts with DTNB in a facilitated way through the four 45-Å large triangular openings in the protein shell, could only be fit by a biexponential process in which the fastest second-order rate constant was of the same order of magnitude determined for the Pf-Ft P77C mutant (Table 1). Finally, closure of the openings by introduction of the K150A/R151A mutations in Af-M54C brought about a significant quenching of the ligand binding rate. The complete set of kinetic traces for each mutant were also fit by either exponential or biexponential relaxations with second-order rate constants as reported in Supplementary materials (Fig. S5). Overall these results indicate that the diffusion of molecules across the proteinaceous barrier of closed ferritin 24-mers can be accurately measured and secondly that contrary to intuition and reported data (see discussion section) the protein shell

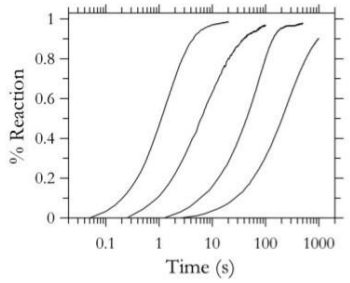


**Fig. 2.** Kinetics of DTNB binding to Af-Ft and Pf-Ft mutants. A. Comparison of the reaction time scales of all mutants; from left to right, Pf-FtP77C, Af-FtM54C, Af-FtM54C/K150A/R151A, and Pf-FtG52C. All mutants were 5 μM except Af-FtM54C which was 4 μM, and DTNB was 0.7 mM.

**Table 1**
Apparent second-order constants for ferritin mutants as determined by the DTNB reaction.

| Protein | Cysteine position | $k_{OBS}$ ($M^{-1}$ $s^{-1}$) |
|---|---|---|
| Pf-FtP77C | External | 908 ± 122 |
| Pf-FtG52C | Internal | 5 ± 1 |
| Af-FtM54C open | Internal | Fast: 198 ± 65<br>Slow: 51 ± 21 |
| Af-FtM54C/K150A/R151A closed | Internal | 26 ± 2 |

permeability to bulky molecules such as DTNB is much higher than expected. These results bear relevant implications discussed below in so far as ligand encapsulation and delivery is concerned.

### 3.3. LC/MS data

LC–MS measurements were performed on the selected point mutants Af-FtM54C, Af-FtM54C/K150A/R151A, Pf-FtG52C and Pf-FtP77C after titration with DTNB in comparison with unreacted proteins. In all samples, ferritins were eluted as monomers of molecular weight of about 21 kDa, and DTNB reacted proteins showed a shifted peak of + 198 ± 2 Da, in agreement with the expected molecular weight of the thio-nitrobenzoic moiety. In all samples reaction was complete with the exception of Pf-Ft G52C protein in which 18 % of unreacted protein was present (Supplementary materials, Fig. S6).

## 4. Discussion

The present data highlight notable properties related to bulky ligands penetration through prototypic archaeal ferritin homopolymers that are relevant both to the general ligand entry/escape mechanism and to the widespread nanotechnological applications of these proteins [21,22].

The experimental set up was designed around four mutants of Pf-Ft and Af-Ft bearing a cysteine residue per subunit either in topologically equivalent positions inside the 24-mer cavity (Af-FtM54C, Af-FtM54C/K150A/R151A, Pf-FtG52C) or outside the 24-mer cage in the Pf-FtP77C mutant (see Fig. 3). In this framework, access to the reactive sulfidryls is totally unhindered on the protein external surface in Pf-FtP77C, partially hindered in the internal cavity in Af-FtM54C and totally hindered in the internal cavity in Af-FtM54C/K150A/R151A and Pf-FtG52C. The overall picture that emerges from the body of experimental results is that even fully assembled, closed Af-FtM54C/K150A/R151A and Pf-FtG52C structures are capable of stoichiometric binding of the bulky, negatively charged, DTNB ligand. These results indicate that the permeation of negatively charged molecular species of 8–10 Å length and 5–6 Å diameter into archaeal ferritins does occur at variance with the reported exclusive entry of positively charged or neutral species only in vertebrate ferritins [13,14]. Charge selectivity was reported in the case of horse spleen ferritin (HoSF) and human H-chain ferritin (HuHF) and was correlated to the nature of threefold channels, endowed with hydrophilic, negatively charged tunnels involved in iron uptake [23]. Electron paramagnetic resonance spectroscopy and gel permeation chromatography studies with HoSF demonstrated that molecular charge and polarity of the diffusants play a critical role in their permeation into ferritin [14]. Kinetic studies of permeation using small nitroxide spin probes also confirmed the role of these channels as providing a charge-selective pathway for entry into the cavity [10]. A negatively charged nitroxide was completely excluded from the interior of the protein, whereas positively charged and polar nitroxide radicals penetrated the protein shell to interact with the iron core. Mutated HuHF (D131H/E134H), where the negatively charged glutamate and aspartate residues lining the threefold channels are replaced by histidines, partially allowed the entry of negatively charged species (4-carboxyTEMPO radical) thus providing strong evidence that the negatively charged threefold channels are the principal pathways for molecular

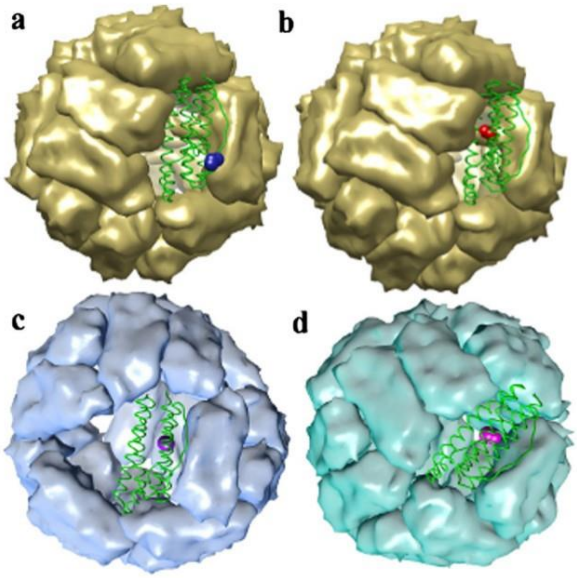


**Fig. 3.** Three-dimensional structures of the ferritin mutants. A monomer is depicted as green ribbon and the cysteine residues are represented in CPK style for clarity. a) Pf-FtP77C: the external cysteine is shown as blue spheres. b) Pf-FtC52C: the internal cysteine is depicted in red (models a) and b) built on Pf-Ft structure, PDB ID: 2JD6). c) Af-Ft54C: the internal cysteine is depicted in purple. d) Af-FtM54C/K150A/R151A: the internal cysteine in magenta (models c) and d) built on Af-Ft structure, (PDB ID: 1SQ3)). Molecular graphics and analyses were performed with the UCSF Chimera package [25].

diffusion into ferritin [10]. Interestingly, first-order half-lives for permeation of positively charged compounds in mammalian ferritins are in the same time range of those observed in DTNB uptake in fully closed Af-FtM54C/K150A/R151A and Pf-FtG52C archaeal ferritins although Af-Ft and Pf-Ft have been reported to show a different amino acid arrangement in the threefold channels that suggested a different ligand incorporation mechanism.

In particular, the eight threefold channels in each protein are shaped by the C-terminal segment of C helix and the N-terminus of D helix in the 4-helix bundle of three adjacent monomers [24]. Thus, C-terminal ends of helices C define the outer entrance to the channel and the N-termini of helices D define the inner entrance. In the case of Pf-Ft, channels are similar to those of HuHF in the outer side, that is rich in negative aminoacids (Glu109, Glu110 and Glu111), whereas they differ in the central region due to the presence of polar and positively charged residues (Tyr114 and Arg117). Lastly, the inner entrance of the channel is characterized by the presence of Ala118 and Glu121, in the topological position which is deemed essential for the transfer of iron (II) to the ferroxidasic center in mammalian ferritins [26].

In the case of Af-Fts, namely Af-FtM54C ("open" form) and Af-FtM54C/K150A/R151A ("closed" form), the threefold channels are lined by a mix of hydrophobic and hydrophilic aminoacids: only one glutamate (Glu113; PBD ID: 1SQ3 and 3KX9) is located to the entrance and two acidic residues lining HuHF channels (D131 and E134) (PDB ID:2FHA) are replaced by neutral and positively charged residues (Tyr119 and Asn 120). Thus, in the case of Af-Ft, the cluster of negative charges characteristic of HuHF is not present, presumably because it is not necessary to drive iron (II) atoms towards the ferroxidasic site, readily available through the large pores present in this protein. Hence, the threefold channels of archaeal ferritins are less negatively charged than the mammalian ones, possibly allowing the entrance of negatively charged compounds (see Fig. 4). Of course, the "open" Af-FtM54C, here investigated, displays the four 45 Å wide triangular pores, defined by C and D helices, characterized by the presence of a group of positive charged residues located at the three apices [17]. These large openings are most likely preferential paths for large ligand entry into the cavity as demonstrated by the 8 fold faster DTNB reaction rate with the internal thiol with respect to the closed Af-FtM54C/K150A/R151A mutant (see Table 1). In turn, the DTNB entry rate into Af-FtM54C/K150A/R151A mutant is 5 fold faster than in the Pf-FtG52C protein. Such difference is significant in view of the fact that the last two proteins are assimilated to closed cages with thiols in topologically equivalent positions.

As a last comment it is worth considering the possible role of the so-called fourfold channels. As matter of fact, the quaternary assembly of the closed Af-FtM54C/K150A/R151A mutant is similar to that of Pf-FtG52C and other mammalian Ft cages displaying a canonical octahedral conformation with fourfold channels of 4–5 Å size. The six fourfold channels of Pf-Ft (PDB ID: 2JD6) are polar and hydrophilic. Moreover, Lys145 in the DE loop (corresponding to Lys 150 in Af-Ft), which forms an outer gate to the fourfold channel, makes this entrance more polar and charged than that of HuHF, which is basically uncharged. Nevertheless, the dimensions of the fourfold channel in both mammalian and archaeal ferritins is found to be too small even to metal ions with the possible exception of protons and cannot be taken as a possible option for the entry of organic molecules.

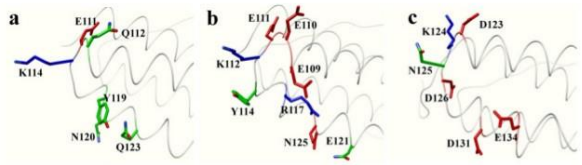


**Fig. 4.** Profile view of the lining amino acids in the threefold channel in a) Af-Ft (PDB ID: 1SQ3) and b) Pf-Ft (PDB ID: 2JD6) with respect to c) HuHF (PDB ID: 2FHA). The exterior of the shell lies on the left side and the inner cavity on the right side of each cartoon as shown schematically. Positive, negative and polar residues are depicted as blue, red and green sticks, respectively.

Thus, on the basis of the observed DTNB binding rates and available crystallographic structures we conclude that archaeal ferritins from *P. furiosus* and *A. fulgidus* are able to incorporate negatively charged, modestly sized diffusants, even in their fully "closed" forms, most likely through the threefold channels whose nature appears less restrictive with respect to that of vertebrate proteins. Possibly, the presence of positively charged residues in the middle of the threefold channel may favour entrance of negatively charged species in the archaeal proteins. As a last comment, it must also be pointed out that the dimensions of the currently used probe slightly exceed the diameter of the threefold channel as inferred from crystal structure coordinates. A mechanism of rotameric adjustment of relevant aminoacid side chains is thus necessary in order to allow for the entry/exit of small organic molecules. Recent demonstration of multiple conformers in aminoacids lining the inner entrance to the ferritin cavity may explain the necessary plasticity of the threefold channels in ferritins [26].

## 5. Conclusions

The results of the present work indicate that molecular diffusion into archaeal ferritin is a complex phenomenon and that even apparently closed, impermeable structures, ferritins do allow entry of 8–10 Å long organic molecules with no necessity of 24-mer desassembly. The data thus obtained indicate clearly that the protein matrix in archaeal ferritins does not provide a significant barrier against bulky, negatively charged ligands such as DTNB, a finding of relevance in view of the multiple biotechnological applications of these ferritins that envisage ligand encapsulation within the internal cavity. The potential impact of such engineered ferritins on the general topics related to their biotechnological application is wide. On the side of material science, the possibility of disposing of a cations dependent self-assembling cage provides the basis of unique "molecular carpentry" tools. On the side of biomedical applications, the use of archaeal proteins must still be explored. The entry of archaeal ferritins into mammalian cells is under investigation in order to clarify their receptor recognition properties, the pathways of intracellular trafficking, the impact on eukaryotic cell iron homeostasis and/or their toxic effects due to possible generation of oxidative stress under the widely different iron reductive mechanisms typical of eukaryotic cells.

## Transparency document

The Transparency document associated with this article can be found, in the online version.

## Acknowledgements

EU $H_{2020}$ Project "X-Probe", Grant N° 637295, to A. Bonamore and M.C.T. is gratefully acknowledged. Flagship project "Nanomax" from MIUR (Nanomax MIUR_J120062) to A. Boffi is also acknowledged.

## Appendix A. Supplementary data

Supplementary data to this article can be found online at doi:10.1016/j.bbagen.2016.10.007.

## References

[1] K. Honarmand Ebrahimi, P.L. Hagedoorn, W.R. Hagen, Unity in the biochemistry of the iron-storage proteins ferritin and bacterioferritin, Chem. Rev. 115 (2015) 295–326.
[2] Z. Zhen, W. Tang, H. Chen, X. Lin, T. Todd, G. Wang, RGD-modified apoferritin nanoparticles for efficient drug delivery to tumors, ACS Nano 7 (2013) 4830–4837.
[3] N. Pontillo, F. Pane, L. Messori, A. Amoresano, A. Merlino, Cisplatin encapsulation within a ferritin nanocage: a high-resolution crystallographic study, Chem. Commun. (Camb.) 52 (2016) 4136–4139.
[4] E. Falvo, E. Tremante, R. Fraioli, C. Leonetti, C. Zamparelli, A. Boffi, V. Morea, P. Ceci, P. Giacomini, Antibody-drug conjugates: targeting melanoma with cisplatin encapsulated in protein-cage nanoparticles based on human ferritin, Nanoscale 5 (2013) 12278–12285.
[5] X.-T. Ji, L. Huang, H.-Q. Huang, Construction of nanometer cisplatin core-ferritin (NCC-F) and proteomic analysis of gastric cancer cell apoptosis induced with cisplatin released from the NCC-F, J. Proteome 75 (2012) 3145–3157.
[6] J.M. Domínguez-Vera, Iron(III) complexation of desferrioxamine B encapsulated in apoferritin, J. Inorg. Biochem. 98 (2004) 469–472.
[7] A. Maham, Z. Tang, H. Wu, J. Wang, Y. Lin, Protein-based nanomedicine platforms for drug delivery, Small 5 (2009) 1706–1721.
[8] A. Maham, H. Wu, J. Wang, X. Kang, Y. Zhang, Y. Lin, Apoferritin-based nanomedicine platform for drug delivery: equilibrium binding study of daunomycin with DNA, J. Mater. Chem. 21 (2011) 8700–8708.
[9] L. Vannucci, E. Falvo, C.M. Failla, M. Carbo, M. Fornara, R. Canese, S. Cecchetti, L. Rajsiglova, D. Stakheev, J. Krizan, A. Boffi, G. Carpinelli, V. Morea, P. Ceci, In vivo targeting of cutaneous melanoma using a melanoma stimulating hormone-engineered human protein cage with fluorophore and magnetic resonance imaging tracers, J. Biomed. Nanotechnol. 11 (2015) 81–92.
[10] X. Yang, P. Arosio, N.D. Chasteen, Molecular diffusion into ferritin: pathways, temperature dependence, incubation time, and concentration effects, Biophys. J. 78 (2000) 2049–2059.
[11] X. Yang, N.D. Chasteen, Molecular diffusion into horse spleen ferritin: a nitroxide radical spin probe study, Biophys. J. 71 (1996) 1587–1595.
[12] B. Zhang, R.K. Watt, N. Gálvez, J.M. Domínguez-Vera, G.D. Watt, Rate of iron transfer through the horse spleen ferritin shell determined by the rate of formation of prussian blue and Fe-desferrioxamine within the ferritin cavity, Biophys. Chem. 120 (2006) 96–105.
[13] R.R. Crichton, J.P. Declercq, X-ray structures of ferritins and related proteins, Biochim. Biophys. Acta 1800 (2010) 760–818.
[14] T. Douglas, D.R. Ripoll, Calculated electrostatic gradients in recombinant H-chain ferritin, Protein Sci. 7 (5) (1998 May) 1083–1091.
[15] P.M. Harrison, A. Treffry, T.H. Lilley, Ferritin as an iron-storage protein: mechanisms of iron uptake, J. Inorg. Biochem. 27 (1986) 287–293.
[16] A. Treffry, P.M. Harrison, Spectroscopic studies on the binding of iron, terbium, and zinc by apoferritin, J. Inorg. Biochem. 21 (1984) 9–20.
[17] E. Johnson, D. Cascio, M.R. Sawaya, M. Gingery, I. Schröder, Crystal structures of a tetrahedral open pore ferritin from the hyperthermophilic archaeon *Archaeoglobus fulgidus*, Structure 13 (2005) 637–648.
[18] B. Sana, E. Johnson, P. Le Magueres, A. Criswell, D. Cascio, S. Lim, The role of nonconserved residues of *Archaeoglobus fulgidus* ferritin on its unique structure and biophysical properties, J. Biol. Chem. 288 (2013) 32663–32672.
[19] P.W. Riddles, R.L. Blakeley, B. Zerner, Ellman's reagent: 5,5′-dithiobis(2-nitrobenzoic acid) —a reexamination, Anal. Biochem. 94 (1979) 75–81.
[20] B.J. Berne, R. Pecora, Dynamic Light Scattering, Wiley, New York, 1976.
[21] M. Liang, K. Fan, M. Zhou, D. Duan, J. Zheng, D. Yang, J. Feng, X. Yan, H-ferritin-nanocaged doxorubicin nanoparticles specifically target and kill tumors with a single-dose injection, Proc. Natl. Acad. Sci. U. S. A. 111 (2014) 14900–14905.

[22] M.A. Kostiainen, P. Hiekkataipale, A. Laiho, V. Lemieux, J. Seitsonen, J. Ruokolainen, P. Ceci, Electrostatic assembly of binary nanoparticle superlattices using protein cages, Nat. Nanotechnol. 8 (2013) 52–56.
[23] A. Desideri, S. Stefanini, F. Polizio, R. Petruzzelli, E. Chiancone, Iron entry route in horse spleen apoferritin. Involvement of the three-fold channels as probed by selective reaction of cysteine-126 with the spin label 4-maleimido-tempo, FEBS Lett. 287 (1991) 10–14.
[24] J. Tatur, W.R. Hagen, P.M. Matias, Crystal structure of the ferritin from the hyperthermophilic archaeal anaerobe *Pyrococcus furiosus*, J. Biol. Inorg. Chem. 12 (2007) 615–630.
[25] E.F. Pettersen, T.D. Goddard, C.C. Huang, G.S. Couch, D.M. Greenblatt, E.C. Meng, T.E. Ferrin, UCSF chimera—a visualization system for exploratory research and analysis, J. Comput. Chem. 25 (2004) 1605–1612.
[26] R.K. Beheraa, E.C. Theil, Moving $Fe^{2+}$ from ferritin ion channels to catalytic OH centers depends on conserved protein cage carboxylates, Proc. Natl. Acad. Sci. U. S. A. 111 (2014) 7925–7930.

# APPENDIX II

Nanoscale

PAPER

# Humanized archaeal ferritin as a tool for cell targeted delivery†

Cite this: *Nanoscale*, 2017, **9**, 647

Valeria de Turris,[a] Matilde Cardoso Trabuco,[b] Giovanna Peruzzi,[a] Alberto Boffi,[a,c] Claudia Testi,[a] Beatrice Vallone,[c] Linda Celeste Montemiglio,[d] Amédée Des Georges,[e] Lorenzo Calisti,[d] Irene Benni,[d] Alessandra Bonamore[d] and Paola Baiocco*[a]

Received 8th September 2016,
Accepted 23rd November 2016

DOI: 10.1039/c6nr07129e

www.rsc.org/nanoscale

Human ferritins have been extensively studied to be used as nanocarriers for diverse applications and could represent a convenient alternative for targeted delivery of anticancer drugs and imaging agents. However, the most relevant limitation to their applications is the need for highly acidic experimental conditions during the initial steps of particle/cargo assembly, a process that could affect both drug stability and the complete reassembly of the ferritin cage. To overcome this issue the unique assembly of *Archaeoglobus fulgidus* ferritin was genetically engineered by changing a surface exposed loop of 12 amino acids connecting B and C helices to mimic the sequence of the analogous human H-chain ferritin loop. This new chimeric protein was shown to maintain the unique, cation linked, association–dissociation properties of *Archaeoglobus fulgidus* ferritin occurring at neutral pH values, while exhibiting the typical human H-homopolymer recognition by the transferrin receptor TfR1. The chimeric protein was confirmed to be actively and specifically internalized by HeLa cells, thus representing a unique nanotechnological tool for cell-targeted delivery of possible payloads for diagnostic or therapeutic purposes. Moreover, it was demonstrated that the 12 amino acids' loop is necessary and sufficient for binding to the transferrin receptor. The three-dimensional structure of the humanized *Archaeoglobus* ferritin has been obtained both as crystals by X-ray diffraction and in solution by cryo-EM.

## Introduction

Ferritin proteins have been extensively used as nanocarriers for diverse applications due to their hollow cage-like structures and their unique, reversible, 24-mer assembly.[1,2] In more detail, they represent the most convenient alternative to viral carriers for targeted delivery of anticancer drugs and imaging agents and have been successfully utilized as reaction nanovessels for the synthesis of non-native metallic nanoparticles in the inner core, with applications in nanoelectronic devices.[3–5] The external and internal surfaces of ferritin are chemically and genetically modifiable allowing for the attachment site for drugs, nucleic acids, fluorophores or magnetic moieties. Along this line, recent studies further established heavy (H) or light (L)-chain homopolymers as versatile multifunctional nanocarriers for targeted cancer diagnosis and therapy.[6–10] In fact, human ferritins constitute biocompatible nanocarriers that stabilize and shelter the enclosed particles, thus preventing immunogenic responses. Moreover, ferritins are naturally targeted toward ubiquitously expressed TfR1 transferrin receptors (H-chain specific) or hepatic SCARA 5 receptors (L-chain specific). Such properties have been widely exploited for the efficient delivery of antitumor drugs to iron-avid, fast replicating, tumor cells overexpressing the TfR1 receptor.[11] Thus, ferritin based protein cages have been developed as versatile platforms for multiple applications in nanomedicine.

Current development of human ferritin based particle is however facing intrinsic limitations due to the experimental conditions linked to their assembly–disassembly equilibrium, whose control is a prerequisite in order to achieve encapsulation of the cargo within the internal cavity. In the conventional *in vitro* encapsulation procedures, ferritin must be disassembled at extreme pH values (pH = 2.0) and re-assembled in the presence of highly concentrated payload compounds.[12]

[a]*Center for Life Nano Science@Sapienza, Istituto Italiano di Tecnologia, V.le Regina Elena 291, Rome 00161, Italy. E-mail: paola.baiocco@iit.it*
[b]*Molirom srl, via Ravenna 8, 00161 Rome, Italy*
[c]*Institute of Molecular Biology and Pathology, National Research Council, P.le A. Moro, 7, 00185, Rome, Italy*
[d]*Department of Biochemical Sciences "Alessandro Rossi Fanelli", Sapienza University of Rome, P.le A. Moro, 5, 00185, Rome, Italy*
[e]*The City University of New York Advanced Science Research Center 85 St. Nicholas Terrace, New York, NY 10031, USA*
†Electronic supplementary information (ESI) available. See DOI: 10.1039/c6nr07129e

Such a procedure leads to a suboptimal load of cargo material, whose chemical structure is required to be pH resistant. Moreover, the pH jump procedure is only partially reversible and re-assembly may not be complete, depending on complex equilibrium and kinetic parameters.[13] Currently, extensive research efforts are devoted to adjust the assembly properties of ferritin nanocages to the desired applications either by intersubunit interface mutagenesis[14] or by genetic engineering of N- or C-terminal regions.[15]

Recently, novel ferritins from lower eukaryotes, bacteria and archaea, endowed with different polymer association–dissociation thermodynamic and kinetic features have emerged as possible alternatives to human ferritin homopolymers for several biotechnological applications requiring cargo material encapsulation.[16,17] Despite low sequence similarity, these ferritins display a highly conserved quaternary structure consisting of a four-helix bundle namely A, B, C and D and a short E helix at the C-terminus. Helices B and C are connected by a 12 amino acid (aa) long loop involved in stabilizing interactions at the 2-fold dimer interface. Unlike most eukaryotic and prokaryotic ferritins, the archaeal ferritin from *Archaeoglobus fulgidus* (AfFt) is characterized by unique self-assembly properties. In fact, in neutral buffers it is present as dimeric species, easily combining into a non-canonical 24-mer cage in the presence of metal cations.[18] AfFt assembles in a distinctive tetrahedral geometry as a result of particular packing between four hexametric units into a 24-mer structure different from those observed so far. Such unusual assembly results in the formation of four wide triangular pores (45 Å) on the protein shell.[19] As demonstrated by Sana *et al.*,[19] amino acid substitutions in the turn motif that connects D and E helices forming the 4-fold iron channels, namely K150A and R151A, are sufficient to restore the canonical octahedral symmetry observed in vertebrate and bacterial ferritins,[18,19] thus providing a rationale for the atypical tetrahedral architecture of AfFt. Nevertheless, the low sequence similarity of AfFt with mammalian ferritins runs against the possibility of targeting AfFt onto the TfR1 receptors in mammalian cells.

Transferrin receptor TfR1, or CD71, has been reported to be a preferred target for human ferritin, due to the specific interaction of the receptor extracellular moiety with epitopes of the H-ferritin subunit.[20,21] Inspection of the three-dimensional structure of the human H-homopolymer external surface indicates that the most significant accessible area is occupied by the external 12 aa long loop connecting B and C helices (up to 19 aa including the turn regions). Patches of a lesser extent exposed to solvent are formed by the N-terminal regions or by the iron channels within the threefold axis of the intersubunit assembly. However, it has been shown that N-terminal or C-terminal deleted human H-homopolymers are efficiently taken up by target cells, thus suggesting these regions are not required for receptor recognition or uptake.[22] Therefore the BC loop, besides its structural role in stabilization of the interdimer interface,[23] appeared to be the best candidate for TfR1 receptor recognition of the ferritin molecule.

We decided then to engineer the archaeal ferritin to devise a chimeric construct, named humanized *Archaeoglobus* ferritin (HumAfFt), in which the external 12 aa loop connecting the B and C helices was mutated to reproduce an analogous one in the corresponding region of the human H chain homopolymer (HuHF). It was observed that this chimeric protein (HumAfFt) was actively internalized by HeLa cells to an extent comparable to transferrin, the preferred ligand for TfR1.

## Results and discussion

### "Humanized" *Archaeoglobus* ferritin design

Heavy chain human ferritin and *Archaeoglobus* ferritin display 31% sequence identity. The structural alignment of HuHF and AfFt monomers (pdb code 3AJO and 1S3Q, respectively) reveals a shorter N-terminus and shorter loops between three of the four helices, with the notable exception of the long loop connecting B and C helices.

As shown in Fig. 1, the BC loops of two adjacent subunits run in an antiparallel fashion establishing significant, mutual interactions. Thus the BC loops of adjacent subunits display the same overall geometry in both HuHF and AfFt, though each couple of loops adopts a different symmetry along the spherical surface of the protein cage, given the different dimer–dimer positioning within each complete 24-mer structure.

In order to preserve the unique assembly properties of AfFt, while implementing a potential cellular uptake, we decided to exploit this external loop by mutating 9 residues into the corresponding residues found in HuHF, according to the sequence alignment shown in Fig. 2. In particular, the nine amino acids sequence IFLQDIKKP, typical of a human H ferritin homopolymer, located at the center of the 12 aa loop was inserted in place of VKLYAVEEP (from residue 70 to 79 in AfFt numbering, see Fig. 2). In addition, a cysteine residue in position 54 (AfFt numbering) has been introduced by point mutation in order to provide a conjugation site of potential thiol reactive derivatives into the cavity. As previously mentioned, we will refer to the chimeric protein described above as humanized *Archaeoglobus* ferritin (HumAfFt).

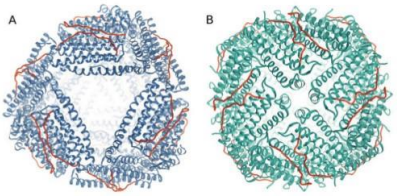


**Fig. 1** Three-dimensional structures determined by X-ray crystallography. A cartoon representation of (A) HumAfFt and (B) HuHF (pdb code 3AJO). Models are coloured in blue and green, respectively, and the external loop connecting the helices B and C of each monomer is shown as red ribbons. Molecular graphics were performed using a UCSF Chimera package.[35]

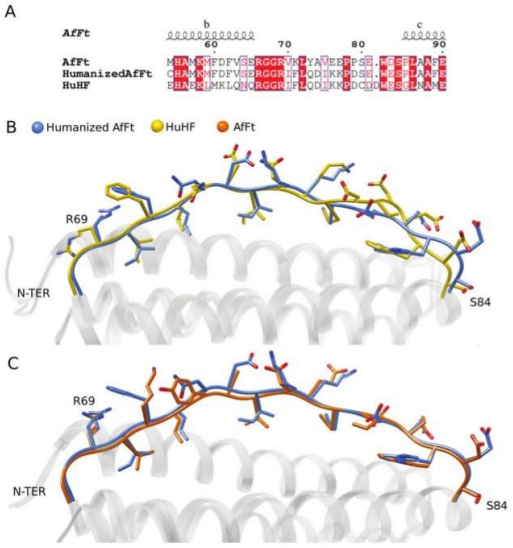


Fig. 2 Structure-based sequence alignment of AfFt, HumAfFt, and HuHF. (A) Close-up view of the sequence alignment. Elements of secondary structure for the AfFt are shown on the top. White characters in a red background indicate strict conservation while residues with poor conservation are drawn in black on a white background. Alignments were made using CLUSTAL Omega, and the figure was generated using ENDSCRIPT.[37] The structural superposition of the region from R69 and S84 (AfFt numbering) is shown in (B) HumAfFt (in blue) *vs.* HuHF (in yellow) and in (C) HumAfFt (in blue) *vs.* AfFt (in orange). Residues are depicted as sticks indicating N atoms in blue, O atoms in red and S atoms in yellow.

### Self-assembly assessment

The effect of mutations on the $MgCl_2$-mediated self-assembly of HumAfFt was studied by size exclusion chromatography (SEC), in order to separate different possible oligomers according to their molecular size. Identical peak-positions confirmed that HumAfFt retains the $MgCl_2$-mediated self-assembly properties of native AfFt[24] (see Fig. S2†). As shown in the chromatograms, the increasing of $MgCl_2$ concentration triggered the self-assembly of dimers until they reached a stable polymeric structure around 500 kDa, roughly corresponding to the expected 24-mer cage-like structure, at 20 mM $MgCl_2$. The data highlighted that the chimeric HumAfFt maintained the cation induced association/dissociation properties of archaeal ferritin and is possibly assembled into a 24-mer typical structure.[24]

### X-ray diffraction data on HumAfFt show the tetrahedral symmetry of archaeal ferritins

The humanized AfFt crystallized under different conditions with respect to wild type AfFt. Crystals were exposed to the synchrotron light in order to confirm the tetrahedral symmetry reported for archaeal ferritins. The protein was crystallized in the presence of $Mg^{2+}$ in order to maintain the 24-mer assembly.

The structure of HumAfFt has been determined by X-ray crystallography at a 2.87 Å resolution. It crystallized in the $C222_1$ space group, as also observed for wild type AfFt. The asymmetric unit (ASU) contains 12 identical subunits with a solvent content of 64.3%. The overall folding corresponded to the wild type structure (pdb code 1S3Q) with a rmsd value of 0.4 Å and displayed four wide triangular pores on the surface (Fig. 1A). B factor analysis shows a mean B factor of 66 $Å^2$ with the exception of the loop region between the D and E helices, which displays higher B factors and a poor electron density on the side chains from 146 to 151 residues. Conversely, the BC loop is well organized and the analysis of the difference electron density (Fo–Fc) map clearly showed the presence of the mutated residues in the loop between the helices B and C as well as the M54C mutation, pointing towards the inner cavity.

Two magnesium ions have been positioned and successfully refined in the ASU, and they are located in the ferroxidasic site of two different subunits. In both, one magnesium

ion is coordinated with both OE1 and OE2 of Glu19, (at 2.5 Å and 2.8 Å distance, respectively), with Glu52 (OE1) at 2.5 Å, with Gln129 (OE1) at 2.6 Å and with a water molecule at 2.6 Å distance. In the other chains, a water molecule has been modelled in the Fo–Fc map and successfully refined in the same position.

The loop region, including the conserved terminal turns, spans from amino acid 68 to amino acid 86. The sequence alignment and the structural superposition between HumAfFt and the human H-homopolymer, as well as between HumAfFt and AfFt, are shown in Fig. 2B and C. At the dimeric interface between the two antiparallel BC loops, the main interactions are a hydrogen bond between Arg69(NH2) and Ser80 (O) at 2.8 Å distance and two salt bridges, namely Lys71 (NZ)–Glu77 (OE1) at 3.0 Å distance and Glu81 (OE2)–Arg69 (NH1) at 2.7 Å distance. A weak salt bridge is established by Glu81 (OE2) and Arg69 (NH2), at a distance of 3.0 Å. The salt bridge between Lys71 and Glu77 observed in HuHF, is absent in HumAfFt since these positions were mutated into a phenylalanine (Phe71) and a lysine (Lys77). Other interactions are conserved between HuHF and HumAfFt and measured the same distances.

### Cryo-electron microscopy confirms the canonical AfFt architecture in solution

Humanized AfFt samples were prepared in thin ice layer and analyzed by cryo-EM in order to assess the three-dimensional structure of the chimeric protein in a near-native environment. Particles were picked with a reference-based automated particle picking procedure. Single ferritin particles were visualized at a nominal resolution of 33 Å demonstrating that their shape and dimensions correspond to that of wild type AfFt in its 24-mer assembly (Fig. 3A). Moreover, the triangular apertures on the protein surface were clearly observable in a bi-dimensional view (Fig. 3B) and better displayed in a three-dimensional reconstruction as shown in Fig. 3C.

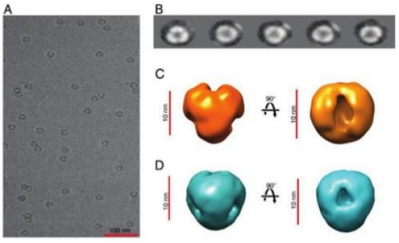


**Fig. 3** Electron microscopy characterization of humanized *Archaeoglobus fulgidus* ferritin. (A) Sample micrograph of the HumAfFt data set. Scale bar: 100 nm. (B) Five representative 2D class averages obtained with RELION. (C) 3D reconstruction of HumAfFt obtained with RELION and visualized with UCSF Chimera.[35] Map final resolution: 33.1 Å. Scale bars: 10 nm. Left: side view. Right: top view. (D) *Archaeoglobus fulgidus* ferritin crystal structure (from 16) filtered to 30 Å, shown for comparison. Scale bars: 10 nm. Left: side view. Right: top view.

### Flow cytometry analysis shows HumAfFt cellular uptake

After we have demonstrated that our HumAfFt maintained its structure with large open pores and the self-assembly property characteristic of the original AfFt, we aimed to verify that the modified version also gained access to eukaryotic cancer cells such as HeLa cells. It is known that HuHF is recognized and internalized by the TfR1, which is overexpressed in many types of tumor cells but not in normal cells and healthy tissues.[21] To validate the effect of our mutations on the external loop related to the uptake efficiency by HeLa cells, we performed time course experiments on cells treated with the same amount (30 μg $ml^{-1}$) of AfFt-FITC, HumAfFt-FITC and transferrin-FITC (TF-FITC) and analyzed them by flow cytometry. As a baseline for FITC fluorescence, control cells not incubated with FITC-ferritins were used. Moreover, to exclude any signal generated from outside particles sticking on the cell membrane due to unspecific binding or remains from the washing steps, trypan blue quenching was performed before using FACS. In Fig. 4, the FACS analysis is summarized, shown as the percentage of cells internalizing the nanoparticles at different times. These data highlighted that HumAfFt nanoparticles are efficiently taken up by HeLa cells already after one hour incubation with a much higher percentage compared to AfFt (81% and 5% respectively). After a

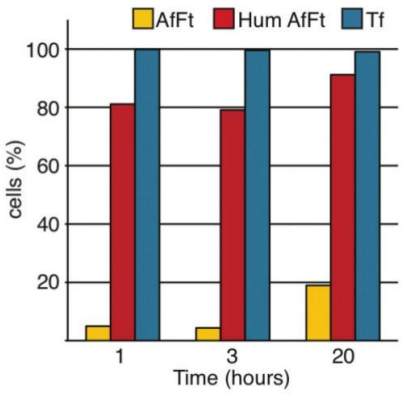


**Fig. 4** Humanized AfFt is internalized with higher efficiency than the original ferritin. Ferritins taken up in HeLa cells have been quantified by flow cytometry. Cells have been treated with 30 μg $ml^{-1}$ of AfFt-FITC, HumAfFt-FITC and transferrin-FITC (Tf). The percentage of cells internalizing the nanoparticles at the time indicated is shown. For each sample 30 000 events gated on live cells have been acquired.

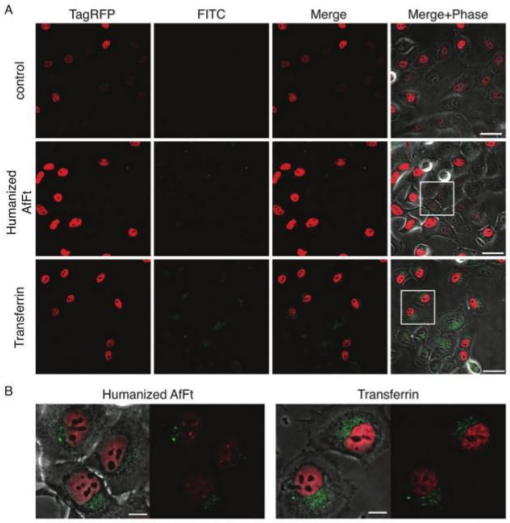


**Fig. 5** Ferritin internalization observed at the confocal microscope. Cells were plated on an 8-well μ-slide (ibidi), induced with doxycycline to express TagRFP and then incubated with 30 μg $ml^{-1}$ of humanized AfFt-FITC or transferrin-FITC for 20 h. After washing, cells were live-imaged using a confocal microscope. (A) Confocal images of live HeLa TagRFP cells are shown as single, merged channels and overlay images with the phase contrast. Scale bars: 40 μm. (B) Images are a magnified view of the region highlighted by the white inset in panel A; merged channels and the overlay with the phase contrast images are shown. Scale bars: 10 μm.

longer incubation time (20 hours), the FITC-positive cells for the humanized samples are increased to more than 90% whereas for native AfFt they are still less than 20%. The latter increment is possibly due to the unspecific uptake by pinocytosis. Each acquired plot is shown in Fig. S4.†

Moreover we performed the RNAi experiment against the transferrin receptor and analyzed the cellular uptake by FACS (Fig. S5†) obtaining around 50% HumAfFt uptake reduction after 48 hours of siRNA transfection, confirming the involvement of TfR1 in the internalization process.

### Visualization of ferritin nanoparticles inside living cells by confocal microscopy

In order to visualize uptaken HumAfFt–FITC nanocages, we performed the internalization assay directly on an ibidi 8-well μ-slide and incubated the cells for 20 hours before confocal microscopy. We exploited the properties of the HeLa TagRFP cell lines available in the lab in order to have a reference fluorescence signal confirming that we were imaging inside the cell. This cell line contains a TagRFP-FUS protein under the control of a doxycycline-inducible promoter that allows for a controlled expression of the protein and hence permits visualization of the nucleus in the red channel. In this case the cells were not selected to eliminate the untransfected cells, allowing us to visualize different levels of expression and also unstained nuclei. Just before imaging, the cells were washed to eliminate the unbound FITC-nanoparticles and then acquired by confocal laser-scanning microscopy. Confocal representative images of the entire field of view of live HeLa TagRFP cells alone (control) or incubated with HumAfFt-FITC or TF-FITC are shown in Fig. 5A. A detailed view of the boxed region in panel A is shown in Fig. 5B. Images confirmed the high extent of HumAfFt internalization and highlight a cellular distribution in the cytoplasm and in the perinuclear space comparable to that observed in the case of transferrin, thus suggesting a typical clathrin-coated endocytosis pathway, mediated by TfR1.

## Conclusion

The present data highlight the remarkable properties of a novel chimeric ferritin nanocage suitable for the design of efficient and versatile scaffolds for the intracellular delivery of bioactive small molecules and/or diagnostic probes.

*Archaeoglobus fulgidus* ferritin (AfFt) is a prominent example of this versatility due to its unique association/dissociation properties that lead to the presence of stable dimeric species at neutral pH and low ionic strength capable of associating into non-classical 24-mer species in the presence of either monovalent or divalent cations at physiological concentrations (*i.e.* higher than 0.5 M $Na^{+}$ or 20 mM $Mg^{++}$). Moreover, AfFt also displays a unique subunit assembly, based on tetrahedral symmetry, which leads to the formation of four large openings in the protein shell. As such, AfFt represents a uniquely suitable scaffold for incorporating a wealth of diverse substructures inside the protein cavity, either by an assembly/disassembly process at neutral pH or by diffusion through the large triangular pores on the surface. Notable examples have been reported in recent literature.[17] Nevertheless, one of the key properties of ferritin nanocages in biomedical applications is the possibility of targeting receptors on human cells, thus allowing the delivery of the desired payload within the cytoplasm. The engineered HumAfFt described here combines the versatility in assembly and cargo incorporation of AfFt by binding to TfR1 and by cellular uptake of HuHF. At present, further experiments with possible payloads for diagnostic or therapeutic applications are under development. However, *in vivo* applications will have to wait for the evaluation of possible immunological responses against non-human epitopes present on the protein surface. In fact, though the mutated loops appear to account for most of the solvent exposed surface, N-terminal and pore lining regions might still offer windows for non-self-recognition by the immune system.

## Materials and methods

### "Humanized" *Archaeoglobus* ferritin design

The gene encoding for a mutated ferritin from *Archaeoglobus fulgidus* was synthesised by GeneArt (ThermoFisher) and subcloned into a pET22b vector (Novagen) between the restriction sites NdeI and HindIII at 5′ and 3′ respectively. The recombinant plasmid was transformed into BL21(DE3) *E. coli* strain for protein expression.

### Protein expression and purification

*E. coli* cells, containing the HumAfFt plasmid, were grown and induced with 1 mM IPTG (isopropyl-β-D-1-thiogalactopyranoside) at $OD_{600}$ = 0.6. Cells were harvested by centrifugation 3 hours post induction at 37 °C.

Cells harvested from 1 L culture were resuspended in 20 mM HEPES buffer, pH 7.5, containing 200 mM NaCl, 1 mM TCEP (tris(2-carboxiethyl)phosphine), and a cOmplete™ Mini Protease Inhibitor Cocktail Tablet (Roche). Cells were disrupted by sonication and the soluble fraction was purified by heat treatment at 78 °C for 10 minutes. Denatured *E. coli* proteins were removed by centrifugation at 15 000 rpm at 4 °C for 1 hour. The soluble protein was further purified by ammonium sulfate precipitation. The precipitated fraction at 70% ammonium sulfate was resuspended in 20 mM HEPES, 50 mM $MgCl_2$, pH 7.5 and dialyzed *versus* the same buffer. As a final purification step, the protein was loaded onto a HiLoad 26/600 Superdex 200 pg column previously equilibrated in the same buffer using an ÄKTA-Prime system (GE Healthcare). The purified protein was concentrated to obtain the final protein preparation of 1 mg $mL^{-1}$ and protein concentration was calculated by measuring the UV spectrum using an extinction coefficient of 32 400 $M^{-1}$ $cm^{-1}$. Protein yield was ∼40 mg $L^{-1}$ culture.

### Self-assembly assessment in solution

Size exclusion chromatography $MgCl_2$-mediated self-assembly was studied by size exclusion chromatography (SEC) using a Superdex 200 26/600 GL column (GE Healthcare). The molecular size of HumAfFt was determined under different conditions by comparing the elution volume with that of standard proteins. Composition of the mobile phase was 25 mM HEPES pH = 7.5 with different $MgCl_2$ concentrations accordingly to the composition of the protein buffer.

### Crystallization and crystal structure determination

The purified protein was concentrated to 20 mg $mL^{-1}$ and initial crystallization screening was performed using a Phenix Robot. Crystals were obtained by mixing in a 2 μL hanging drop 1 mM of the purified protein with a solution containing 22% (vol/vol) polyacrylic acid PAA, 0.1 M Tris, 0.02 M $MgCl_2$, pH 7.4, at 25 °C within a week, cryo-protected by increasing the precipitant concentration and flash-frozen in liquid nitrogen. Diffraction data have been collected at ID23-2 beamline at the European Synchrotron Radiation Facility (ESRF), Grenoble, France.

Data were processed with XDS[25] and scaled with Aimless (ccp4 suite) at a final resolution of 2.87 Å. The structure was solved by Molecular Replacement with MolRep (ccp4 suite) using the open pore structure AfFt (pdb code 1S3Q) as the search model. Model Building and refinement were done using Coot[26] and Refmac5, respectively. The final model was analyzed with PROCHECK[27] and Molprobity.[28] The Ramachandran plot showed that 97.8% of residues are in preferred regions, 2.2% in allowed regions and no outlier is observed. The final atomic coordinates and structure factors were deposited with the PDB Data Bank (http://www.rcsb.org) with accession code: 5LS9. Complete data collection and refinement statistics are reported in Table S1.†

### Cryo-Electron microscopy

Holey-gold grids were prepared as described by Russo and Passmore[29] from Quantifoil R1.2/1.3 (Quantifoil Micro Tools GmbH, Germany). 3 μL of HumAfFt (12 μM) was applied to the holey-gold grids after plasma cleaning with a mixture of $H_2$ and $O_2$. Grids were blotted for 4 seconds and vitrified by rapidly plunging into liquid ethane at −180 °C (ref. 30 and 31) with a Vitrobot (FEI).

Data acquisition was done using a FEI Titan Halo (FEI, Eindhoven) operating at 300 kV. Datasets were imaged with a Volta phase-plate (FEI, Eindhoven)[32] and were collected with

 

the automated data collection system EPU (FEI, Eindhoven) at a nominal magnification of 59 000× on an FEI Ceta camera (FEI, Eindhoven) with a camera pixel size of 14 μm, corresponding to a calibrated pixel size of 1.49 Å on the specimen scale and with a dose of 50 $e^{-}$ $Å^{-2}$.

**Image processing.** The particles were picked with the reference-based automated particle picking procedure implemented in RELION 1.3.[33,34] CTF correction was not applied since the data were collected within 200 nm of focus and the first CTF zero crossing was well beyond the achievable resolution of the dataset. Those particles were subjected to 2D classification using RELION with $k$ = 100 classes. Good particles were then subjected to 3D classification using RELION with the number of classes $K$ = 8. Resulting classes were refined with the autorefine procedure in RELION.

**Resolution estimation.** Reported resolutions are based on the 'gold-standard' protocol with the FSC = 0.143 criterion using soft masks with an 8 pixel soft edge, and were corrected for the effects of the mask on the FSC curve using high-resolution noise substitution.[34]

Maps were visualized using UCSF Chimera.[35]

### Cell line generation

The HeLa cell line stably expressing an inducible TagRFP-FUS protein (HeLaTagRFP) was generated by transfection with epB-Puro-TT-RFP-FUS wt plasmid and the piggyBac transposase vector. Plasmid construction is described in ref. 36.

### Protein FITC labeling

HumAfFt, AfFt and Olo-transferrin were labeled with fluorescein-isothiocyanide (FITC, ThermoFisher) according to the manufacturer's standard protocol. Briefly, 2 mg $mL^{-1}$ of the purified protein was added with 10-fold molar excess of in protein storage buffer stirring for 2 hours at RT. The non-reacted dye was removed by gel filtration chromatography and the fluorescent dye to protein ratio was determined by UV-spectroscopy. LC-MS spectrometry measurements on HumAfFt-FITC confirmed that >60% of monomers are FITC labeled as reported in Fig. S6.†

### Cell cultures and ferritin internalization

HeLa cells were grown at 37 °C in Eagle's MEM supplemented with 10% (v/v) FBS, Glutamax (Invitrogen) and penicillin–streptomycin solution (Sigma). When needed, the cells were induced with doxycycline 0.2 μg $mL^{-1}$. The internalization assay was performed as follows: after seeding the cells on the relevant substrate depending on the experiment, cells were left one day to attach and then incubated with FITC-ferritin nanoparticles (AfFt-FITC, HumAfFt-FITC or Tf-FITC as specified in each experiment) at the final concentration of 30 μg $ml^{-1}$ for the time indicated (1 h, 3 h or 20 h).

### Flow cytometry analysis

For flow cytometry analysis HeLa cells were seeded on multi-well plates. Cells were incubated with FITC-ferritin nanoparticles as described previously, then washed two times with PBS, detached with trypsin-EDTA (Euroclone), washed with PBS and resuspended in BD-FACS flow buffer. Half of each sample was treated with Trypan Blue (TB; Sigma) to quench the FITC signal from membrane-bound nanoparticles that were not internalized. The quenching was performed with 0.04% TB for 10 min on ice. Control cells were treated in the same way but without FITC-ferritin incubation. Internalization of ferritins before and after TB treatments was measured at the BD LSFORTESSA (BD Biosciences, San Jose, CA, USA) equipped with a 488 nm laser and FACSDiva software (BD Biosciences version 6.1.3). Live cells were first gated by forward and side scatter area (FSC-A and SSC-A) plots, then detected in the green channel for FITC expression (530/30 nm filter) and side scatter parameter. The gate for the final detection was set in the control sample. Data were analyzed using FlowJo9.3.4 software (Tree Star, Ashland, OR, USA).

### Confocal microscopy of live cells

To visualize ferritin internalization by live cells using a confocal microscope, HeLa TagRFP cells were seeded on a μ-slide 8-well ibiTreat (ibidi) and induced with 0.2 μg $mL^{-1}$ of doxycycline. Cells were then incubated with FITC-ferritin nanoparticles as previously described for 20 h and, before microscopy, cells were washed two times with an imaging medium (DMEM without phenol red, 10% FBS, 10 mM Hepes, Glutamax and penicillin–streptomycin solution) to eliminate the unbound FITC-nanoparticles. The confocal laser-scanning microscope used was an Olympus FV10i platform equipped with a built-in incubator. Images were acquired with a 60×/1.2NA water-immersion objective, LD lasers, 473 nm and 559 nm, and filter sets for FITC and TRITC. Phase-contrast images were acquired simultaneously.

## Acknowledgements

We thank Alessandro Rosa and Riccardo De Santis for the HeLa TagRFP cell line. EU $H_{2020}$ Project "X-Probe", Grant No. 637295, to A. B. and M. C. T. is gratefully acknowledged. Flagship Project "Nanomax" to A. B. is acknowledged. Regional project FILAS to B. V. is also acknowledged.

## References

1 E. C. Theil, Ferritin protein nanocages use ion channels, catalytic sites, and nucleation channels to manage iron/oxygen chemistry, *Curr. Opin. Chem. Biol.*, 2011, **15**, 304–311.

2 L. Schoonen and J. C. van Hest, Functionalization of protein-based nanocages for drug delivery applications, *Nanoscale*, 2014, **6**, 7124–7141.

3 A. Prastaro, P. Ceci, E. Chiancone, A. Boffi, G. Fabrizi and S. Cacchi, Homocoupling of arylboronic acids and potassium aryltrifluoroborates catalyzed by protein-stabilized

palladium nanoparticles under air in water, *Tetrahedron Lett.*, 2010, **51**, 2550.
4 F. Meng, B. Sana, Y. Li, Y. Liu, S. Lim and X. Chen, Bioengineered tunable memristor based on protein nanocage, *Small*, 2014, **10**, 277–283.
5 M. A. Kostiainen, P. Hiekkataipale, A. Laiho, V. Lemieux, J. Seitsonen, J. Ruokolainen and P. Ceci, Electrostatic assembly of binary nanoparticle superlattices using protein cages, *Nat. Nanotechnol.*, 2013, **8**, 52–56.
6 M. Liang, K. Fan, M. Zhou, D. Duan, J. Zheng, D. Yang, J. Feng and X. Yan, H-ferritin-nanocaged doxorubicin nanoparticles specifically target and kill tumors with a single-dose injection, *Proc. Natl. Acad. Sci. U. S. A.*, 2014, **111**, 14900–14905.
7 L. Vannucci, E. Falvo, C. M. Failla, M. Carbo, M. Fornara, R. Canese, S. Cecchetti, L. Rajsiglova, D. Stakheev, J. Krizan, A. Boffi, G. Carpinelli, V. Morea and P. Ceci, In Vivo Targeting of Cutaneous Melanoma Using an Melanoma Stimulating Hormone-Engineered Human Protein Cage with Fluorophore and Magnetic Resonance Imaging Tracers, *J. Biomed. Nanotechnol.*, 2015, **11**, 81–92.
8 E. Falvo, E. Tremante, R. Fraioli, C. Leonetti, C. Zamparelli, A. Boffi, V. Morea, P. Ceci and P. Giacomini, Antibody-drug conjugates: targeting melanoma with cisplatin encapsulated in protein-cage nanoparticles based on human ferritin, *Nanoscale*, 2013, **5**, 12278–12285.
9 L. Vannucci, E. Falvo, M. Fornara, P. Di Micco, O. Benada, J. Krizan, J. Svoboda, K. Hulikova-Capkova, V. Morea, A. Boffi and P. Ceci, Selective targeting of melanoma by PEG-masked protein-based multifunctional nanoparticles, *Int. J. Nanomed.*, 2012, **7**, 1489–1509.
10 S. Geninatti Crich, M. Cadenazzi, S. Lanzardo, L. Conti, R. Ruiu, D. Alberti, F. Cavallo, J. C. Cutrin and S. Aime, Targeting ferritin receptors for the selective delivery of imaging and therapeutic agents to breast cancer cells, *Nanoscale*, 2015, **7**, 6527–6533.
11 K. Fan, C. Cao, Y. Pan, D. Lu, D. Yang, J. Feng, L. Song, M. Liang and X. Yan, Magnetoferritin nanoparticles for targeting and visualizing tumour tissues, *Nat. Nanotechnol.*, 2012, **7**, 459–464.
12 Z. Zhen, W. Tang, T. Todd and J. Xie, Ferritins as nanoplatforms for imaging and drug delivery, *Expert Opin. Drug Delivery*, 2014, **11**, 1913–1922.
13 K. Mihee, R. Yecheol, S. J. Kyeong, A. Byungcheol, J. Sungmin, K. Heesoo and R. Moonhor, pH-dependent structures of ferritin and apoferritin in solution: disassembly and reassembly, *Biomacromolecules*, 2011, **12**, 1629–1640.
14 H. Chen, S. Zhang, C. Xu and G. Zhao, Engineering protein interfaces yields ferritin disassembly and reassembly under benign experimental conditions, *Chem. Commun.*, 2016, **52**, 7402–7405.
15 S. Kim, J. O. Jeon, E. Jun, J. Jee, H. K. Jung, B. H. Lee, I. S. Kim and S. Kim, Designing Peptide Bunches on Nanocage for Bispecific or Superaffinity Targeting, *Biomacromolecules*, 2016, **17**, 1150–1159.
16 A. M. Sevcenco, M. Paravidino, J. S. Vrouwenvelder, H. T. Wolterbeek, M. C. van Loosdrecht and W. R. Hagen, Phosphate and arsenate removal efficiency by thermostable ferritinenzyme from Pyrococcus furiosus using radioisotopes, *Water Res.*, 2015, **76**, 181–186.
17 B. Sana, E. Johnson and S. Lim, The unique self-assembly/disassembly property of *Archaeoglobus fulgidus* ferritin and its implications on molecular release from the protein cage, *Biochim. Biophys. Acta*, 2015, **1850**, 2544–2551.
18 E. Johnson, D. Cascio, M. R. Sawaya, M. Gingery and I. Schröder, Crystal structures of a tetrahedral open pore ferritin from the hyperthermophilicarchaeon *Archaeoglobus fulgidus*, *Structure*, 2005, **13**, 637–648.
19 B. Sana, E. Johnson, P. Le Magueres, A. Criswell, D. Cascio and S. Lim, The role of nonconserved residues of *Archaeoglobus fulgidus* ferritin on its unique structure and biophysical properties, *J. Biol. Chem.*, 2013, **288**, 32663–32672.
20 Z. Heger, S. Skalickova, O. Zitka, V. Adam and R. Kizek, Apoferritin applications in nanomedicine, *Nanomedicine*, 2014, **9**, 2233–2245.
21 L. Li, C. J. Fang, J. C. Ryan, E. C. Niemi, J. A. Lebrón, P. J. Björkman, H. Arase, F. M. Torti, S. V. Torti, M. C. Nakamura and W. E. Seaman, Binding and uptake of H-ferritin are mediated by human transferrin receptor-1, *Proc. Natl. Acad. Sci. U. S. A.*, 2010, **107**, 3505–3510.
22 S. Levi, A. Luzzago, G. Cesareni, A. Cozzi, F. Franceschinelli, A. Albertini and P. Arosio, Mechanism of ferritin iron uptake: activity of the H-chain and deletion mapping of the ferro-oxidase site. A study of iron uptake and ferroxidase activity of human liver, recombinant H-chain ferritins, and of two H-chain deletion mutants, *J. Biol. Chem.*, 1988, **263**, 18086–18092.
23 C. Bernacchioni, V. Ghini, C. Pozzi, F. Di Pisa, E. C. Theil and P. Turano, Loop electrostatics modulates the intersubunit interactions in ferritin, *ACS Chem. Biol.*, 2014, **9**, 2517–2525.
24 L. Calisti, I. Benni, M. Cardoso Trabuco, P. Baiocco, B. Ruzicka, A. Boffi, E. Falvo, F. Malatesta and A. Bonamore, Probing bulky ligand entry in engineered archaeal ferritins, *Biochim. Biophys. Acta*, 2016, DOI: 10.1016, [Epub ahead of print].
25 W. Kabsch, Integration, scaling, space-group assignment and post-refinement, *Acta Crystallogr., Sect. D: Biol. Crystallogr.*, 2010, **66**, 133–144.
26 P. Emsley and K. Cowtan, Coot: model-building tools for molecular graphics, *Acta Crystallogr., Sect. D: Biol. Crystallogr.*, 2004, **60**, 2126–2132.
27 R. A. Laskowski, M. W. MacArthur, D. S. Moss and J. M. Thornton, PROCHECK - a program to check the stereochemical quality of protein structures, *J. Appl. Crystallogr.*, 1993, **26**, 283–29125.
28 V. B. Chen, W. B. Arendall 3rd, J. J. Headd, D. A. Keedy, R. M. Immormino, G. J. Kapral, L. W. Murray, J. S. Richardson and D. C. Richardson, MolProbity: all-atom structure validation for macromolecular crystallo-

 

graphy, *Acta Crystallogr., Sect. D: Biol. Crystallogr.*, 2010, **66**, 12–21.
29 C. J. Russo and L. A. Passmore, Ultrastable gold substrates for electron cryomicroscopy, *Science*, 2014, **346**, 1377–1380.
30 J. Dubochet, M. Adrian, J. J. Chang, J. C. Homo, J. Lepault, A. W. McDowall and P. Schultz, Cryo-electron microscopy of vitrified specimens, *Q. Rev. Biophys.*, 1988, **21**, 129–228.
31 T. Wagenknecht, R. Grassucci and J. Frank, Electron microscopy and computer image averaging of ice-embedded large ribosomal subunits from *Escherichia coli*, *J. Mol. Biol.*, 1988, **199**, 137–147.
32 R. Danev, B. Buijsse, M. Khoshouei, J. M. Plitzko and W. Baumeister, Volta potential phase plate for in-focus phase contrast transmission electron microscopy, *Proc. Natl. Acad. Sci. U. S. A.*, 2014, **111**, 15635–15640.
33 S. H. W. Scheres, Semi-automated selection of cryo-EM particles in RELION-1.3, *J. Struct. Biol.*, 2015, **189**, 114–122.
34 S. Chen, G. McMullan, A. R. Faruqi, G. N. Murshudov, J. M. Short, S. H. Scheres and R. Henderson, High-resolution noise substitution to measure overfitting and validate resolution in 3D structure determination by single particle electron cryomicroscopy, *Ultramicroscopy*, 2013, **135**, 24–35.
35 E. F. Pettersen, T. D. Goddard, C. C. Huang, G. S. Couch, D. M. Greenblatt and E. C. Meng, Ferrin TE. UCSF Chimera–a visualization system for exploratory research and analysis, *J. Comput. Chem.*, 2004, **25**, 1605–1612.
36 M. Morlando, S. Dini Modigliani, G. Torrelli, A. Rosa, V. Di Carlo, E. Caffarelli and I. Bozzoni, FUS stimulates microRNA biogenesis by facilitating co-transcriptional Drosha recruitment, *EMBO J.*, 2012, **31**, 4502.
37 X. Robert and P. Gouet, Deciphering key features in protein structures with the new ENDscript server, *Nucleic Acids Res.*, 2014, **42**, 320–324.

# APPENDIX III

# Engineered ferritin for lanthanide binding.

Lorenzo Calisti[a], Matilde Cardoso Trabuco[b], Alberto Boffi[c,d], Claudia Testi[a], Linda Celeste Montemiglio[a], Amédée des Georges[e], Irene Benni[a], Andrea Ilari[d], BartłomiejTaciak[f,g], MaciejBiałasek[f], Tomasz Rygiel[g,h], Magdalena Król[f,g], Paola Baiocco[c], Alessandra Bonamore[a].

[a.] Department of Biochemical Sciences "Alessandro Rossi Fanelli", Sapienza University of Rome, Rome Italy.

[b.] Molirom srl, via Ravenna 8, 00161, Rome, Italy.

[c.] Center for Life Nano Science@Sapienza, Istituto Italiano di Tecnologia, V.le Regina Elena 291, Rome 00161, Italy

[d.] Institute of Molecular Biology and Pathology, National Research Council, Rome, Italy.

[e.] The City University of New York Advanced Science Research Center 85 St. Nicholas Terrace, New York, NY 10031.

[f.] Faculty of Veterinary Medicine, Warsaw University of Life Sciences, ul. Nowoursynowska 166 02-787, Warszawa, Poland.

[g.] Cellis Ltd., Gen. Zajaczka 28, 01-510 Warsaw, Poland

[h] Department of Immunology, Center for Biostructure Research, Medical University of Warsaw, Banacha 1a, 02-089 Warsaw, Poland.

*Corresponding author: paola.baiocco@iit.it

Keywords: Protein cage; Ferritin; cellular uptake; Terbium binding, protein crystallography; cryo electron microscopy.

## Abstract

Mammalian ferritin H-homopolymers have been extensively studied to be used as nanocarriers for diverse applications in the targeted delivery of anticancer drugs and as imaging agents. In the present work, we have engineered a new construct in which a lanthanide binding tag (LBT) was genetically fused to the C-terminal end of mouse H ferritin, HFt. The HFt-LBT thus obtained possesses an extra Terbium binding site per subunit provided by six coordinating aminoacid side chains and a tryptophan residue in

its close proximity and is thus endowed with high Terbium ion affinity and strong FRET sensitization properties. The Terbium emission band at 544 nm for the HFt-LBT Tb(III) complex was detectable in the pM protein concentration range in solution, two order of magnitude higher with respect to control wild type mouse HFt. X-ray crystallography data at 2.9Å resolution and cryo-EM at 7 Å resolution demonstrated that HFt-LBT is correctly assembled as a 24-mer both in crystal and in solution. Tb(III) binding sites were identified in the protein threefold axes and in the ferroxidase sites for a total of about 56 Tb(III) atoms per 24-mer, comprising the 24 metal ions coordinated to the LBT. Moreover, HFt-LBT Tb(III) was demonstrated to be actively uptaken by selected tumor cell lines by confocal microscopy and FACS analysis of their FITC derivatives.

## 1. INTRODUCTION

Ferritin is a cage-like protein made of 24 subunits arranged in octahedral 432 symmetry with an outer diameter of roughly 12 nm and an inner diameter of 8 nm [1,2]. The symmetrical positioning of three or four subunits in the protein shell results in the formation of eight channels connecting the inner cavity to the outside and allows for the entry and exit of iron and other cations with a relatively broad selectivity [3]. Besides their physiological function, centered around intracellular iron uptake, the nanocage properties of ferritins have been exploited in a number of diverse biotechnological applications as drug delivery vectors [4], scaffolds for vaccine development [5] and tools for bioimaging [6]. In this context, ferritins have been proven particularly useful for the selective targeting to cell populations overexpressing the transferrin receptor (CD71), in particular iron avid tumor cells [7,8].

Among the many ingenious ferritin based constructs for bioimaging, only a few have been devoted to the creation of smart fluorescent probes and these include quantum dots [9] and gold nanoparticles [10, 11]. However, advanced optical imaging techniques need an expanded color palette of bright fluorescent probes for biological visualization in order to enable real-time cellular imaging with high spatial resolution for close up view into subcellular compartments and for providing key information on intracellular activities and macromolecular dynamics.

In this framework, fluorescent probes based on trivalent lanthanide ions are becoming widespread due to their unique photophysical properties [12-14]. Lanthanide f-orbitals with their high quantum yields are capable of efficiently radiating most of the absorbed energy, although their small absorption cross sections poses limits to their use. To improve the luminescent signals, small organic fluorophores that absorb in the UV region and transfer the absorbed light to the lanthanide atom are thus currently used in complex with the metal ion. Complexes of lanthanides are characterized by narrowband emission

spectra, large Stokes shift (150-300 nm), and excited state lifetimes within the range of micro to milliseconds. By exploiting the microsecond fluorescence of lanthanides, time-resolved spectroscopy allows for the elimination of the short living background signals whose lifetimes are usually not more than 10-15 ns and the enhancement of the sensitivity for recording the delayed signal [15]. Moreover, the inherently low extinction coefficient of lanthanide ions, due to the forbidden character of the electronic transitions, can be overcome by Förster resonance energy transfer (FRET) from an appropriately placed (within 5-6 Å distance) sensitizer-fluorophore onto the emitting level of the lanthanide, a phenomenon often referred to as "antenna effect" [16]. Among lanthanides, Tb(III) and Eu(III) are the most interesting due to their more intense microsecond fluorescence in the visible region [17, 18]. Among the various methods for the incorporation of lanthanide ions into biomolecules, a straightforward and generalizable approach has been proposed in recent years that integrates a lanthanide binding sequence as a protein co-expression tag via molecular biology strategies. On the basis of known properties of calcium binding loops, recent design and engineering studies have resulted in the development of short polypeptides comprising 20 or fewer encoded amino that are capable of tight and selective binding to lanthanides. These peptide sequences, identified as "lanthanide-binding tags" (LBT), show low-nanomolar affinities for the target ions and are selective for lanthanides over other common metal ions [19-22]. The probe nature of these protein tags has been demonstrated by their use for luminescence-based visualization on gels, as magnetic-field paramagnetic alignment agents in protein NMR experiments [23, 24] in fluorescence microscopy, [25, 26] and as partners in luminescence resonance energy transfer (LRET) studies [27].

Among the several proteins physiologically involved in metal binding that can be used for Terbium binding, ferritins may appear among the most suitable. In fact, native apoferritins have been reported to naturally bind Tb(III) within their iron binding sites [28]. In particular, it was demonstrated that mammalian apoferritins could bind more than one Tb(III) ion per subunit, corresponding respectively to ferroxidase site, threefold channel and nucleation centre [29, 30]. Moreover, upon excitation between 280-295 nm Tb(III) ferritin complex showed characteristic emission bands at 490 and 544 nm due to a FRET sensitization effect provided by aromatic aminoacids [30]. However, the distance between Terbium ions and aromatic moieties in native ferritin isoforms made the FRET efficiency very poor and suboptimal for any type of fluorescence/luminescence based measurement.

In the present paper, a LBT sequence has been genetically fused at the C-terminal end of heavy chain of mouse ferritin. The tag has been designed to be located inside the inner cavity such that the

lanthanide ion diffusing through the surface pores can eventually bind to the LBT sequence. The construct would thus act both as carrier targeted to CD71 receptors and as a FRET sensitizer.

## 2. METHODS

*2.1 Protein design, expression and purification.*

A synthetic gene encoding for mouse H chain ferritin (HFt) fused with a lanthanide binding peptide (LBT) was designed, synthesized, and optimized for *Escherichia coli* codon usage by Geneart (Geneart AG). LBT sequence YIDTNNDGWIEGDELLA [22] was added to the C-terminal of HFt generating HFt-LBT construct, that was subcloned into pET22-b vector (Novagene) between NdeI/XhoI restriction sites.

HFt-LBTwas overexpressed in *Escherichia coli* BL21 cells upon induction with 1 mM IPTG (Isopropyl-β-D-1-thiogalactopyranoside) at $OD_{600}$=0.6. Cells were harvested by centrifugation 16 hours post induction at 37°C.

Cells harvested from 1 L culture were resuspended in 20 mM HEPES buffer, pH 7.5, containing 200 mM NaCl, 1 mM TCEP (tris(2-carboxiethyl)phosphine), and a cOmplete TM Mini Protease Inhibitor Cocktail Tablet (Roche). Cells were disrupted by sonication and the soluble fraction was purified by heat treatment at 78°C for 10 minutes. Denatured *E. coli* proteins were removed by centrifugation at 15.000 rpm at 4°C for 1 hour. The soluble protein was further purified by ammonium sulfate precipitation. The precipitated fraction at 70% ammonium sulfate, was resuspended in 20 mM HEPES, 50 mM $MgCl_2$, pH 7.5 and dialyzed versus the same buffer. As final purification step, the protein was loaded onto a HiLoad 26/600 Superdex 200 pg column previously equilibrated in the same buffer using an ÄKTA-Prime system (GE Healthcare). Purified protein was concentrated to obtain the final protein preparation of 1 mg/mL and protein concentration was calculated by measuring the UV spectrum using an extinction coefficient of 32400 $M^{-1}cm^{-1}$. Protein yield was ~50 mg/l culture.

The expected molecular weight of 22662 Da was confirmed by MALDI-TOF Mass Spectrometry as reported in Supplementary Data (Figure S1).

*2.2 Fluorescence spectroscopy*

Fluorescence spectra and titrations were performed using FluoroMax 4 (Horiba) spectrofluorimeter with a Haake D8 refrigerated bath at 20 °C. Emission spectra were recorded between 450 and 560 nm, in order to include the luminescent maxima of Tb(III) (490 and 545 nm). The excitation wavelength was chosen at 295 nm to minimize the overlap of second order diffraction (570 nm) with the Tb(III) emission at 545 nm. Emission spectra were taken with excitation and emission band passes of 4

and 8 nm and corrected for the blank contribution and the instrument response at 295 nm in a quartz cell of 1 cm pathlength. Emission spectra were normalized to 1 at 545 nm.

Fluorescence measurements were performed using 1 μM apoHFt-LBT and apoHFt as a control in 100 mM MES buffer pH 6.4. A 50 mM $TbCl_3$ (Aldrich) stock solution was also prepared in MES buffer at pH 6.4. Fluorescence spectra were recorded upon 30 min incubation with excess of $TbCl_3$ in buffer solution followed by a washing step to remove the unbound metal. Titration data were obtained by addition of aliquots of $TbCl_3$ in buffer solution under continuous stirring.

*2.3 Cryo-Electron microscopy*

Holey-gold grids from Quantifoil R1.2/1.3 (Quantifoil Micro Tools GmbH) were prepared as described [31]; their surfaces were treated with plasma cleaning using a mixture of $H_2$ and $O_2$ and 3 μl of a solution containing 1 μM HFt-LBT Tb(III) complex was applied to the holey-gold grids. After 30 s waiting time, grids were blotted for 3 seconds at 100% humidity with filter paper and vitrified by rapidly plunging into liquid ethane at −180 °C [32, 33] with a Vitrobot Mark IV (FEI).

Data acquisition was performed using a FEI Titan Halo (FEI, Eindhoven) operating at 300 kV, while the specimen was maintained at liquid nitrogen temperatures. Datasets were collected with an automated data collection system [34] on a K2 Summit direct detector camera (Gatan, Pleasanton) operating in super-resolution mode, with a calibrated pixel size of 1.15 Å on the object scale and a magnification of 59 000×. Images were typically recorded with a defocus range between −0.7 and −3.0 μm and a dose of electrons on the specimen plane between 10 and 20 electrons/$Å^2$.

Data analysis was completely carried out using RELION 2.0 [35]. CTF correction was done using MotionCor2 [36]. Particles were picked and extracted from the original micrographs with the reference-based automated particle picking procedure implemented in RELION [37] and were 2D classified using 100 classes. 2D good classes were selected and then subjected to 3D classification with 8 classes (see Supplementary Figures S2 and S3), using as reference model the mouse H-ferritin structure (PDB code 3WNW). Resulting good classes were refined with the 3D Autorefine procedure in RELION.

The final 3D map resolution is calculated with the FSC = 0.143 criterion, based on the 'gold-standard' protocol [38], using soft masks with a 4 pixel soft edge, and has been corrected for the effects of the mask on the FSC curve using high-resolution noise substitution [39]. This final map was visualized using UCSF Chimera [40].

*2.4 Crystallization and X-ray structure determination.*

Crystals of apoHFt-LBT and HFt-LBT in complex with Tb(III) were obtained by mixing in a 2 µl hanging drop the purified protein at 15 mg/ml with a solution containing 1.8/2.0 M ammonium sulphate and 0.1 M Tris, pH 8.5, at 25° C within a week, cryo-protected by extensively washing the crystals in sodium malonate and flash-frozen in liquid nitrogen. Diffraction data were collected at XRD1 beamline at the Elettra Synchrotron, Trieste, Italy.

Data were processed with XDS [41] and scaled with Aimless [42] at a final resolution of 2.85 and 2.65 Å. The structures were solved by Molecular Replacement with Phaser [43, 44] using the structure of mouse H-chain modified ferritin (pdb code 3WNW) as search model. Model building and refinement were done using Coot [45] and Refmac5, respectively. The final model was analyzed with PROCHECK [46] and Molprobity [47]. Ramachandran Plot showed more than 98 % residues were in preferred regions and no outlier was observed in both structures. The validation of metal binding sites was performed using CheckMyMetal web server [48]. The final atomic coordinates and structure factors were deposited with the PDB Data Bank (www.rcsb.org) with accession code (5OBA and 5OBB, respectively). Complete data collection and refinement statistics are reported in Supplementary Data (Table S1).

*2.5 Cell cultures and ferritins internalization*

Human prostate cancer cell line DU-145 (ATCC® HTB81™), human colorectal cancer cell line HCT-116 (ATCC® CCL-247™), human breast cancer cell line MDA-MB-231 (ATCC® HTB-26™) and human ovarian cancer cell line SKOV-3 (ATCC® HTB-77™) were cultured in DMEM medium containing 10% FBS, 100 µg/ml streptomycin and 100 U/ml penicillin G in a humidified 37 °C incubator. The internalization assay was performed as follow: cells were detached using trypsin, then washed twice with PBS and resuspended in non-supplemented DMEM medium containing FITC-ferritin nanoparticles (HFt-LBT or mouse HFt as a control) at the final concentration 0.5 mg/ml for 1 hour in a humidified 37 °C incubator. After incubation cells were washed three times with PBS and subjected for confocal microscopy and flow cytometry analysis.

*2.6 Confocal microscopy*

Following internalization step described above, cells were seeded into 8-well Nunc™ Lab-Tek™ Chambered Coverglass with 200 µl DMEM medium containing 10% FBS, 100 µg/ml streptomycin and 100 U/ml penicillin G per well. Chambers with cells were then incubated on ice until microscopic visualization. Images were acquired using an inverted confocal microscope IX70 FV 500 (Olympus), with 488 nm laser, 20x objective lens and emission filter 505-560 nm. Image processing was performed

using ImageJ software (National Institutes of Health, www.imagej.nih.gov/ij/).

*2.7 Flow cytometry analysis*

Cells were incubated with FITC-ferritin nanoparticles as described previously then washed three times with PBS, and resuspended in FACS buffer (2% FBS, 1 mM EDTA). Internalization of ferritins before and after treatments was measured at the BD FACS Aria™ III equipped with a 488 nm laser. Cells were first gated by forward and side scatter area (FSC-A and SSC-A) plot and for singlets population (FSC-H and SSC-A), then detected in the channel for FITC expression (530/30nm filter) and side scatter parameter. The gate for the final detection was set according to the gate set on the control sample. Data were analyzed using BD FACS DIVA™ and Flow Josoftwares.

## 3. RESULTS

*3.1 Fluorescence spectroscopy*

Static emission spectra were recorded for both Terbium saturated HFt-LBT and wild type mouse HFt upon excitation at 295 nm. As reported in Figure 1, the intensity of the Terbium emission peak at 544 nm for HFt-LBT was at least two orders of magnitude higher with respect to HFt, indicating that the presence of the LBT effectively sensitizes the Terbium signal. The Terbium emission band at 544 nm for the HFt-LBT Tb(III) complex is detectable up to 4 pM protein concentration.

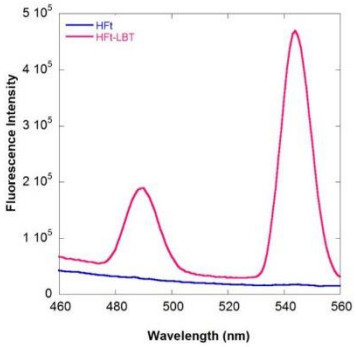


**Figure 1: Fluorescence spectra of HFt-LBT Tb(III) complex.**

Fluorescence spectra of HFt-LBT Tb(III) complex (red line) and wild type mouse HFtTb(III) complex (blue line) at the same protein concentration (1 μM). Spectra were recorded after 1 h incubation time with $TbCl_3$ in 0.1 M MES buffer pH 6.4.

Fluorescence titration analysis were thus carried out on HFt-LBT by adding free Tb(III) ions to the apoprotein (Figure 2 A and B).

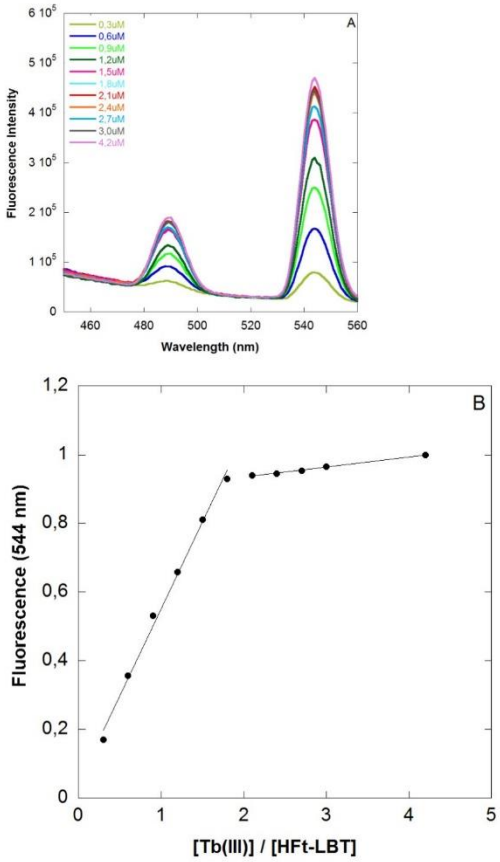


**Figure 2: Fluorescence titration of HFt-LBT with Tb(III).**

A) Fluorescence titration of HFt-LBT (1 µM) with incremental concentration of Tb(III) (0–4 equivalents) in 0.1 M MES buffer pH 6.4. Emission spectra were recorded in 1 cm pathlength cuvette

upon excitation at 295 nm. B) Fluorescence intensity of HFt-LBT Tb(III) complex as a function of the Tb(III)/HFt-LBT ratio. Fluorescent intensity was recorded at 545 nm and normalized to the emission maximum.

The titration endpoint was reached at 1.7 equivalent amount of Tb(III) per subunit. Extensive dialysis or size exclusion chromatography could not remove bound Tb(III). Titrations were conducted at pH 6.4 in MES buffer, in order to avoid precipitation of Terbium hydroxides, easily formed around neutrality. Analogous titrations carried out on wild type mouse HFt, demonstrated a negligible fluorescence contribution provided by Terbium bound to the metal binding sites of the native protein (*i.e.* ferroxidase site, threefold channel and nucleation centre). Thus, the presence of the tryptophan residue within the LBT, appears to account for most of the observed fluorescence signal. However, an additional contribution of the tryptophan residue as a FRET sensitizer is envisaged to enhance emission not only of the Tb(III) atom within the tag but also to the other Tb(III) atoms present in the ferroxidase site or in the threefold channels.

*3.2 Cryo-EM microscopy*

A plasma cleaned solution of HFt-LBT Tb(III), applied to holey-gold grids and vitrified, was used to obtain a complete 7.1 Å resolution map of the protein structure in solution (see Figure 3 and Figure S4).

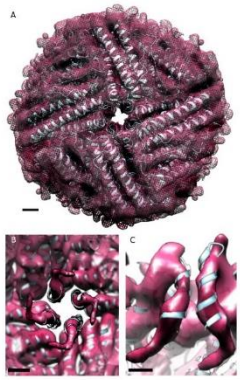


**Figure 3: 3D postprocess final maps of HFt-LBT Tb(III) from Cryo EM analysis.**

Data were obtained with RELION and visualized with UCSF Chimera. Light blue: X-ray diffraction data of the crystal Terbium structure. Pink: experimental Cryo-EM electronic density map.

Map resolution: 7.1 Angstroms. Scale bar=10 Angstroms. A: external view; B: internal view; C: focus on one internal C-terminal helix.

The final 3D map of HFt-LBT Tb(III) corresponds to an overall structure that conforms to the high resolution crystallographic data indicating perfect matching of the subunit assembly and helix axes. It is worth considering, from the analysis of the selected 2D classes, that significant densities appear within the internal cavity that can be attributed to the lanthanide binding tags (see Supplementary Data, Figure S2). Nevertheless, considerable heterogeneity of the observed signals does not allow even a partial reconstruction of at least a single conformation of the 24 LBTs. Only, a kinked fragment of the terminal tail can be modeled, which corresponds to a segment of 6-7 aminoacids.

*3.3 X-ray crystal structure*

The structures of apoHFt-LBT and HFt-LBT Tb(III) were determined by X-ray crystallography at a 2.85 Å and 2.65 Å resolution, respectively. They both crystallized in I222 space group with 24 identical subunits in the asymmetric unit (ASU) with a solvent content of 64,7%. The overall X-ray-structure confirms that the LBT does not affect the protein scaffold which corresponds to the native H-chain mouse ferritin (pdb code 3WNW) with a *rmsd* value of 0.1 Å. However, the LBT loop is not visible in both structures, due to the high flexibility of the C-terminus region. Temperature factors analysis shows a mean B factor of 57 $Å^2$ calculated for the main chain of the subunits in both structures and 78 $Å^2$ for the Terbium ions modelled in HFt-LBT Tb(III).

X-ray emission scans ranging from 4.0 to 8.0 KeV of the crystals were performed in order to confirm the presence of the Terbium in the samples. Characteristic L and M X-ray line energies of Terbium were clearly identified in the HFt-LBT Tb(III) crystals. Accordingly, the crystals of apoHFt-LBT lacked these emission energies and displayed the presence of residual iron atoms at the characteristic energies lines in the emission scan.

In HFt-LBT Tb(III) structure, 24 Terbium ions were positioned and successfully refined with a 75% occupancy in each ferroxidase site of the protein scaffold and 8 Terbium ions were positioned with 100 % occupancy in each three-fold axes. In the ferroxidase center, each Terbium ion is located in a trigonal planar coordination to OE1-Gln141 and to OE1 and OE2-Glu62, and to OE2-Glu27, in a range 2.6-3.2 Å distance (Figure 4A). In the 3-fold center, the Terbium ion is tetrahedrally coordinated to OE1-Glu134 of the three subunits, (at 2.2-2.4 Å distance) (Figure 4B). In the 4-fold channels were positioned and successfully refined one water molecule.

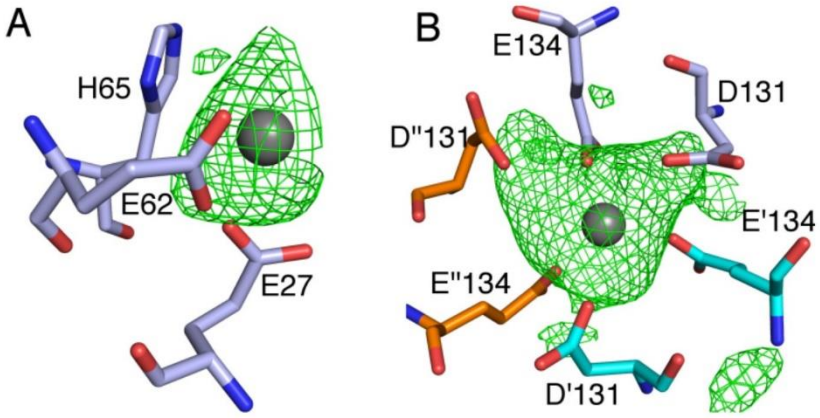


**Figure 4: Terbium binding sites from X-ray crystallography.**

The omit map contoured at 3 σ is shown as a green mesh A) In the ferroxidase center: a Tb(III), is shown as a grey sphere and B) in the 3-fold axes: the residues Glu131 and Glu134 of three different monomers are depicted as sticks in light blue, cyan and orange, respectively.

*3.4 Ferritins uptake by tumor cell lines*

After demonstration that HFt-LBT Tb(III) maintained the overall structure of the wild type mouse HFt, binding and internalization of the construct was analyzed in selected cancer cell lines. It is known that HFt is recognized and internalized by the CD71 (TfR1), which is overexpressed in many types of tumor cells but not in normal cells and healthy tissues [49]. Experiment on cells treated with the same amount (0.5 mg/ml) of HFt-LBT Tb(III) or HFt were undertaken in order to study uptake efficiency by cancer cells by flow cytometry and confocal microscopy. As a baseline for FITC fluorescence, control cells untreated with FITC-ferritins were used. In order to exclude any signal generated from outside particles sticking on the cell membrane due to unspecific binding or remaining from the washing steps, Trypan blue quenching was performed before FACS acquisition. In Supplementary Figures S5, the FACS analysis is summarized, shown as the percentage of cells internalizing the nanoparticles. These data highlighted that HFt-LBT Tb(III) nanoparticles are efficiently taken up by all cells of each cell line. All acquisition plots are shown in Figure S5.

In order to visualize HFt-LBT Tb(III) nanocages within cytoplasm, cells were observed under confocal microscopy. Confocal representative images of entire field of view of live cells incubated with HFt-LBT Tb(III) are shown in Figure 5A. Images confirmed the high extent of both HFt-LBT Tb(III) and wild type mouse HFt internalization and highlight similar cellular distribution in the cytoplasm and in the perinuclear space.

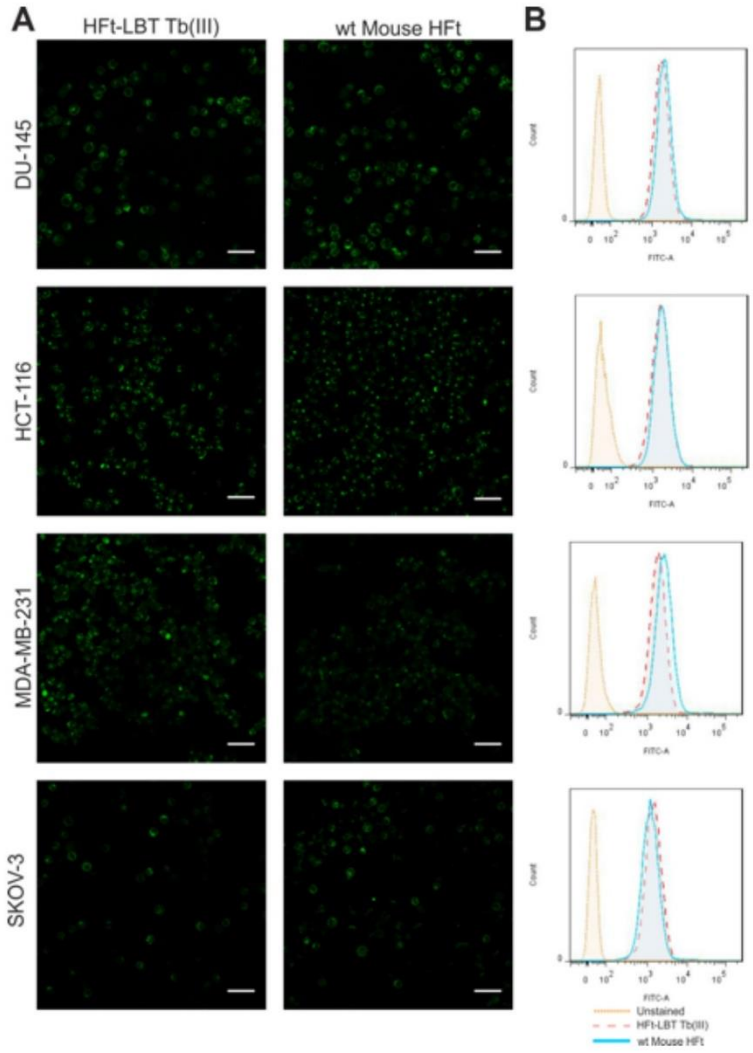
A
HFt-LBT Tb(III)
wt Mouse HFt
B
DU-145
HCT-116
MDA-MB-231
SKOV-3
Count
FITC-A
Unstained
HFt-LBT Tb(III)
wt Mouse HFt

**Figure 5: Confocal microscopy images and flow cytometry analysis of HFt-LBT Tb(III) uptake by selected tumor cell lines.**

DU-145, HCT-116, MDA-MB-231 and SKOV-3 cancer cells were incubated with either HFt-LBT Tb(III) or wt mouse HFt (0.5 mg/ml) for 60 min. A) Images acquired by confocal microscopy showing side by side comparison of cellular distribution of HFt-LBT Tb(III) and HFt conjugated with FITC. Scale bar = 50 μm. B) Flow cytometry analysis of HFt-LBT Tb(III) and HFt cellular uptake.

## 4. DISCUSSION

In the present work, an engineered ferritin construct, bearing a lanthanide binding tag on the C-terminal end of each subunit of mouse H ferritin, was designed in order to build a biomolecular nanosystem endowed with strong FRET sensitization properties. The peptide tag (LBT) was designed according to the findings of Martin *et al.*, [22] that demonstrated efficient lanthanide chelating properties of a peptide sequence derived from $Ca^{2+}$ binding sites from Troponin C EF hand motif. The LBT has six metal-binding residues that form a coordination sphere around a lanthanide (III) ion and is endowed with high affinity and strong FRET effect from the encoded tryptophan residue to the Terbium or Europium ions. Spectroscopic and crystallographic studies showed that the inner coordination sphere of Tb(III) bound to this sequence was free from water molecules [21], a key feature for luminescence experiments, given the quenching effect of O-H vibration [50]. Accordingly, the HFt-LBT construct exhibited high affinity Tb(III) binding as demonstrated by fluorescence spectroscopy measurements in solution in comparison with the native protein. In these measurements, excitation of the tryptophan residue present in the center of the LBT provided an excellent FRET to the Terbium atom with a sustained narrow emission at the 544 nm line typical of Terbium excited state decay (see Figure 1). The thermodynamics of the Terbium binding process was however complex due to the well known presence of additional metal binding sites to the ferritin 24-mer [28-30]. In particular, the observed fluorescence signal accounted for 1.7 Tb(III) ions per subunit indicating that the presence of the tryptophan residue within the tag is able to act as an antenna system not only for the Tb(III) ion bound within the LBT tag but also for a number of extra Tb(III) atoms bound to ferritin binding site. Spurious effects due to other contributions are ruled out by control experiments on wild type mouse HFt, still able to bind Tb(III) within the canonical metal binding sites but endowed with negligible fluorescence in the Tb(III) emission regions.

Analysis of the three-dimensional structure of the HFt-LBT Tb(III) complex, by X-ray crystallography and cryo-EM demonstrates that the presence of the C-terminal tag does not affect the overall assembly of the protein and that the genetically fused tags point to the interior cavity. The peptide arm connecting the lanthanide binding loop to the C-terminal sequence is, as expected, flexible and does not allow for a complete resolution of the local structure [51]. Interestingly, cryo-EM reconstruction provided the identification of low resolution but definite patterns relative to the first few aminoacids of the tag, though the possible multiple orientations of the loop region precluded the observation of the Tb(III) complex. X-ray data further demonstrated that Terbium ion is efficiently complexed at the threefold axis channels (8 channels per 24-mer) by side chains of E131 and D134 aminoacids from each of the three adjacent subunits. Further Tb(III) binding occurs stoichiometrically at the ferroxidase site (24 sites per 24-mer), coordinated by carboxyl residues E27 and E62 with minor participation of H65. In contrast, LBT bound Tb(III) atoms were not visible by X-ray diffraction. In summary, HFt-LBT construct is capable of high affinity binding of 24 Tb(III) atoms at each tag and 20, out of 24 available (occupancy in X-ray structure corresponded to 75%), at the ferroxidase binding site. In addition, 8 fully occupied sites are observed at the entrance of the threefold channels for a total of 56 Terbium atoms within the whole 24-mer.

In the present investigation on confocal microscope, however, attempts to image live cells by direct excitation at 290-375 nm of the tryptophan residue in the lanthanide binding loop after ferritin uptake yielded very poor results due to the very high fluorescence background within the typical Terbium emission interval. We thus report measurements in which HFt-LBT Tb(III) or wild type mouse HFt have been labeled with common FITC. Results demonstrate that the HFt-LBT Tb(III) complex is very efficiently uptaken by all four human tumor cell lines selected. In particular, DU145 (from a central nervous system metastasis, of primary prostate adenocarcinoma origin), MDA-MB-231 (from invasive ductal carcinoma, Hepatoma cell line and SK-OV-3 (highly resistant ovarian cancer cell line) were demonstrated for the first time to display a high uptake of both wild type mouse HFt and HFt-LBT Tb(III). These cancer cell lines overexpress CD71 molecule and are subject of cancer therapy studies focused on this receptor (PMID: 20180585; PMID: 26491294; PMID: 23267137; PMID: 23752192).

**Conclusions**

In conclusion, we have shown that a ferritin nanocage can be engineered by addition of appropriate metal binding tags inside the cavity in order to provide specific additional metal sites in topologically selected positions. This approach is in alternative to the quasi random metal cluster

insertion into the ferritin cavity that has been commonly used by free diffusion of metal ions through the open pores on the surface of the macromolecule or by disassembly-reassembly of the 24-mer structure ("encapsulation" procedure) [8]. The importance of a guided allocation of metal sites inside the cavity is however essential to proceed with rationale positioning of antenna systems vs. lanthanide sites in order to assess the best geometry for efficient FRET. Rational design of such metal binding sites would foster most advanced applications such as the construction of up-converting nanoparticles or ultrabright fluorescent organic polymer for single molecule detection.

**Acknowledgment**

The authors are grateful to the ELETTRA XRD-1 beamline staff for their help and assistance during the data collection and fluorescence emission experiments. This study has received funding from the European Community's Seventh Framework Programme (FP7/2007-2013) under grant agreement n° 312284. The biological part of the study was supported by the grant from National Science Centre (NCN) in Poland no. UMO-2015/18/E/NZ6/00642. EU H2020 Project "X-Probe", Grant N° 637295, to A. Bonamore and M.C.T. is gratefully acknowledged. Flagship project "Nanomax" from MIUR to A. Boffi is also acknowledged.

**References**

[1] Arosio P, Elia L and Poli M 2017 Ferritin, cellular iron storage and regulation *IUBMB Life*. **69**(6) 414-422

[2] Theil EC 2013 Ferritin: the protein nanocage and iron biomineral in health and in disease *Inorg. Chem.* **52**(21) 12223-12233

[3] Calisti L, Benni I, Cardoso Trabuco M, Baiocco P, Ruzicka B, Boffi A, Falvo E, Malatesta F and Bonamore A2017 Probing bulky ligand entry in engineered archaeal ferritins *Biochim Biophys Acta.***1861**(2 )450-456

[4] Zhen Z, Tang W, Chen H, Lin X, Todd T, Wang G, CowgerT, Chen X and Xie J 2013RGD-modified apoferritin nanoparticles for efficient drug delivery to tumors *ACS Nano* **7** 4830–4837

[5] Kanekiyo M, Wei C-J, Yassine HM, McTamney PM, Boyington JC, Whittle JR, Rao SS, Kong WP, Wang L and Nabel GJ 2013 Self-assembling influenza nanoparticle vaccines elicit broadly neutralizing H1N1 antibodies *Nature* **499** 102–106

[6] Valero E, Fiorini S, Tambalo S, Busquier H, Callejas-Fernández J, Marzola P, Gálvez N and Domínguez-Vera JM 2014 In vivo long-term magnetic resonance imaging activity of ferritin-based magnetic nanoparticles versus a standard contrast agent*J. Med. Chem.***57**(13)5686-5992

[7] Fracasso G, Falvo E, Colotti G, Fazi F, Ingegnere T, Amalfitano A, Doglietto GB, Alfieri S, Boffi A, Morea V, Conti G, Tremante E, Giacomini P, Arcovito A and Ceci P 2016 Selective delivery of doxorubicin by novel stimuli-sensitivenano-ferritins overcomes tumor refractoriness *J. Control Release* **239** 10-18

[8] Falvo E, Tremante E, Arcovito A, Papi M, Elad N, Boffi A, Morea V, Conti G, Toffoli G, Fracasso G, Giacomini P and Ceci P 2016 Improved Doxorubicin Encapsulation and Pharmacokinetics of Ferritin-Fusion Protein Nanocarriers Bearing Proline, Serine, and Alanine Elements *Biomacromolecules* **17**(2) 514-522

[9] Bain J and Staniland SS 2015 Bioinspired nanoreactors for the biomineralisation of metallic-based nanoparticles for nanomedicine *Phys. Chem. Chem. Phys.***17**(24)15508-15521

[10] Tian L, Dai Z, Liu X, Song B, Ye Z and Yuan J 2015Ratiometric Time-Gated Luminescence Probe for Nitric Oxide Based on an Apoferritin-Assembled Lanthanide Complex-Rhodamine Luminescence Resonance Energy Transfer System *Anal. Chem.* **87**(21) 10878-10885

[11] Maity B, Abe S and Ueno T 2017 Observation of gold sub-nanocluster nucleation within a crystalline protein cage *Nat.Commun.***8**:14820

[12] Handl HL and Gillies R 2005 Lanthanide-based luminescent assays for ligand-receptor interactions *J. Life Sci.***77** 361-371

[13] Hemmila I and Laitala VJ 2005 Progress in lanthanides as luminescent probes *Fluoresc.* **15** 529-542

[14] Bunzli J 2006 Benefiting from the unique properties of lanthanide ions *Acc. Chem. Res.* **39**, 53-61

[15] Rajapakse HE, Reddy DR, Mohandessi S, Butlin NG and Miller LW 2009 Luminescent terbium protein labels for time-resolved microscopy and screening *Angew. Chem. Int.* **48**, 4990-4992

[16] Gudgin Dickson EF, Pollak A and Diamandis EP 1995 Time-resolved detection of lanthanide luminescence for ultrasensitive bioanalytical assays *Photochem. Photobiol. B***27**(1)3-19

[17] Selvin PR 2002 Principles and biophysical applications of lanthanide-based probes *Annu. Rev. Biophys. Biomembr.* **31** 275-302

[18] Bunzli JC (2004) Luminescent lanthanide probes as diagnostic and therapeutic tools *Met. Ions. Biol. Syst.* **42** 39-75

[19] Franz KJ, Nitz M and Imperiali B 2003 Lanthanide-binding tags as versatile protein coexpression probes *Chembiochem.* **4**(4) 265-271

[20] Nitz M, Franz KJ, Maglathlin RL and Imperiali B 2003 A powerful combinatorial screen to identify high-affinity terbium(III)-binding peptides *Chembiochem.* **4**(4) 272-276

[21] NitzM, Sherawat, M, Franz KJ, Peisach E and Allen KN 2004 Structural origin of the high affinity of a chemically evolved lanthanide-binding peptide *Angew. Chem. Int. Ed.Engl.* **43**(28) 3682-3685

[22] Martin LJ, Hähnke MJ, Nitz M, Wöhnert J, Nicholas R, Silvaggi, Allen KR, Schwalbe H, Imperiali B 2007 Double-Lanthanide-Binding Tags: Design, Photophysical Properties, and NMR Applications *J. Am. Chem. Soc.* **129** (22) 7106–7113

[23] Wo¨hnert J, Franz KJ, Nitz MI, mperiali B and Schwalbe H 2003 Protein alignment by a coexpressed lanthanide-binding tag for the measurement of residual dipolar couplings *J. Am.Chem. Soc.***125** 13338-13339

[24] Su XC, Huber T, Dixon NE and Otting G 2006 Site-specific labelling of proteins with a rigid lanthanide-binding tag *Chembiochem.* **7**1 599-1604

[25] Goda N, Tenno T, InomataK, Iwaya N and Sasaki Y 2007LBT/PTD dual tagged vector for purification, cellular protein delivery and visualization in living cells *Biochim. Biophys. Acta* **1773**(2) 141-614

[26] Shirakawa M and Hiroaki H 2007 LBT/PTD dual tagged vector for purification, cellular protein delivery and visualization in living cells *Biochim. Biophys. Acta* **1773**, 141-146

[27] Sculimbrene BR and Imperiali B 2006 Lanthanide-binding tags as luminescent probes for studying protein interactions *J. Am. Chem. Soc.* **128** 7346-7352

[28] Stefanini S, Chiancone E, Antonini E and Finazzi-Agro A 1983 Binding of Terbium to apoferritin: a fluorescence study *Arch. Biochem. Biophys.* **222**(2) 430-434

[29] Treffry A and Harrison PM 1984 Spectroscopic studies on the binding of iron, terbium, and zinc by apoferritin *J. Inorg. Biochem.***21**(1) 9-20

[30] Bou-Abdallah F, Arosio P, Levi S, Janus-Chandler C and Chasteen ND 2003 Defining metal ion inhibitor interactions with recombinant human H- and L-chain ferritins and site-directed variants: an isothermal titration calorimetry study *J. Biol. Inorg. Chem.* **8**(4) 489-497

[31] Russo C J and Passmore LA 2014Ultrastable gold substrates for electron cryomicroscopy *Science* **346** 1377–1380

[32] Dubochet J, Adrian M, Chang JJ, Homo JC, Lepault J, McDowall AW and Schultz P 1998 Cryo-electron microscopy of vitrified specimens *Q. Rev. Biophys.***21** 129–228

[33] Wagenknecht T, Grassucci R and Frank J. 1988 Electron microscopy and computer image averaging of ice-embedded large ribosomal subunits from Escherichia coli *J. Mol. Biol.* **199** 137–147

[34] Suloway C, Pulokas J, Fellmann D, Cheng A, Guerra F, Quispe J, Stagg S, Potter CS and Carragher B 2005 Automated molecular microscopy: the new Leginon system *Struct. Biol.***151** 41–60

[35] Scheres SH 2012 "RELION: Implementation of a Bayesian Approach to Cryo-EM Structure Determination *J. Struct. Biol.* **180**(3) 519-530

[36] Zheng SQ, Palovcak E, Armache JP, Cheng Y and Agard DA 2016 Anisotropic Correction of Beam-induced Motion for Improved Single-particle Electron Cryo-microscopy *Nature Methods* **14** 331–332

[37] Scheres SHW 2015 Semi-automated selection of cryo-EM particles in RELION-1.3 *J. Struct. Biol.* **189** 114–122

[38] Rosenthal PB and Henderson R 2003 Optimal determination of particle orientation, absolute hand, and contrast loss in single-particle electron cryomicroscopy *J. Mol. Biol.***333** 721–745

[39] Chen S, McMullan G, Faruqi AR, Murshudov GN, Short JM, Scheres SH and Henderson R 2013 High-resolution noise substitution to measure overfitting and validate resolution in 3D structure determination by single particle electron cryo-microscopy *Ultramicroscopy* **135** 24–35

[40] Pettersen EF, Goddard TD, Huang CC, Couch GS, Greenblatt DM and Meng EC 2004 UCSF Chimera--a visualization system for exploratory research and analysis *J. Comput. Chem.***25**1605–1612

[41] Kabsch W 2010 Integration, scaling, space-group assignment and post-refinement *Acta Crystallogr. D Biol. Crystallogr.* **66**, 133-44

[42] Winn MD, Ballard CC, Cowtan KD, Dodson EJ, Emsley P, Evans PR, Keegan RM, Krissinel EB, Leslie AG, McCoy A, McNicholas SJ, Murshudov GN, Pannu NS, Potterton EA, Powell HR, Read RJ, Vagin A and Wilson KS 2011 Overview of the CCP4 suite and current developments *Acta Crystallogr. D Biol. Crystallogr.* **67**(4) 235-242

[43] Adams PD, Afonine PV, Bunkoczi G, Chen VB, Davis IW, Echols N, Headd JJ, Hung LW, Kapral GJ, Grosse-Kunstleve RW, McCoy AJ, Moriarty NW, Oeffner R, Read RJ, Richardson DC, Richardson JS, Terwilliger TC and Zwart PH 2010 PHENIX: a comprehensive Python-based system for macromolecular structure solution *Acta Cryst. D* **66** 213-221

[44] McCoy AJ, Grosse-Kunstleve RW, Adams PD, Winn MD, Storoni LC and Read RJ 2007 Phaser crystallographic software *J. Appl. Crystallogr.*: **40** 658-674

[45] Emsley P and Cowtan K 2004 Coot: model-building tools for molecular graphics *Acta Crystallogr. D Biol Crystallogr.* **60** 2126–2132

[46] Laskowski RA, MacArthur MW, Moss DS and Thornton JM 1993 PROCHECK - a program to check the stereochemical quality of protein structures J. *App. Cryst.***26** 283-29125

[47] Chen VB, Arendall WB 3rd, Headd JJ, Keedy DA, Immormino RM, Kapral GJ, Murray LW, Richardson JS and Richardson DC 2010 MolProbity: all-atom structure validation for macromolecular crystallography *Acta Crystallogr. D Biol.Crystallogr.***66**(1)12-21

[48] Zheng H, Cooper DR, Porebski PJ, Shabalin IG, Handing KB and Minor W 2017 Check My Metal: a macromolecular metal-binding validation tool *Acta Crystallogr. D Struct. Biol.***73**(3) 223-233

[49] Habashy HO, Powe DG, Staka CM, Rakha EA, Ball G, Green AR, Aleskandarany M, Paish EC, Douglas Macmillan R, Nicholson RI, Ellis IO, Gee JM. Transferrin receptor (CD71) is a marker of poor prognosis in breast cancer and can predict response to tamoxifen. *Breast Cancer Res Treat*. 2010 Jan;119(2) 283-93

[50] Horrocks WD Jr and Sudnick DR 1979 Lanthanide ion probes of structure in biology. Laser-induced luminescence decay constants provide a direct measure of the number of metal-coordinated water molecules *J. Am. Chem. Soc.***101** 334-340

[51] Barthelmes D, Granz M, Barthelmes K, Allen KN, Imperiali B, Prisner T and Schwalbe H 2015 Encoded loop-lathanide-binding tags for log-range distance measurements in proteins by NMR and EPR spectroscopy *J. Biomol. NMR* **63** 275-282

# APPENDIX IV

# Other published papers

Bonamore A, Calisti L, Calcaterra A, Ismail OH, Gargano M, D'Acquarica I, Botta B, Boffi A, Macone A. A Novel Enzymatic Strategy for the Synthesis of Substituted Tetrahydroisoquinolines. ChemistrySelec 2016;1(8):1525-1528.

Bonamore A, Gargano M, Calisti L, Francioso A, Mosca L, Boffi A, Federico R. A Novel Direct Method for Determination of Riboflavin in Alcoholic Fermented Beverages. Food Analytical Methods 2016; 9(4)840-844.